

Universität der Bundeswehr München
Fakultät für Luft- und Raumfahrttechnik
Institut für Strömungsmechanik und Aerodynamik

Investigation of bubble dynamics in turbulent background flow

M. Sc. Katharina Haase

Vollständiger Abdruck der bei der
Fakultät für Luft- und Raumfahrttechnik
der Universität der Bundeswehr München
zur Erlangung des akademischen Grades eines

Doktor der Naturwissenschaften (Dr. rer. nat.)

genehmigten Dissertation

1. Berichterstatter: Prof. Dr. rer. nat. habil Christian J. Kähler
2. Berichterstatter: Prof. Dr. Achim Wixforth

Diese Dissertation wurde am 02.11.2020 bei der Universität der Bundeswehr München, 85577 Neubiberg eingereicht und durch die Fakultät für Luft- und Raumfahrttechnik am 12.05.2021 angenommen. Die mündliche Prüfung fand am: 30.06.2021 statt.

ACKNOWLEDGMENTS

The author wants to thank the following people for helping during the experiments and writing of the thesis.

- Prof. Dr. rer. nat. Christian J. Kähler for giving me the chance to work at his institute and the many helpful discussions, we held during my time working on the project and thesis.
- Prof. Dr. Achim Wixforth for being my second corrector and for the nice conversations we had during the evaluation of my work.
- Dr. Sven Scharnovski and Dr. Rainer Hain for the help with many problems that occurred during the experiments and evaluation.
- Thomas Fuchs, Nico Reuther and Benedikt Mutsch for the help with my experiments and the many fruitful discussions.
- Dr. Martin Osberger and Dr. Bianka Aas for the help with the chemical tracer system.
- The DFG and everyone from the SPP 1740 for the funding and the yearly meetings that helped further ideas and discussions.

TABLE OF CONTENTS

	Page
LIST OF FIGURES	v
SYMBOLS	x
ABSTRACT / KURZFASSUNG	1
1 General aspects of a single bubble rising in water	5
1.1 Introduction - Bubbles in the real world	5
1.2 Bubbles and how to describe them	6
1.2.1 Different bubble shapes, velocity and path	6
1.2.2 Bubbles in dimensionless numbers	12
1.2.3 Shape oscillations	12
1.2.4 Flow and turbulence of a rising bubble swarm	15
1.3 Interaction between the bubble and the surrounding liquid	21
2 Experimental Facility	23
2.1 Introduction	23
2.2 Description of the counter-flow Channel	23
2.3 Characterization of the Counter-flow Channel	27
3 Emulation of bubble induced turbulence	30
3.1 Introduction	30
3.2 Free moving Particle Grids	31
3.2.1 Experimental Setup	31
3.2.2 Characterization of the particle grids and turbulence analysis	33
3.3 Fractal Grids	44
3.4 Summary and Conclusion	48
4 A novel approach to describe 3D bubble deformation with a tomographic reconstruction	49
4.1 Introduction	49
4.2 Experimental setup	49
4.3 Comparison of different methods	51
4.4 Sensitivity analysis	56
4.5 Conclusions	58
5 Behavior of a free rising single bubbles	59
5.1 Introduction	59
5.2 Experimental Setup	59
5.3 Results and discussions	61
5.3.1 Rising path in quiescent water	61
5.3.2 Deformation of the surface	61
5.3.3 Wake structures	64
5.4 Conclusion	68
6 Behavior of a single bubble in swarm like background turbulence	71
6.1 Introduction	71
6.2 Experimental Set-up	71
6.3 Results of path measurements, oscillations and flow structures	72
6.3.1 Movement in emulated turbulence	72

TABLE OF CONTENTS

6.3.2	Shape oscillations induced by emulated turbulence	75
6.3.3	Influence of the bubble on the velocity and fluctuations inside the liquid flow	76
6.3.4	Influence of the turbulence on the bubbles wake structures	80
6.4	Summary and Conclusions	84
7	Conclusions and outlook	86
	LIST OF REFERENCES	90

LIST OF FIGURES

Figure	Page
1.1 Sketch of a single bubble with the definition of the axis.	7
1.2 Velocity field and streamwise vorticity distribution in a horizontal plane downstream of a spiraling bubble at $Re = 5360$. The bubble spirals in the horizontal plane along the dashed line around the center of the cross. The direction of lateral bubble motion is indicated by the arrow. Left: velocity field $y(x,y)$ ($u_{max} = 300$ mm/s); right: regions of concentrated streamwise vorticity u_z (contour lines start from ± 5 mm/s in steps of 2 mm/s; solid line: positive value, dashed lines: negative value). Reproduced from Brücker (1999), with the permission of AIP Publishing.	10
1.3 Evolution of the velocity field and stream wise vorticity distribution in a horizontal plane 10 mm downstream of the zigzagging bubble for the moments (A)(F). The zigzagging motion of the bubble in the horizontal plane is along the y axis. Left column: velocity field $y(x,y)$ ($v_{max} = 70$ mm/s); right column: regions of concentrated stream wise vorticity ω_z (contour lines start from $\pm 1/s$ in steps of 1/s; solid line: positive value, dashed lines: negative value). Reproduced from Brücker (1999), with the permission of AIP Publishing.	11
1.4 Top images: Visualization of a colorized vortex and schematic interpretation in the cross section for a rocking bubble $Re = 1500$. Bottom four images: Spatial-Temporally reconstructed vertical flow around a spiraling bubble. The solid line indicates the position of the bubble. The dashed line indicates the measurement plane. The left column shows the velocity, while the right shows the according isolines of the vorticity. Reproduced from Brücker (1999), with the permission of AIP Publishing.	13
1.5 Sketch to visualize axis definitions used in this work (left side) and the mode $f_{2,0}$ and $f_{2,2}$ waves (right side). The $f_{2,0}$ waves are moving from the front to the rear stagnation points (from pole the pole), and mode $f_{2,2}$ waves are traveling around the equator of the bubbles.	14
1.6 Change in the oscillation frequencies depending on the spherical equivalent radius. Taken from Lunde & Perkins (1998), with permission from Springer Nature.	15
1.7 Velocity in a cross-section of a container, normalized by the mean bulk velocity. (a), (c), (e) shows the vertical velocity, and (b), (d), (f) the radial one. From top to bottom the distance to the bubble swarm was increased. From top to bottom the measurement position is rather away from the injection point of the swarm. The marker type indicates different bubble swarm densities. The open circle has a volume fraction of α [%] 0.05, the open squares 0.1, the open triangles 0.17 and the filled circles 0.64. The image is taken with permission from Kim et al. (2016).	17
1.8 Velocity fluctuations in the liquid phase normalized by the bulk velocity. In the left column are the vertical fluctuations plotted with a comparison to single phase flows. In the right column the radial fluctuations are compared to single phase flows at different Reynolds numbers. From top to bottom the measurement position is rather away from the injection point of the swarm. The marker type indicates different bubble swarm densities. The open circle has a volume fraction of α [%] 0.05, the open squares 0.1, the open triangles 0.17 and the filled circles 0.64. The image is taken with permission from Kim et al. (2016).	18

LIST OF FIGURES

1.9	Semi-logarithmic plots of the PDFs measured and published by Riboux et al. (2009). In the left column the fluctuations in z direction (against the bubble rising direction). The right column shows it perpendicular to it. From top to bottom the distance to the bubble swarm is increased. Reprinted with permission.	19
1.10	Spectra of vertical fluctuations calculated from PIV images. The different lines show different PIV interrogation windows and outlier detections. The bubble diameter was 2.5 mm and the density 0.46 %. The image was taken from Riboux et al. (2009) with permission.	21
2.1	Left: Schematic drawing of the channel. Published in Schlüter et al. (2021) and reprinted with permission. Right: Photograph	24
2.2	Comparison of the three different particle grids. From left to right the fractal grid, the free moving particle grid and the active grid.	25
2.3	Absolute velocity profile across the channel. Left shows the mean velocity profile along the channel normal for three different inflow velocities. The right picture shows the corresponding turbulence level. The graphs don't span the full channel width due to a blockage of the beams holding the glass.	29
2.4	Profile characterization of the boundary layer of the channel. The left image shows again the velocity profile along the channel normal for four different velocities. In the right is the corresponding Turbulence level plotted. Published in Schlüter et al. (2021) and reprinted with permission.	29
3.1	Photograph of one exemplary particle grid. Only the top two layers are fixed in all spatial directions. Every following layer is solely attached vertically, allowing the particle strings to move freely in a horizontal plane. Published in (Schlüter et al. 2021) and reprinted with permission.	31
3.2	A comparison of the flow velocities behind the free moving particle grids. Left image: Comparison of the velocity profile in spanwise direction at $\sim 3 d_p$ behind the last layer of grid elements. Right image: Vertical velocity component (u_z) in flow direction under a grid element against the distance in particle diameters of the grid. The flow behind grids with big elements decays proportional to $\exp(-1.12)$, while the flow behind smaller elements decays slower, proportional to $\exp(-0.46)$. Published in Schlüter et al. (2021) and reprinted with permission.	34
3.3	Comparison of the introduced turbulence by the different grids. Left image: Comparison of the turbulence profile in spanwise direction at $\sim 3d_p$ behind the last layer of grid elements. Right image: Vertical decay of the turbulence Tu under a grid element against the distance in particle diameters of the grid. Published in Schlüter et al. (2021) and reprinted with permission.	35
3.4	Comparison of the velocity and turbulence in the boundary layer profile behind different particle grids. The falloff in the left image results from the end of the measured image and is an artifact from the PIV evaluation. This is not physical and solely an error in the measurement.	36
3.5	Comparison of the velocity and turbulence in the boundary layer profile in increasing distances behind the elliptical particle grid. Close to $x = 0.5$ in the Minimum of the graph the wall was positioned. Theoretically the velocity should go to 0, but due to the finite PIV evaluation windows the wall cannot fully be resolved. The small increase on the left side of the minimum is the mirror image of the particle in the glass channel walls. The same would be visible in the image for the turbulence but the values here are cut off by the graph. The fall off on the right side can also be explained by the finite measurement windows at the edge of the recording.	37

LIST OF FIGURES

3.6	Comparison of the velocity and turbulence profile in the boundary layer for different bulk velocities with the elliptical grid mounted. and turbulence in the boundary layer profile in increasing distances behind the elliptical particle grid. Close to $x = 0.5$ in the Minimum of the graph the wall was positioned. Theoretically the velocity should go to 0, but due to the finite PIV evaluation windows the wall cannot fully be resolved. The small increase on the left side of the minimum is the mirror image of the particle in the glass channel walls. The same would be visible in the image for the turbulence but the values here are cut off by the graph. The fall off on the right side can also be explained by the finite measurement windows at the edge of the recording.	37
3.7	Comparison of the normalized p.d.f. of horizontal (top image) and vertical fluctuations (bottom image) for all grids. Both are normalized and scaled with the volume fraction. ($\alpha_0 = 0.001$ and U_0 is the mean bulk velocity).Published in Schlüter et al. (2021) and reprinted with permission.	39
3.8	Top image Shows the normalized p.d.f. of liquid velocity fluctuations in span wise direction and the bottom in the flow direction in comparison with measurements published in Risso (2016) that were performed for different bubbles sizes and volume fractions. Published in Schlüter et al. (2021) and reprinted with permission.	40
3.9	Energy spectra measured with EDM at the facility at the University in Bremen. The -5/3 and -8/3 slopes are added. The range of frequencies that are responsible for the bubble deformation are marked. Published in Schlüter et al. (2021) and reprinted with permission.	42
3.10	Example of diffusion visualization using PIV tracer particles. Shown is the time-averaged image behind (right) a grid with round particles (left) with elliptical particles.	43
3.11	Example of a square fractal grid.	45
3.12	Mean velocities left: across small grid elements (line 1); right: in the center of the grid (line 2)	46
3.13	turbulent intensity left: across small grid elements (line 1); right: in the center of the grid (line 2) . .	46
3.14	Comparison of the p.d.f.s underneath the fractal grids. In contrast to the free moving particle grids, there was no scaling of normalization done, since a definitive volume fraction that is comparable to real bubble swarms cannot be made. across small grid elements (line 1); right: in the center of the grid (line 2)	47
4.1	Schematic diagram of the counter current channel (left). The flow velocity is regulated by an electric valve at the end of the measuring section. In order to generate a continuous flow, the fluid is pumped back into the water basin. The turbulence generators are located between the measuring section and the nozzle. Schematic representation of the camera setup (right) with controlled background lighting. White LEDs are used as backlight for better contrast in the shadows. Published in Schlüter et al. (2021) and reprinted with permission.	50
4.2	Example of bubbles with attached Januspartikles. The left shows the bubbles and particles in a testing tube, while the right one shows that the particle are moved to the bottom pole of the bubble. .	52
4.3	Comparison of the real boundary (blue dots) and a fitted ellipse (red crosses) of a 4 mm bubble moving in turbulent flow. It can clearly be seen that the contour is not described correctly.	53
4.4	Example plot of the e-Axis (left) and the ratio of the direct and mirror major axis (right).	53
4.5	Example evaluation of the spectral analysis of the two dominant frequencies.	54
4.6	Example reconstruction. Each line represents one fit in the z -plane. The color only visualizes the heights to make it easier to see the shape.	55
4.7	Evaluation of the surface-to-volume ratio. On the left the surface-to-volume ratio is plotted over time. To the right is the according energy spectrum. From that the two dominant frequencies are determined.	56
4.8	Sketch of the reconstruction principle with a perfect circle (right) and a deformed shape (left). If only 2 cameras or views are used to reconstruct the shape, Information is lost as can be seen when comparing the right and left black line.	57

LIST OF FIGURES

4.9	Sketch of the 2D (left) and 3D (right) reconstruction principle. If four cameras are used even in 2D the shape can be approximated better than with only 2 cameras. In the right image gray lines indicate the line-of-sights of the individual characters that are intersected in space. The Boolean intersection of those lines is marked with the orange shape. The white sphere in the middle is the desired bubble.	57
5.1	Sketch of the camera setup. Two cameras are positioned in a 90-degree angle to each other and look straight through the channel glass, so no reflective index matching is necessary. To enhance the contrast on the shadow images background LEDs were installed. They were triggered to the camera images to get higher intensities.	61
5.2	Comparison of different bubble path depending on the size. From top to bottom the bubble size is increasing. The smallest bubbles had a size of 1-3 mm. The medium sized bubbles were around 3-7 mm. While the biggest one was 7-10 mm in diameter. The left column shows a top to bottom view, on the right-hand side a perspective view.	62
5.3	Schematic tomographic camera setup with triggered background light. For the visualization of the wake, background LEDs were setup to enhance the contrast and create shadow images. Snapshot of a colored wake structures behind a free rising NO bubble.	65
5.4	Different time steps of a free rising bubble with colored vortex trails. Through the chemical reaction of the NO gas and the iron in the solution a substance is formed that darkens the solution. The chemical reaction takes place on the surface of the bubble as soon as the gas diffuses through the interface. The product is then transported along the surface channel and gets trapped in the vortices behind the bubble.	65
5.5	One time step of a freely rising NO-bubble in the FeEDTA solution. The reconstruction was done analog to the one in Cha. 4. The two wakes behind the bubble are clearly visible and the wake diffuses roughly 3 bubble diameters behind the bubble. Both images show the bubble from different angles.	66
5.6	Visualization of the crow instabilities behind a zigzagging bubble. To enhance the image and increase the visibility of the instabilities the mean value over 10 images was taken.	67
5.7	Spatial temporal reconstructed particle tracks. Each time step was spatially moved according to the bubble motion. The bubble motion is marked with black x. The reconstructed volume in each time step is shifted in x,y and z direction with the bubble path.	69
6.1	Example of a path and sphere position evaluation. Both the position of the two lowest grid layers as well as the bubble path is reconstructed. The path of the bubble over the whole measurement is printed in blue. The coloring denotes the distance to the grid. The red marker shows the current position in relation to the grid. The left image shows a top view, the right image a side view of the channel. Published in Schlüter et al. (2021) and reprinted with permission.	72
6.2	Example of a path and sphere position evaluation. The height of the bubble is color coded. the spheres of the grid are hanging at the top of the graph at around 20 mm. For this measurement a medium sized bubble and a turbulence grid with 10 mm sphere and a volume fraction of 5 % was used.	73
6.3	Comparison of the estimated forces introduced by the pressure gradient through the grids. In the left image on the x-axis is plotted until the bubble diameter is big enough, that the inertia forces outweigh the pressure forces. On the right a zoom in on the range is shown for the bubble diameters that are used in this work of 10 mm beyond.	75
6.4	Example of the surface-to-volume ratio with time. The two frequencies are calculated from this with the Welch-method. The evaluation for different bubble diameters is shown in the right image. The most common frequency range is marked with grey boxes.	77

LIST OF FIGURES

6.5	One Timestep of a suspended bubble in the emulated turbulence. The color of the dots represents the velocity. For better illustration 5 additional timesteps are plotted as well. The bubbles (blue rings, but the color of the bubble is not representative and just chosen for visibility.) influence is clearly visible. The velocity behind the bubble drops to around 120 mm/s in comparison to the 300 mm/s from the counterflow.	78
6.6	Compression of the probability density function of the velocity with and without the bubble. Taken with the 3D data. The top and middle one are the p.d.f in \vec{x} and \vec{y} direction respectively. The bottom image shows the p.d.f. in \vec{z} -direction. Z is in this case also the flow direction of the counterflow. While the p.d.f.s perpendicular to the flow direction are symmetric, the p.d.f. in the counterflow direction shows a bump to positive values. In comparison to the 2D data that was shown in Cha. 3 the bump is not visible, but rather smooth.	79
6.7	Comparison of the probability density function of the fluctuations with and without the bubble. Taken from the 3D data. The top and middle one is the represent the p.d.f in \vec{x} and \vec{y} direction respectively. The bottom image shows the p.d.f. in \vec{z} -direction. \vec{z} is in this case also the flow direction of the counterflow. While the p.d.f.s perpendicular to the flow direction are symmetric, the p.d.f. in the counterflow direction shows a bump to positive values.	81
6.8	Spatial temporal reconstruction of a free rising bubble on the left and one in a counter flow setting with a 10 mm grid with a volume fraction of 5 %. In both cases was the bubble moved to the coordinate origin and the flow field displaced accordingly. In the left-hand image, the displacement in \vec{z} -direction is corresponding to the rising velocity of the bubble. In the right image the sift was calculated with the effective velocity the bubble experiences. Thus, the flow field was displaced with the sum of the bubble velocity and the mean counter flow velocity.	82
6.9	Spatial temporal reconstruction of a free rising bubble on the left and one in a counter flow setting with a 10 mm grid with a volume fraction of 5 %. In both cases was the bubble moved out of the drawing plane. In the left image, the free rising case the two counter rotating vortices can be seen forming above the bubble, marked with green to red dots. The color corresponds to the velocity. This shows that in the vortices a velocity ranges from 30 mm/s up to 100 mm/s. In the counterflow case the velocity ranges between 50 and 140 mm/s. The red dot symbolizes the bubble.	83
7.1	One time step of a freely rising NO-bubble in the FeEDTA solution. The reconstruction was done analog to the one in Cha. 3. The two wakes behind the bubble are clearly visible and the wake diffuses roughly 3 bubble diameters behind the bubble.	89

SYMBOLS

Re [-]	Raynoldsnumber
Sc [-]	Schmidt number
Pr [-]	Prandl number
d_B [m]	bubble diameter
d_p [m]	particle diameter
t [s]	time
u [cm/s]	velocity
Tu [%]	turbulence level
α [%]	void fraction
λ [nm]	laser wavelength
Λ [mm]	integral length scale

Superscripts

u'	liquid velocity fluctuations
T	transposed

Subscripts

x, y, z	quantity related to the physical x, y, z coordinate
u, v, w	velocity corresponding to the physical x, y, z coordinates
b	bubble
p	grid particle

Acronyms

2D	two-dimensional
3D	three-dimensional
FFT	F ast F ourier T ransform
PIV	p article i mage v elocimetry
EDM	e lectro- d iffusion- m easurement technique
HFA	h ot- f ilm a nomometry
PDF	p robability d ensity f unction

ABSTRACT

Haase, Katharina

Investigation of bubble dynamics in turbulent background flow.

Professor: Prof. Dr. rer. nat. habil Christian J. Kähler.

This thesis presents an experimental study of free rising bubbles and bubbles in emulated turbulence to study the interaction between the flow structures and the movement of the bubble. Of particular interest is the bubble shape and shape oscillations, since these mechanisms are important for mass transport through the bubble surface. By understanding these interactions and using these results and measurement data, the interaction between the flow structures and the bubble can be qualified and the data can also serve as a basis for numerical studies of the phenomena, but especially for improving the efficiency of chemical reactors and other industrial plants. Here for example mixing plants or medical applications.

The present dissertation is divided into three parts. First, different aspects of movement, such as the path and shape changes, are investigated. For this purpose, a new water channel was built, which allows non-intrusive optical measurements on a single bubble with and without background fluctuations. These background fluctuations are emulating swarms of bubbles and generate flow statistics similar to a swarm of bubbles. The created fluctuations are similar to those used in real industrial applications. This is achieved by different grids which are inserted into the water flow of the channel. One chapter of this thesis is dedicated to the qualification of the grids. The best results were obtained with a so-called free moving particle grid. These particles consist of spheres or ellipses of the desired bubble size, between 5 and 10 mm. These spheres are connected by a sewing thread only to the layer above. This allows the entire strand to move freely in the water flow. This emulates not only the shape of the swarm of bubbles, but also the movement of the bubbles. This makes it possible to induce a good model swarm of bubbles in the flow. Different strands (particle size, volume fraction and particle shape) were qualified with respect to flow statistics, energy spectra and probability density functions. It was found that a grid consisting of about 5 mm ellipsoids with a density of 10 % shows the best agreement with real swarms of bubbles. This was evaluated by comparison with real bubble swarms from literature data. With this model, individual bubbles in the swarm are suspended in the flow and further investigated with respect to shape oscillation and path changes. Such bubbles can be considered as moving in a swarm of bubbles.

Before the bubbles in the emulated swarm can be measured, the bubbles are examined in still water, not only to establish reference cases, but also to develop optical methods and evaluation algorithms to study shape and path oscillation. Individual bubbles were measured and the time-resolved shape, path and oscillation of the bubbles are recorded and reconstructed in 3D. The bubble size was varied between 2 mm and 6 mm to characterize all possible shape and path options. While it is known that in still water smaller bubbles show a zigzag path, larger ones follow a spiral path. Not yet reported is the bubble motion in a turbulent countercurrent flow and especially the interaction with the mentioned turbulent structures. In order to understand the shape oscillations, a new 3D reconstruction method is also introduced, which calculates the 3D shape of the bubble based on the shadow images alone. Compared to a 2D evaluation used in the literature, the 3D technique allows to study the bubble shape in an emulated background turbulence. While the 2D evaluation is sufficient for smaller, freely rising bubbles, it shows discrepancies for larger bubbles and especially for bubbles moving in an emulated turbulence. From the 3D reconstruction, the surface-volume ratio method is used to describe the shape oscillations. With the 3D evaluation it was made clear that the two frequencies used in the literature to describe the oscillations, $f_{2,0}$ and $f_{2,2}$, actually overlap in the 3D oscillation and can be measured as f_R and f_S . With these frequencies

the surface-to-volume ratio is described. These frequencies show that the bubble in the emulated turbulence experiences a reduced oscillation frequency with increasing diameter, which could not be measured with the 2D approach. The emulated turbulence impedes the natural frequency and reduces it by a factor of 3.

Furthermore, the path and movement of the bubbles and the influence of turbulence on them are investigated. The pressure gradients in the flow, caused by the velocity gradients, determine the path of the bubbles and push them into regions of low turbulence and high velocity. Furthermore, it could be shown that a critical turbulence level exists above which the bubbles are influenced by the turbulence and no longer follow their original path. This threshold was about 15 % turbulence level. By adding tracer particles to the flow, the wake structures for freely rising bubbles and bubbles in the emulated turbulence were reconstructed. While the wake of a freely ascending bubble remains for more than 20 bubble diameters, the wake behind a bubble in the turbulence is accumulated in close proximity behind the bubble in a distance of about 3-4 bubble diameters. The wakes also becomes wider and the intensity is reduced as the imposed fluctuations quickly disperse the flow.

Understanding the bubble dynamics in a swarm is especially important for mass and heat transport phenomena. To investigate this, a chemical tracer was used in collaboration with the LMU in Munich. This tracer allows to visualize the mass transport through the bubble surface and into the flow. With this tracer it could be shown that the transported species is mainly trapped in the core vortex areas of the wake. The reconstruction algorithm was also applied to this measurement and a three-dimensional representation of the wake could be reconstructed. With this reconstruction it would now also be possible to study the mass transport in the turbulent flow. However, this is an enormous experimental endeavor, which was no longer carried out in the context of this work.

KURZFASSUNG

Diese Arbeit präsentiert eine experimentelle Studie über frei aufsteigende Blasen und Blasen in emulierten Turbulenzen zur Untersuchung der Wechselwirkung zwischen der Strömungsstrukturen und die Bewegung der Blase. Besonderes Interesse gilt dabei der Blasenform und den Formschwingungen, da diese Mechanismen für den Massentransport durch die Blasenoberfläche wichtig sind. Durch das Verständnis dieser Wechselwirkungen und mit diesen Ergebnissen und Messdaten kann die Wechselwirkung zwischen den Strömungsstrukturen und der Blase qualifiziert werden, und die Daten dienen auch als Grundlage für numerische Studien der Phänomene, vor allem aber zur Verbesserung des Wirkungsgrades von chemischen Reaktoren und anderen Industrieanlagen. Hier zum Beispiel Mischanlagen oder medizinische Anwendungen.

Die vorliegende Dissertation ist in drei Teile unterteilt. Zunächst werden verschiedene Bewegungsaspekte, wie die Weg- und Formveränderungen, untersucht. Dazu wurde ein neuer Wasserkanal gebaut, der nicht intrusive optische Messungen an einer einzelnen Blase mit und ohne Hintergrundfluktuationen erlaubt. Diese Hintergrundfluktuationen sollen Blasenschwärme emulieren und eine Strömungsstatistik ähnlich einem Blasenschwarm erzeugen. Der emulierte Blasenschwarm ähnelt denen, die auch in realen industriellen Anwendungen verwendet werden. Dies wird durch verschiedene Gitter erreicht, die in den Wasserfluss des Kanals eingefügt werden. Ein Kapitel dieser Arbeit ist der Qualifizierung der Gitter gewidmet. Die besten Ergebnisse wurden mit einem so genannten frei beweglichen Partikelgitter erzielt. Diese Partikel bestehen aus Kugeln oder Ellipsen in der Größe von Blasen, zwischen 5 und 10 mm. Diese Kugeln sind mit einem Nähfaden nur mit der darüber liegenden Schicht verbunden. Damit kann sich der gesamte Strang frei im Wasserstrom bewegen. Dies emuliert nicht nur die Form des Blasenschwarmes, sondern auch die Bewegung der Blasen. Dies ermöglicht es einen guten Modelblasenschwarm in der Strömung zu induzieren. Verschiedene Stränge (Partikelgröße, Volumenanteil und Partikelform) wurden hinsichtlich Strömungsstatistik, Energiespektren und Wahrscheinlichkeitsdichtefunktionen qualifiziert. Es zeigte sich, dass ein Gitter bestehend aus etwa 5 mm Ellipsoiden mit einer Dichte von 10 % die beste Übereinstimmung mit realen Blasenschwärmen zeigt. Diese wurde durch den Vergleich mit realen Blasenschwärme aus Literaturdaten bewertet. Mit diesem Modell werden einzelne Blasen im Schwarm in der Strömung suspendiert und hinsichtlich Form Oszillation und Bahnveränderungen weiter untersucht. Solche Blasen können als sich in einem Blasenschwarm bewegend betrachtet werden.

Bevor die Blasen im emulierten Schwarm gemessen werden können, werden die Blasen in ruhendem Wasser untersucht, nicht nur, um Referenzfälle zu erstellen, sondern auch, um optische Methoden und Bewertungsalgorithmen zur Untersuchung der Form- und Weg Oszillation zu entwickeln. Einzelne Blasen wurden gemessen und die zeitaufgelöste Form, Bahn und Oszillation der Blasen werden aufgezeichnet und in 3D rekonstruiert. Die Blasengröße wurde zwischen 2 mm und 6 mm variiert, um alle möglichen Form- und Weg-Optionen zu charakterisieren. Während es bekannt ist, dass im ruhenden Wasser kleinere Blasen einen Zickzackpfad zeigen, folgen Größere einer spiralförmigen Bahn. Noch nicht berichtet wurde bis jetzt über die Blasenbewegung in einer turbulenten Gegenströmung und insbesondere die Wechselwirkungen mit den genannten turbulenten Strukturen. Um die Formschwingungen zu verstehen, wird auch eine neue 3D-Rekonstruktionsmethode eingeführt, die die 3D-Form der Blase allein auf der Grundlage der Schattenbilder berechnet. Im Vergleich zu einer 2D-Auswertung, die in der Literatur verwendet wird, ermöglicht die 3D-Technik eine Untersuchung der Blasenform in einer emulierten Hintergrundturbulenz. Während die 2D-Auswertung für kleinere, frei aufsteigende Blasen ausreichend ist, zeigt sie für größere Blasen und insbesondere für Blasen, die sich in einer emulierten Turbulenz bewegen, Diskrepanzen. Aus der 3D-Rekonstruktion wird die Methode des Oberflächen-Volumen-Verhältnisses zur Beschreibung der Formschwingungen verwendet. Mit der 3D-Auswertung wurde deutlich gemacht, dass sich die beiden Frequenzen, die in der Literatur zur Beschreibung der Schwingungen verwendet werden, $f_{2,0}$ und $f_{2,2}$ in der 3D-Schwingung tatsächlich überlagern und als f_R und f_S gemessen werden können. Mit diesen Frequenzen wird das Oberflächen-zu-Volumen-Verhältnis beschrieben. Diese Frequenzen zeigen, dass die Blase in der emulierten Turbulenz mit zunehmendem Durchmesser eine reduzierte Oszillationsfrequenz erfährt, die mit dem 2D-Ansatz nicht gemessen werden konnte. Die emulierte Turbulenz behindert die Eigenfrequenz und

reduziert sie um den Faktor 3.

Darüber hinaus werden der Weg und die Bewegung der Blasen sowie der Einfluss der Turbulenz auf diese untersucht. Die Druckgradienten in der Strömung, hervorgerufen durch die Geschwindigkeitsgradienten, bestimmen den Weg der Blasen und schieben sie in Regionen mit geringer Turbulenz und hoher Geschwindigkeit. Darüber hinaus konnte gezeigt werden, dass ein kritisches Turbulenzniveau existiert, oberhalb dessen die Blasen durch die Turbulenz beeinflusst werden und nicht mehr ihrem ursprünglichen Weg folgen. Diese Schwelle lag bei etwa 15 % Turbulenzniveau. Durch Zugabe von Tracer Partikeln in die Strömung wurden die Nachlaufstrukturen für frei aufsteigende Blasen und Blasen in der emulierten Turbulenz rekonstruiert. Während der Nachlauf einer frei aufsteigenden Blase für mehr als 20 Blasendurchmesser bestehen bleibt, wird der Nachlauf hinter einer Blase in der Turbulenz in unmittelbarer Nähe hinter der Blase in einem Abstand von etwa 3-4 Blasendurchmessern akkumuliert. Der Sog wird auch breiter und die Intensität wird verringert, da die auferlegten Fluktuationen die Strömung schnell zerstreuen.

Das Verständnis der Blasendynamik in einem Schwarm ist besonders wichtig für Massen- und Wärmetransportphänomene. Um dies zu untersuchen, wurde in Zusammenarbeit mit der LMU in München ein chemischer Tracer eingesetzt. Dieser Tracer erlaubt es, den Massentransport durch die Blasenoberfläche und in die Strömung zu visualisieren. Mit diesem Tracer konnte gezeigt werden, dass die transportierte Spezies hauptsächlich in den Kernwirbelbereichen der Wirbelschleppes gefangen ist. Der Rekonstruktionsalgorithmus wurde ebenfalls auf diese Messung angewendet und es konnte eine dreidimensionale Darstellung des Nachlaufes rekonstruiert werden. Mit dieser Rekonstruktion wäre es nun auch möglich den Massentransport in der turbulenten Strömung zu untersuchen. Jedoch stellt dies ein enormes Experimentelles Unterfangen dar, dass im Rahmen dieser Arbeit nicht mehr durchgeführt wurde.

1 General aspects of a single bubble rising in water

1.1 Introduction - Bubbles in the real world

Multiphase flows are the combination of two different phases, like water and solid particles, air in liquid or even liquids with different density. One very prominent example is gas bubbles in liquid that can occur in various places in everyday life, for example in soft drinks, water vapor in boiling water or in sea foam. But they also find use in various industrial or scientific applications and also in the energy sectors. Examples are bioreactors, steel melts or nuclear power plants. Bubbles are often used as punctiform mass sources to supply a liquid with substances at the right time, but also for mixing purposes. The main reason for it is that, bubble-induced turbulence leads to a gentler blending compared to mechanical stirring tools. This becomes necessary if large shear stresses in the flow would impair the product quality, or if steering with mechanical agitating tools is too complex and expensive due to the size of the reactor plants. Most often mixing processes are needed to improve chemical reactions or heat transfer to enable certain processes or increase the selectivity of the desired reactions. In most applications, bubbles up to 10 mm in size are used in swarms with around 18% volume fraction (Deckwer 1985). To efficiently build mixing reactors however, it is necessary to fully understand the flow behavior in bubble swarms and their interaction with each other and how the mass transport from the gaseous phase is influenced. The experimental and numerical analysis of such high-density bubble swarms and its flow statistics are still an enormous methodical challenge and is coupled with a high amount of computational power. Besides the flow statistics the mass transport processes are of great interest and are studied by many research groups.

In particular, the influence of swarm turbulence on the dynamics of the individual bubbles and the mass transfer across the phase boundary into the fluid are of fundamental importance for the design of reactors to increase either the product quality or product yield. Until today, only mechanical probes can be used in such swarms, e.g. for local measurement of the enriched substance, since optical methods do not provide reliable results due to the shadowing by the bubble swarms. Since probes always interfere with the flows within the plants and influence the measurement results and only measure in a single local point a different approach based on a non-intrusive technique is needed. The use of non-contact optical methods is desirable in order to gain more detailed and precise knowledge about the processes and their interactions. Of special interest is the interaction of a bubble in this swarm and how the induced flow fluctuations of the swarm are influencing this bubble.

To investigate this a new measurement channel was built that is designed to allow to create a model turbulence with statistics similar to real bubble swarms. By releasing a single bubble in this emulated turbulence measurements of a single bubble can be conducted as if they were moving in a swarm. This thesis will present different approaches to create this model turbulence and the measurement techniques to conduct the experiments to study not only the flow itself, but also the interaction of the bubbles shape and the fluctuations. To do this the following questions will be answered over the course of the thesis.

- What is a good experimental model to emulate swarm like turbulence? How can a swarm be emulated and induced in a flow? How does it need to be characterized, to compare to real bubble agitations?
- How can a single bubble be measured without intrusive techniques? How can a single bubble be accurately described and the surface be reconstructed? Can the flow around the bubble be measured simultaneously and how are they affecting each other?

- How do bubbles behave in this emulated swarm turbulence compared to free rising bubbles? What is the difference compared to a free rising bubble?

1.2 Bubbles and how to describe them

Bubble swarms and their inner workings are still an ongoing topic for different research groups and are of great interest for industrial applications, which lead to a wide variety of publications for example from groups in Toulouse or Seoul covering different aspects of bubbly agitations and swarm dynamics. While a variety of information is widely available it becomes clear that only single aspects of either a single bubble or a swarm of bubbles is investigated. This chapter will give an overview of the different aspects of the bubble dynamics and swarm behaviors but will also place this thesis in context with the existing literature and show where the presented data is placed in and on what aspects it wants to improve on.

1.2.1 Different bubble shapes, velocity and path

In the literature bubbles are often also called particles, since the same physics applies to droplets as well. In [Clift et al. \(1978\)](#) for example a particle is described as a self-contained body with a maximum dimension, which is surrounded by a recognizable interface. Since this thesis solely focuses on bubbles, they will be referred to as such in comparison to some literature that is cited. The material forming the bubble will be termed the 'dispersed phase' (subscript b), the surrounding one 'continuous phase' (no subscript). In this work the continuous phase is always a Newtonian fluid and if not otherwise stated, it is clean distilled water. The easiest case to study is a single rising bubble without interaction with other bubbles or any surface, like channel walls etc. In order to describe the behavior of a single rising bubble, the following chapter is separated into two parts. The first part will go into more detail about how the bubble itself is behaving, especially the shape and movement of the bubbles surface. The second part will focus on the flow of the liquid around the bubble, the induced wake structures and interactions between the bubble and the flow.

The shape of the bubble and its behavior is depending on many factors, like the size or the surface tension between the two phases. Extensive research has been done regarding this topic, among those the most notable are the following: [Brücker \(1999\)](#), [Veldhuis et al. \(2008\)](#), [Lauterborn & Kurz \(2010\)](#), [Magnaudet & Eames \(2000\)](#), [Lunde & Perkins \(1995\)](#) and more. One way to describe the shape is with the aspect ratio E , defined as the ratio of the major and minor axis, where $E = 1$ describes a spheroid. Is $E < 1$ the bubble has the shape of an oblate spheroid and for $E > 1$ that of a prolate spheroid. Some of the bubbles in this work can be described as axisymmetric bodies. The shape is created by a closed curve around an axis. Small bubbles are closely resembled by a spheroidal shape. But most are irregular in shape and cannot be categorized easily. In [Fig. 1.1](#) a sketch of a bubble is shown how the axis will be labeled and referred to in the following.

Depending on the shape the bubbles describe different paths due to their induced wakes and differences in the pressure gradient. The shape and general motion of a rising bubble is also affected by the container walls. Unless otherwise expressed the wall effects can be neglected in all experiments shown here, if the wall effects are taken into account it is stated. With increasing size, the rising velocity also increases. The smallest bubbles of around 0.2 mm rise with a mean velocity of 200 mm/s, which increases to almost 380 mm/s for diameter of 1.5 mm. The velocity again decreases until 7 mm down to 210 mm/s. Does the bubble diameter increase again, so does the velocity. Many publications measured this correlation the most prominent graph is published in [Clift et al. \(1978\)](#). It also shows the dependency on the purity of water and describes the influence of surfactants.

From the correlation ([Eq. 1.1](#)) the rise velocity depending on the equivalent diameter can be estimated with the following equation. U_T notes the terminal rise velocity, σ the surface tension between the gas and the liquid, ρ the density of the disperse phase, g the gravitational constant and d_b the bubble equivalent diameter. The equation was taken from [Clift et al. \(1978\)](#).

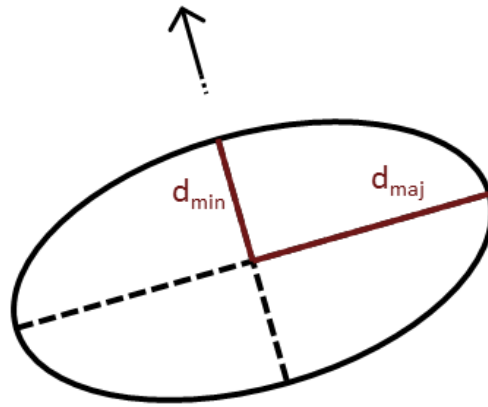


Figure 1.1: Sketch of a single bubble with the definition of the axis.

$$U_T = [(2.14 \sigma / \rho d_b) + 0.505 g d_b]^{1/2} \quad (1.1)$$

Several publications studied the bubble motions and supply overviews. Most noticeably are [Clift et al. \(1978\)](#), [Saffman \(1956\)](#), [Riboux et al. \(2013\)](#), [Brücker \(1999\)](#), [Tomiyama et al. \(1993\)](#), [Tomiyama et al. \(2003\)](#) and others. These bring the shape with the rising path into correlation. In literature three distinguishable forms of the rising path are described [Clift et al. \(1978\)](#). Straight rising, spiraling and zigzagging bubbles, each are having their own signature length- and timescales. The simplest form of rising is the rectilinear path performed by small bubbles. Thereafter, with increasing diameter, bubbles first become oblate spheroids and follow a helical path. With further increasing diameter, shape oscillation starting to occur and the bubble moves in a zigzagging motion. Finally, the bubble has the form of a spherical cap, rising rectilinear or even chaotic. In the following a short description of the spiraling and zigzagging bubbles is given, since those are the two prominent structures that were observed and investigated in this thesis.

Table 1.1: Motion of medium sized bubbles in relation to the Reynolds-number ([Clift et al. 1978](#), [Aybers & Tapucu 1969](#))

d_e (mm)	Re	aspect ratio \bar{E}	Path and description
<1.3	<565	>0.8	sphere, Rectilinear,
1.3 to 2.0	565 to 880	0.8 to 0.5	oblate spheroid, helical
2.0 to 3.6	880 to 1350	0.5 to 0.36	Plane (zig-zag) then helical
3.6 to 4.2	1350 to 1510	0.36 to 0.28	irregular oblate sphere, Plane(zig-zag)
4.2 to 17	1510 to 4700	0.28 to 0.23	transition from oblate sphere to spherical cap, rectilinear but with rocking

Force balance and equation of motion

Before the individual bubble shapes are discussed, a quick overview of the governing forces shall be presented. The easiest case is to treat the bubble as a particle with an effective mass, so the trajectory and the forces on the bubble can be described as follows:

- Buoyancy force

The buoyancy force is the driving force that is responsible for the rise of the bubble (density ρ_b and radius r_b) in a liquid (density ρ). The force F_b can be written as following, with g as the acceleration due to the gravity:

$$F_b = -4/3 \pi r_b^3 (\rho - \rho_b) g \quad (1.2)$$

Since the density of the bubble is much smaller than the density of the liquid one could neglect the bubble density and solely use the density of the liquid.

- Drag force

Once the bubble reaches the terminal rise velocity the buoyancy force is countered by the hydrodynamic forces. If the water is contaminated with surfactants the bubble behaves similar to a rigid sphere, because the surfactants render the hydrodynamic forces tangentially immobile. With this, the drag force can be written as:

$$F_d = \pi/4 C_d \text{Re} \mu r_b u_b \quad (1.3)$$

The drag coefficient C_d can be derived from the Schiller and Naumann formula for a solid sphere ([Hendrix et al. 2012](#), [Manica et al. 2013, 2014](#)):

$$C_d = (24/\text{Re})(1 + 0.15 \cdot \text{Re}^{0.687}) \quad (1.4)$$

This approach describes the coefficient well up to Reynolds numbers up to 800 for spheres ([Klaseboer et al. 2014](#)).

- Inertial forces (added mass)

The inertia of the fluid surrounding a bubble can be described with an added mass. Is a constant bubble size assumed the inertial force can be written as, with the added mass coefficient $C_m(\infty)$:

$$F_p^\infty = \frac{4\pi}{3} \rho r_b^3 C_m(\infty) \frac{du(t)}{dt} \quad (1.5)$$

- History or Basset force

is the velocity changing with time a force depending on the acceleration can be derived from the Navier-Stokes equation. This force $F_h(t)$ can be written as:

$$F_h = 6\sqrt{\pi\mu\rho} r^2 \int_{-\infty}^t \frac{1}{\sqrt{t-\tau}} \frac{dU(\tau)}{d\tau} d\tau \quad (1.6)$$

The assumption of the immobile boundary condition is consistent with the use of the Schiller and Naumann formula. On the other hand, the sphere surface has zero tangential stress boundary condition, the magnitude of the history force is considerably smaller compared to the other forces.

Rectilinear bubbles (<1.3 mm)

Many publications describe the simplest form of the rising path, the rectilinear path. It is in most cases the initial rising path of the bubble and once it reaches the terminal rise velocity the bubble goes into the subsequent bubble motion. If Re is smaller than 565, the bubble keeps rising in a rectilinear motion (Aybers & Tapucu 1969). By comparison with other publications this number is more a range than a fixed value. This value is mainly depending on the system purity. Clift et al. (1978) for example gives a value of 360. The rising velocity can easily be calculated by the Stokes equation with a force balance between the inertia, the buoyancy and the mass.

$$F_{\text{inertia}} = 6\pi r_b \eta u_b \quad (1.7)$$

$$F_{\text{buoyancy}} = \rho V g \quad (1.8)$$

$$F_{\text{mass}} = \rho V_b g \quad (1.9)$$

From that the rising velocity can be calculated to be:

$$u_b = 2/9 \frac{r_b^2 g (\rho_b - \rho)}{\eta} \quad (1.10)$$

Spiraling bubbles (<4 mm, $Re \approx 360$)

Bubbles with a diameter smaller than 4 mm start to exhibit a spiraling motion. The shape-aspect ratio can be measured to be around $E = 0.8$. Several path characteristics can be found in various literature. For example, Lunde & Perkins (1995) describes a spiral in the horizontal plane with an amplitude of 3 mm and a frequency of 5.8 Hz from which the lateral velocity was estimated to be about 110 mm/s. According formula Eq. 1.1 a mean rising velocity for spiraling bubbles can be estimated around $U_T = 270$ mm/s. This results in a Reynolds number of around $Re = 360$, and a Strouhal number of $Sr = 0.08$. By observing the bubble shape in relation to the path it is clear that the bubble, an oblate sphere in this case, tilts with each turn of the helix. The spheroid is not only tilted in the tangential plane but is also tilted towards the center of the spiral. This motion is induced by the pressure gradient in the flow around the bubble similar to the zigzagging motion. A pair of counter-rotating vortices are observed like sketched in Fig. 1.2. Due to the additional tilt in the bubble the vortices are placed out of center of the bubbles and moved more to the outer side of the helix motion. Further the strength of these two pairs is not equal and placed asymmetrical to one another. It appears that the inner vortex dominates the flow and dictates the motion, while the outer vortex has a lower strength and is stretched tangentially. This acts as a lift force and results in the lateral motion and the displacement to the outer vortex forces then the bubble on a helical path, similar to a centripetal force. The wake and the motion are consistent over time.

Zigzagging bubbles (5 mm - 7 mm, $Re \approx 1320$)

Closest to the rectilinear motion is the zigzagging motion. For bubbles with a diameter between 5 mm and 7 mm the bubbles perform a regular unidirectional zigzag motion in one plane. In publications this zigzag is described as a sinus function with a frequency of 4.2 Hz and an amplitude of 1.3 bubble diameter (Brücker 1999). The velocity in the horizontal plane is $u_T = 100$ mm/s with a Strouhal number of $Sr = 0.11$ ($Sr = fr/u_T$). The long axis is tilted to be perpendicular to the path. In the turning points of the path the ellipses deform to a sphere and to an ellipse again until the next turning point. This is a result from uneven pressure distribution around the equator of the bubble induced by the flow around it (Brücker 1999). A symmetric oscillation is superimposed in the aspect ratio with a amplitude of roughly 10 % of the maximum diameter with double the frequency of the motion. Lunde & Perkins (1995) correlate these oscillations to capillary waves traveling over the surface of the bubble. Brücker (1999) on the other hand correlates these to the variation in the spacing of the hairpin vortices.

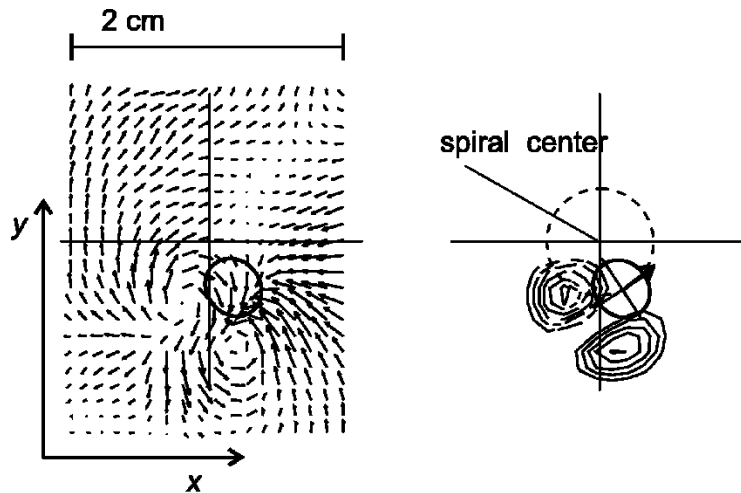


Figure 1.2: Velocity field and streamwise vorticity distribution in a horizontal plane downstream of a spiraling bubble at $Re = 5360$. The bubble spirals in the horizontal plane along the dashed line around the center of the cross. The direction of lateral bubble motion is indicated by the arrow. Left: velocity field $y(x,y)$ ($u_{max} = 300$ mm/s); right: regions of concentrated streamwise vorticity u_z (contour lines start from ± 5 mm/s in steps of 2 mm/s; solid line: positive value, dashed lines: negative value). Reproduced from Brückner (1999), with the permission of AIP Publishing.

In Lunde & Perkins (1995) it is shown that the frequency is dependent of the diameter and can be correlated like shown in Fig. 1.6. A more detailed description can be found later in Cha. 6.

actually In Fig. 1.4 the wake structure of a freely rising bubble at a Reynolds number of $Re = 1500$ is shown. The visualization shows a hairpin like vortex whose legs are attached to the base of the bubble while the head of the hairpin points downstream to the left. In Fig. 1.3 PIV flow field measurements of horizontal cross sections in the bubbles wake at different stages in the bubble path are sketched. The zigzagging bubble starts to rise from the left to the right out of the drawing plane in z -direction. The head of the bubble is marked by the solid line. The images were spatially temporally corrected with the free stream velocity by Brückner (1999) to show the correlation between the shape and the flow. With this shift based on the Taylor hypothesis time resolved data can be corrected by a spatial shift to create a pseudo 3D view of the flow. This means that the bubble is not necessarily still in the measurement plane.

Brückner shows in Fig. 1.3 (taken from Brückner (1999)) that at the beginning of the measurement in (A) the bubble is close to the stagnation point on the left side of the motion and starts to rise to the right. The hairpin vortex is starting to form as indicated by the small vortices to the left of the bubble. If the bubble is now entering the path where it can freely rise (B), the two counter rotating vortices start to grow and the legs start to develop. The pressure on the left side starts to increase due to the vortices and create a lift force that pushes the bubble to the right. The vortex pairs are still attached to the rear of the bubble and follow it, but the distance increases (C-D). With time the vortices start to dissolve and lose strength which decelerates the movement of the bubble, the bubble reaches the second stagnation point on the right side; the first pair of vortices is now weak enough, so that a new set of pairs starts to form on the opposite site. In image (E) the generation of a new vortex pair is seen. The same approach as for Fig. 1.4 was taken to create vertical cuts through the wake structures of the bubbles wake, as seen in Fig. 1.4 in the bottom two images. The two counterrotating vortices are shown as the flow field (left column) and as isolines of the vorticity (right column). The process from here on out is repeated and the bubble is pushed to the left-hand side. This finally results in a zigzagging motion with alternating left and right vortex pairs. These pairs introduce lift forces onto the bubble that pushes the bubble into this characteristic

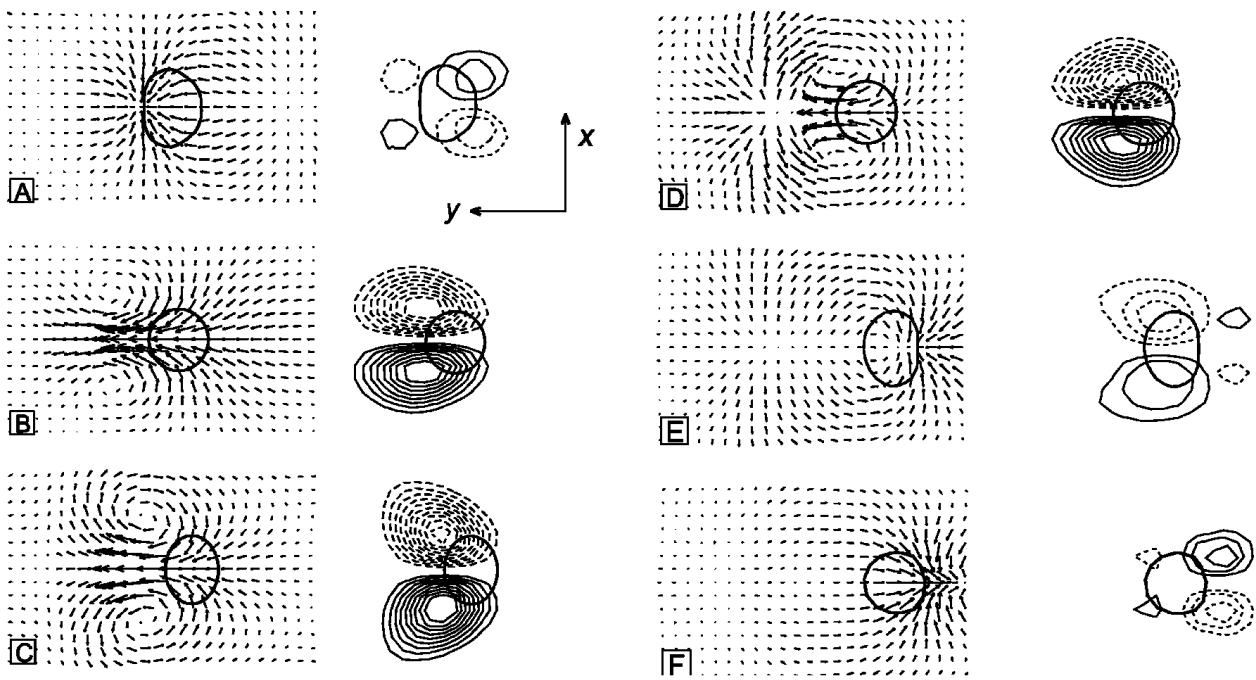


Figure 1.3: Evolution of the velocity field and stream wise vorticity distribution in a horizontal plane 10 mm downstream of the zigzagging bubble for the moments (A)(F). The zigzagging motion of the bubble in the horizontal plane is along the y axis. Left column: velocity field $y(x,y)$ ($v_{\max} = 70\text{mm/s}$); right column: regions of concentrated stream wise vorticity ω_z (contour lines start from $\pm 1/s$ in steps of $1/s$; solid line: positive value, dashed lines: negative value). Reproduced from [Brücker \(1999\)](#), with the permission of AIP Publishing.

motion.

1.2.2 Bubbles in dimensionless numbers

The rising path and velocity of the bubbles are a coupled and influence each other. The motion can in general be described by dimensionless numbers like the Reynolds number Re , the Weber number We and the Etvös number Eo . With these, comparability between different experiments can be created. Countless of these numbers can be used to describe fluid dynamics. Five of them play an important role in the multiphase flow and in this thesis and will be further discussed here. In [Eq. 1.11](#) - [Eq. 1.13](#) the symbols are defined as followed: ρ is the density, d_b the bubbles equivalent diameter, u the vertical rise velocity, μ the dynamic viscosity, σ the surface tension and g the gravitational acceleration.

$$Re = \frac{\rho d_b u}{\mu} = \frac{\text{fluid's inertia}}{\text{viscosity}} \quad (1.11)$$

The Reynolds Number Re is the ratio between the inertial forces in a fluid and the viscous forces. It is used to predict flow patterns. At low Reynolds numbers the flow is laminar while flows with higher Reynolds numbers are turbulent. For bubbly flow the equivalent diameter is usually used as a characteristic length and ranges from 500 for small bubbles (~ 10 mm) to 5000 for bubbles in the range of 10 mm.

$$We = \frac{\rho u^2 d_b}{\sigma} = \frac{\text{fluid's inertia}}{\text{surface tension}} \quad (1.12)$$

The Weber Number We is used to describe interfaces with high curvatures, like bubble and droplets and is the ratio of the fluid's inertia to the surface tension. It is also often also written as the ratio between the kinetic energy and the surface energy.

$$Eo = \frac{\Delta\rho d_b^2 g}{\sigma} = \frac{\text{gravitational forces}}{\text{surface tension}} \quad (1.13)$$

The Eötvös Number Eo also called Bond Number Bo is used to characterize the shape of bubbles and droplets and is defined as the ratio of the capillary forces to gravitational forces. In [Clift et al. \(1978\)](#) a figure correlating the rise velocity with the Etvös number and the bubble diameter is given.

$$Sc = \frac{\nu}{D} = \frac{\mu}{\rho D} = \frac{\text{viscous diffusion rate}}{\text{molecular (mass) diffusion rate}} \quad (1.14)$$

The Schmidt number Sc describes the ratio of the momentum diffusivity (kinematic viscosity) and the mass diffusivity. The Schmidt number describes the processes in which both momentum as well as mass transport takes place. For bubbles the Schmidt number is around or smaller than 0.1.

To fully describe all the processes that take place in a bubbly flow or even at the interface layer of a single bubble several additional numbers are required, like the Prandtl number, the Lewis number, the Nusselt number, the Sherwood number or the Peclet number. Since neither the mass transport nor the heat transport is studied in great detail in this work, these are just mentioned here. Further information about those numbers can be found in a variate of publications.

1.2.3 Shape oscillations

The topic of shape oscillations has been a prominent subject in both experimental and numerical publications like [Tsamopoulos & Brown \(1983\)](#), [Wang et al. \(1987\)](#), [Brücker \(1999\)](#), [Reddy & Szeri \(2002\)](#) and [Veldhuis et al. \(2008\)](#) with numerical studies from [Prosperetti et al. \(1988\)](#). In the last few decades this topic has been

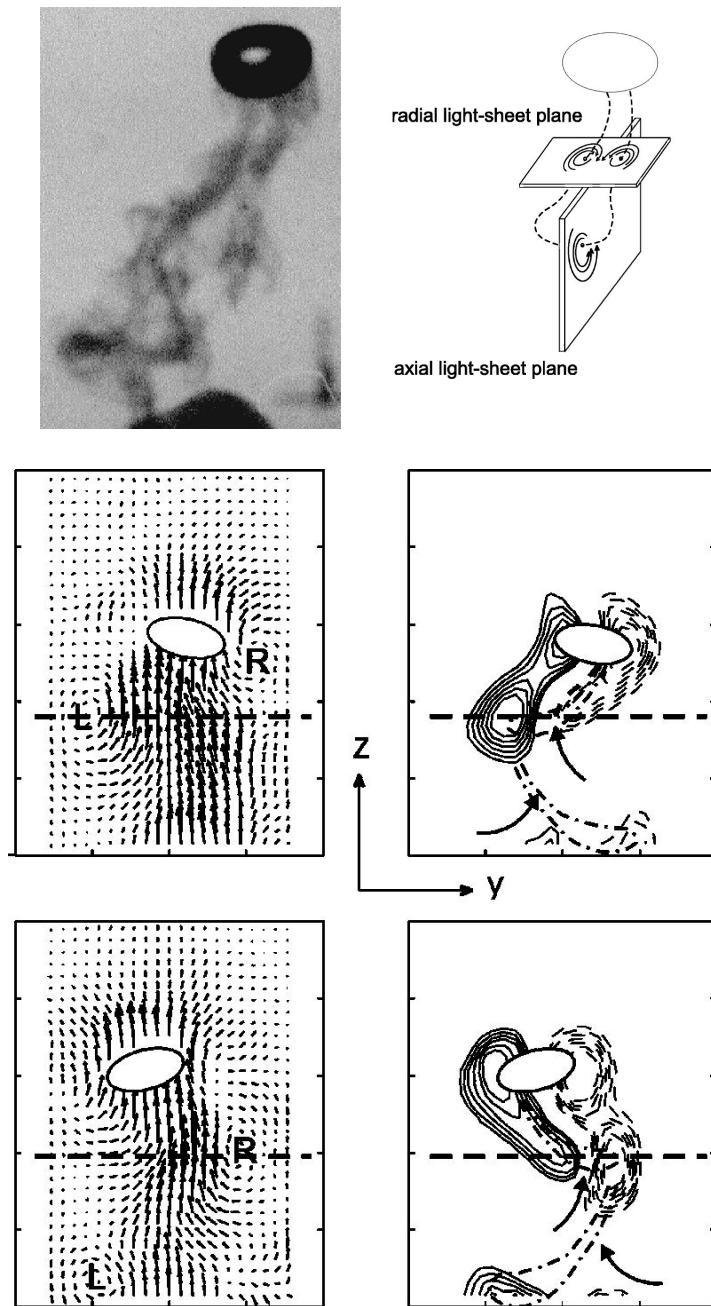


Figure 1.4: Top images: Visualization of a colored vortex and schematic interpretation in the cross section for a rocking bubble $Re = 1500$. Bottom four images: Spatial-Temporally reconstructed vertical flow around a spiraling bubble. The solid line indicates the position of the bubble. The dashed line indicates the measurement plane. The left column shows the velocity, while the right shows the according isolines of the vorticity. Reproduced from [Brücker \(1999\)](#), with the permission of AIP Publishing.

discussed in a various number of literature, in [Loth \(2008\)](#) and [Liu et al. \(2005\)](#) an overview over this topic can be found. In this case, the deformations are of small amplitude and the oscillations can be described in terms of spherical harmonics. It is stated, that the distribution and the connected local flow field rather than the volume fraction or the average turbulent kinetic energy are responsible for the bubble shape.

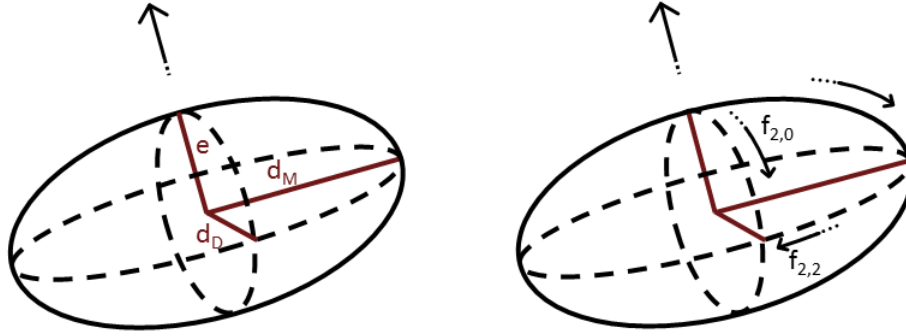


Figure 1.5: Sketch to visualize axis definitions used in this work (left side) and the mode $f_{2,0}$ and $f_{2,2}$ waves (right side). The $f_{2,0}$ waves are moving from the front to the rear stagnation points (from pole the pole), and mode $f_{2,2}$ waves are traveling around the equator of the bubbles.

If larger bubbles are considered, the amplitude of the oscillations leads to non-linear effects, as the inviscid frequency shift described by [Tsamopoulos & Brown \(1983\)](#) and [Hartunian & Sears \(1957\)](#). They studied large scale lateral motion of bubbles, following mainly zigzagging and spiraling paths, and suggested that an interaction between capillary shape oscillations and the translation of the bubble are responsible for the behavior. The shape of a bubble fluctuates in response to oscillations in the pressure field and in the liquid surrounding the bubble. The intermittent vortex shedding associated with the lateral motion of bubbles, see, e.g., [De Vries \(2001\)](#), will cause regular fluctuations in the velocity and therefore in the pressure field around the bubble. In their review on bubble wakes, [Fan & Tsuchiya \(1990\)](#) refer to several instances where the shape of (mainly large) bubbles was observed to oscillate at the frequency of the lateral motion. It is evident that the shape of a bubble fluctuates as a result of the turbulent shear and pressure forces of the surrounding liquid. In addition to that, the coupled vortex shedding behind rising bubbles leads to lateral motion of the bubbles, inducing drag and lift forces on the bubbles.+

To describe these oscillations, two different modes are discussed in the literature: the oscillations in the equivalent major axis e , named mode $f_{2,0}$ and the axes ratio R , as mode $f_{2,2}$. In [Lunde & Perkins \(1998\)](#), a simple model is described linking the shape oscillations to capillary waves traveling on the bubble surface. The $f_{2,0}$ waves are moving from the front to the rear stagnation points (from pole the pole), and mode $f_{2,2}$ waves are traveling around the equator of the bubbles. In [Fig. 1.5](#) a sketch visualizing the two modes is shown. It is further described in [Lunde & Perkins \(1998\)](#) that the modes correlate with the bubble volume and deformation. It is also noted that the $f_{2,0}$ mode has a strong correlation with the motion of the bubble itself. The $f_{2,2}$ mode however does not show any relation to the bubble motion.

The frequencies of the oscillations can be formulated in terms of the spherical equivalent diameter r_e and the ellipticity ϵ . This formula λ denotes the wavelength, with the mode n around $f_{2,0}$ and $f_{2,2}$ frequencies can be calculated according to [Lunde & Perkins \(1998\)](#) as follows:

$$f_{2,0} = \frac{1}{2\pi} \sqrt{\frac{16\sqrt{2}\epsilon^2\sigma}{\rho_L(\epsilon^2+1)^{3/2}r_e^3}} \quad (1.15)$$

$$f_{2,2} = \frac{1}{2\pi} \sqrt{\frac{8\sigma}{\rho_L \epsilon r_\epsilon^3}} \quad (1.16)$$

In Fig. 1.6 the dependency on the two frequencies with the radius is shown. The two modes are compared to each other and also with a calculation for a sphere. The calculation is plotted with dashed lines. The two solid lines are calculated with Eq. 1.15 and Eq. 1.16, while the marks are taken from measurements. It is easy to see that for a sphere the two frequencies fall together. While for elliptical bodies, like the bubbles the two frequencies are different, with mode 2,0 being higher by 40 Hz for small radii and 10 Hz for bigger ones of around 2.5 mm. It is also stated that for even higher radii these two frequencies fall together and are not measurable anymore. In addition, the vortex shedding is marked with open squares and show the frequencies in which the shading takes places. For all bubble diameters the shading is in the range of 15 Hz. The evaluation and calculation of the frequencies was done via analyzing two orthogonal images and calculating the frequencies from those.

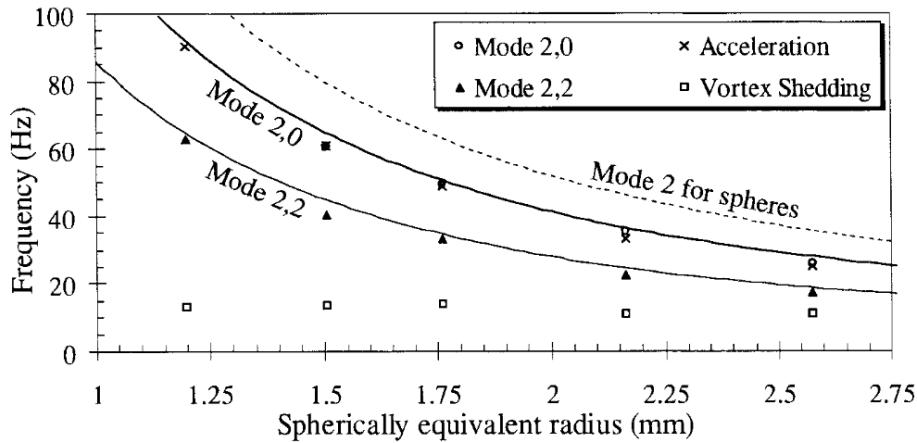


Figure 1.6: Change in the oscillation frequencies depending on the spherical equivalent radius. Taken from Lunde & Perkins (1998), with permission from Springer Nature.

1.2.4 Flow and turbulence of a rising bubble swarm

So far only single bubbles rising in quiescent waters have been described, However, no single bubbles, but swarms of bubbles are used in industrial applications to induce certain mixing effects by their induced swarm turbulence. This section will give a short overview over the literature, since and in-depth analysis will be given later in Cha. 3.

Velocity profile

It is well-known that bubbly flow with a low gas volume fraction is similar to a laminar velocity profile, but with increasing volume fraction α , a modification of the laminar flow profile can be observed (Hosokawa & Tomiyama 2013). In a fully developed bubble flow, the rise velocity of the bubble swarm is nearly constant over the cross section of a channel with a slight decrease in the near-wall region because of the boundary layers at the channel walls (Hosokawa & Tomiyama 2013). Thus, the liquid velocity is mainly determined by the void fraction α . At low to moderate volume fractions the bubbles are distributed stochastically which results in a velocity profile resembling a turbulent flow (Liu et al. 2005, Risso & Ellingsen 2002). With increasing volume

fraction, the shape deviates from the flat profile and the mean velocity lowers at the core and rises again slightly with the radial distance until the wall boundary effects decrease the velocity again. This can be seen in Fig. 1.7 in image (a), (c) and (e). Between those three the distance to the swarm is increased, showing that the profile closer to the bubble bulk is more irregular than the further downstream, when the velocity settles and is fully developed. Images (b), (d) and (f) plot the velocity in radial direction across the swarm. Again, the distance is increasing from top to bottom. The asymmetric shape is explained by the chosen coordinate system that is symmetric to the middle of the swarm or water container.

Kim et al. (2016) as well as Riboux et al. (2009) suggest that the bubble rise velocity decreases with increasing volume fraction. Riboux additionally states in his publication that the velocity scales with $\alpha^{-0.1}$.

The liquid velocity in vertical direction is mostly determined by the local volume fraction and instantaneous bubble distribution. The liquid velocity is higher in regions with a higher bubble density, due to the acceleration caused by the bubbles. This was shown by experiments done by Kim et al. (2016). The bubbles migrated first to that side due to the dominant radial velocity. With increasing volume fraction the profile becomes more symmetric; the radial component decreases and becomes irrelevant for the bubble movement.

Velocity fluctuations and turbulence

In Fig. 1.8 a comparison of the vertical and radial velocity fluctuations with a fully developed single phase flow is made. The image was taken with permission from Kim et al. (2016). Again (a), (c) and (e) plot the fluctuations in z direction across the channel with increasing distance to the swarm. (b), (d) and (f) the same for the radial fluctuations. The fluctuations in vertical and horizontal directions for real bubble and flows are comparable to each other due to the oscillating path of bubbles, even though the main flow direction is vertical (Lance & Bataille 1991). Already at low volume fractions the bubbles introduce a great amount of fluctuations to the system. Both the radial and vertical components seem to develop a plateau in the channel center with increasing volume fraction. In comparison to single flow turbulence, which shows a convex center line and peaks towards the wall, the bubble flow in comparison shows a wide plateau and no peaks towards the wall. This is explained with the bubbles in the wall region lowering the velocity fluctuations in contrast to the center region. Due to the bubbles present the shear induced turbulence is almost negligible and the turbulence is characteristic for bubble induced turbulence and is also called bubble induced agitation. According to Lance & Bataille (1991) and (Wang et al. 1987), the turbulence level for swarms with 2 % is ~ 6 % for swarms with a low volume fraction of 2 %. Further criteria like energy spectra, probability density functions (p.d.f.) and other statics will be summarized here, but are also described and evaluated in more detail in Cha. 3.

Probability density function and a physical interpretation of it

Many publications regarding this topic were made by the group from Toulouse (Riboux et al. 2009, 2013, Risso & Ellingsen 2002, Risso et al. 2008a, Risso 2016). One of the experiments they performed to measure the flow statistics behind a bubble swarm was to do PIV measurements behind a free rising swarm and recorded the flow immediately after the swarm has passed (Riboux et al. 2009). Several different bubble diameters, and volume fractions were tested. The PIV data was used to calculate the fluctuations and the probability density function calculated from it. To compare the different volume fractions a normalization factor was introduced. The velocity was first normalized by the rising velocity of a single bubble and then multiplied by $(\alpha/0.01)^{-0.4}$. This is done to collapse all the functions onto each other.

As can be seen in Fig. 1.9 the p.d.f.s in flow direction (a), (b) and (c) on the left side, are showing a long foot to the right, while the ones in spanwise direction are symmetric (right column). This is explained by the large upward fluctuations caused by the bubble wakes, while the flow and also the fluctuations in the horizontal

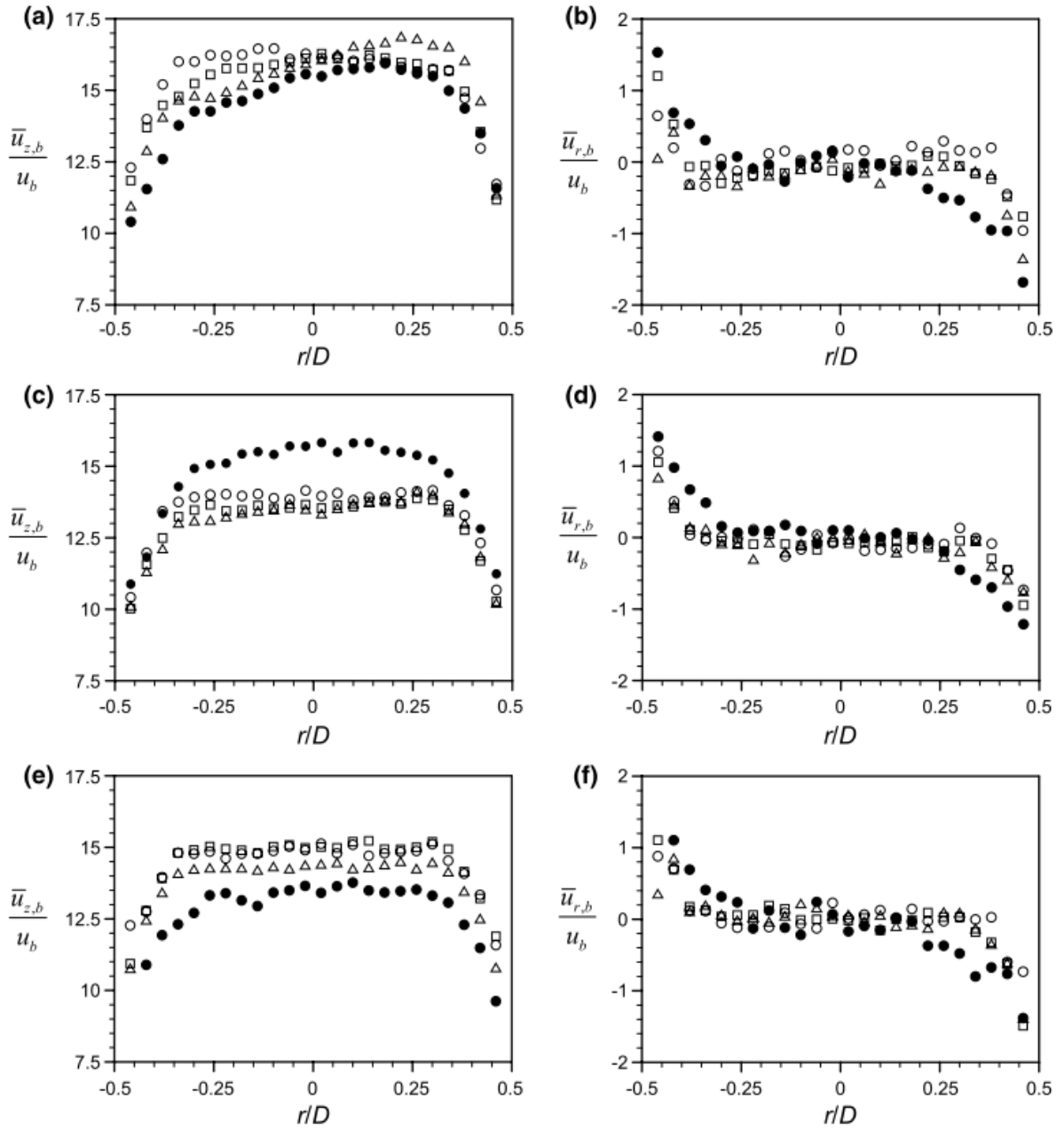


Figure 1.7: Velocity in a cross-section of a container, normalized by the mean bulk velocity. (a), (c), (e) shows the vertical velocity, and (b), (d), (f) the radial one. From top to bottom the distance to the bubble swarm was increased. From top to bottom the measurement position is rather away from the injection point of the swarm. The marker type indicates different bubble swarm densities. The open circle has a volume fraction of α [%] 0.05, the open squares 0.1, the open triangles 0.17 and the filled circles 0.64. The image is taken with permission from [Kim et al. \(2016\)](#).

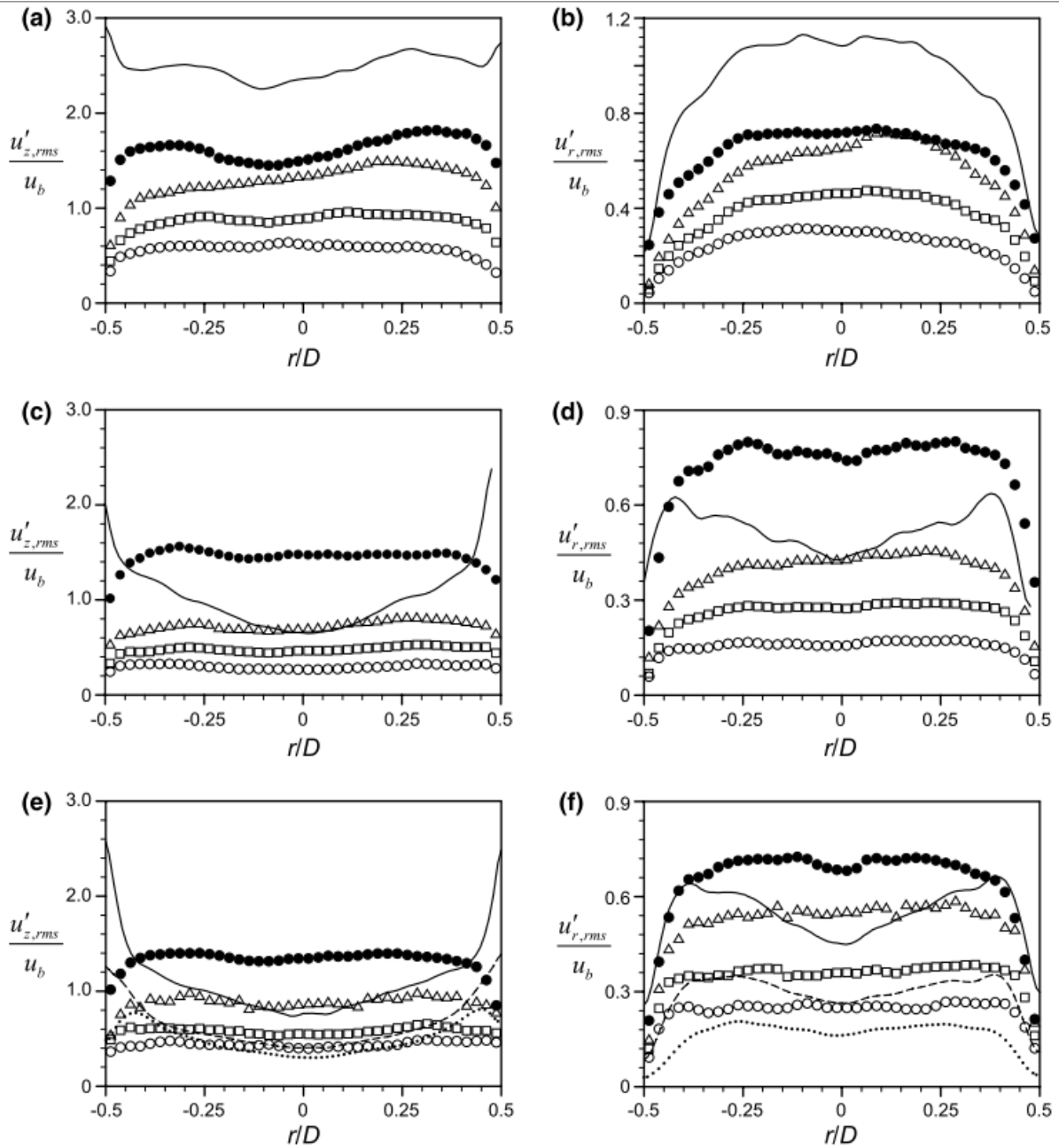


Figure 1.8: Velocity fluctuations in the liquid phase normalized by the bulk velocity. In the left column are the vertical fluctuations plotted with a comparison to single phase flows. In the right column the radial fluctuations are compared to single phase flows at different Reynolds numbers. From top to bottom the measurement position is rather away from the injection point of the swarm. The marker type indicates different bubble swarm densities. The open circle has a volume fraction of α [%] 0.05, the open squares 0.1, the open triangles 0.17 and the filled circles 0.64. The image is taken with permission from [Kim et al. \(2016\)](#).

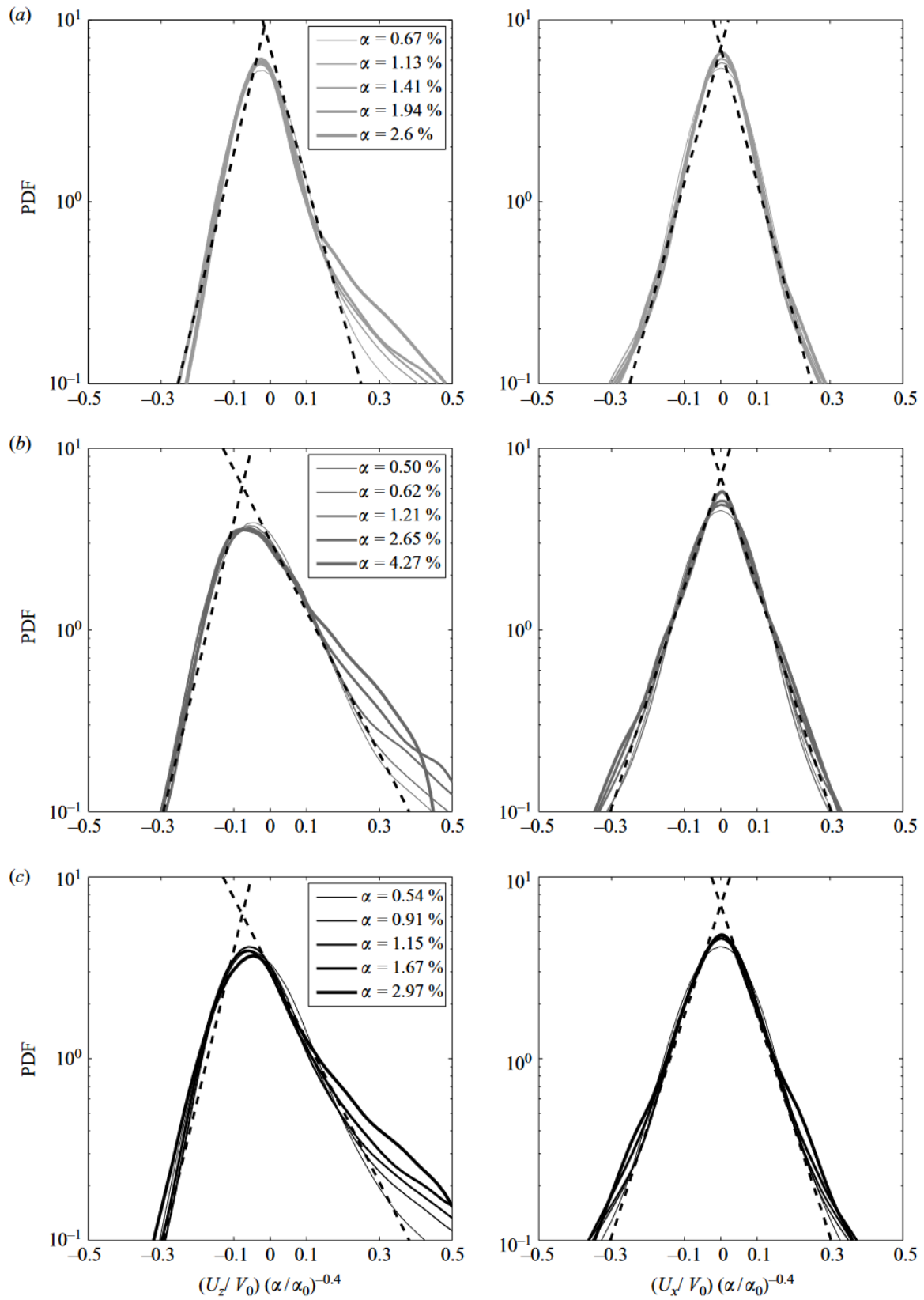


Figure 1.9: Semi-logarithmic plots of the PDFs measured and published by Riboux et al. (2009). In the left column the fluctuations in z direction (against the bubble rising direction). The right column shows it perpendicular to it. From top to bottom the distance to the bubble swarm is increased. Reprinted with permission.

direction are axisymmetric around the bubble and the distribution is homogeneous. The anisotropy, the ratio of the vertical to horizontal standard deviations is given to 1.4.

In a separate publication by [Risso \(2016\)](#) a physical interpretation of these p.d.f.s is given. The data shown in this publication are based on mathematical models and are more of theoretical nature than taken from experiments, since it is not possible to separate the governing mechanisms from each other. He correlates the fluctuation to be a result of three different mechanisms. The bubbles wake, the bubbles shape, also called the potential flow in this publication and the turbulent agitations resulting from the flow instabilities. It is explained that the wakes of the individual bubbles play only a minor, to almost no significant role in the contribution to the overall turbulence in a swarm. The wake is distributed only 3-4 bubble diameters after its creations, but not due to the inert dissipation but rather a dissipation due to the interaction with other bubbles or their wake. This means for the p.d.f. that for a large bubble density (up to 80%) the shape tends towards a Gaussian function. It is said that this is just a theoretical calculation since this case is not possible to be observed in a real experiment. For intermediate volume fractions the p.d.f.s are strongly asymmetric (between 1% and 40%). Furthermore, the shape of the p.d.f. flattens the higher the volume fraction is and with increasing wake width w . The increase in the wake length L is said to have little to no effect, however it is dependent on the total volume the wake occupies and the author suggest that the shape of the p.d.f. is proportional to $\alpha L w^2$. It is summarized that p.d.f.s are a summation of randomly distributed wakes and is responsible for the exponential tail in the upward fluctuations, while the horizontal and downward fluctuations are insignificant. The shape of the bubbles for the flow regimes considered can be approximated to be oblate ellipsoids. The potential flow is solely dependent on the axis ratio of the minor and major axis. As for the wakes the gaussian shape is only reached for unreasonable high-volume fractions of 100%. For physically feasible volume fractions an exponential tail develops that is however not as strongly dependent on the volume fraction. The third mechanism the turbulent agitations from the flow instabilities are a result of large enough Reynolds numbers inside the flow, so that the flow becomes unstable and turbulence fluctuations develop. It turns out that they are not localized and are homogeneously distributed over the liquid phase. They also appear to be isotropic and the p.d.f.s of the horizontal and vertical fluctuations are symmetric and show both an exponential tail. The nonlinear interactions between the wakes also suggest that the scaling for the turbulent agitations is also not linear with the gas volume fraction and the already introduced scaling of $(\alpha/0.01)^{-0.4} v_t$ is proposed. In this formula v_t is the standard deviation of the fluctuation at 1 percent volume fraction. Furthermore the theoretical model was compared in parts to experimental data taken by the same group and published in [Amoura \(2008\)](#) and [Riboux et al. \(2013\)](#). They show a good agreement with the flow through an array of randomly fixated spheres. To summarize the findings from [Risso \(2016\)](#) the flow in the vicinity of each bubble is modeled as an sum of potential flow around the ellipsoidal body rising at a constant velocity and the exponentially decaying wake. Furthermore, it is stated that even though the contribution of the wake is rather well understood the contribution of the turbulence is not and the dynamics still need to be investigated further. In other publications the turbulence is characterized by a k^{-3} subrange in the spectral domain. This shall be explained further in the next section and also be a topic in [Cha. 3](#).

k^{-3} model in the energy spectra

In many publications the general characteristics of a bubble swarm with certain density and bubble size that the p.d.f. is non-Gaussian and seem to appear self-similar with increasing volume fraction and a k^{-3} behavior in the energy spectra. An experimental measurement done by the group in Toulouse of this behavior is shown in [Fig. 1.10](#). Where k is the wave number. This was first reported by [Lance & Bataille \(1991\)](#). For this behavior to develop it is important that the bubble induced agitation outweighs the shear induced turbulence (at walls for example) and a large-scale recirculation due to gas volume gradients. [Risso \(2011\)](#) and [Riboux et al. \(2009\)](#) make it clear that the k^{-3} is always present when the agitations result from the bubbles wake and their interaction and take place in a range between $2\pi/\Lambda$ and $2\pi/\Lambda_c$ with Λ being the integral length scale of the spectrum and Λ_c a cut-off wavelength that is dependent on the Reynolds number and the density of the swarm. [Risso et al.](#)

(2008b) found that $\Lambda = d_b/C_d$. Where d_b is the bubble diameter and C_d the drag coefficient of a single rising bubble. It is described in Risso (2011) that the mechanism for the k^{-3} can be appointed to a superposition of the random burst of the wakes that are created by individual bubbles in a swarm. Since the spectra could not be measured in this thesis only a short explanation will be given. For a full analysis of the shape of the spectra and the dependency of the shape to the bubble size, volume fraction and other factors like the turbulent length scales refer to Risso (2011), Lance & Bataille (1991), Riboux et al. (2009) and Riboux et al. (2013) among others.

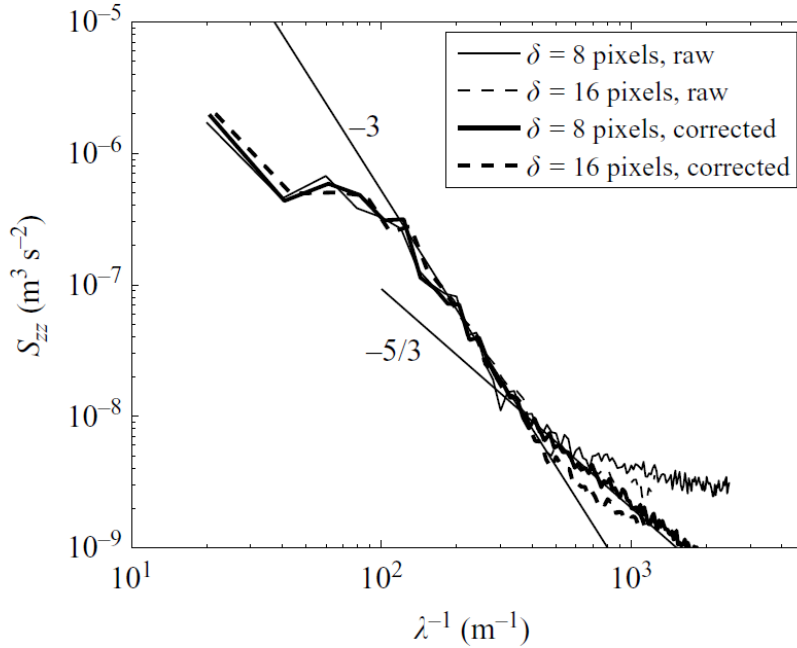


Figure 1.10: Spectra of vertical fluctuations calculated from PIV images. The different lines show different PIV interrogation windows and outlier detections. The bubble diameter was 2.5 mm and the density 0.46 %. The image was taken from Riboux et al. (2009) with permission.

1.3 Interaction between the bubble and the surrounding liquid

While the dynamics of a single bubble in quiescent water is well documented and investigated and also the bubble swarm turbulence in general has been investigated by numerous people, the understanding of the behavior of a single bubble in such a swarm is not. Especially the interaction between the swarm and said single bubble, how the turbulence is influencing e.g. the shape oscillations or the bubbles path.

One hindering aspect to that is for once the measurement technique. In the literature mostly intrusive methods are used to measure the swarm statistics or approximation by only measuring flows in a 2D channel. But those interact with the bubble and their dynamics and introduce unwanted disturbances or are approximations. If optical methods are used one big factor is the obscuration of the swarm, that results in that the usable data is either sparse or in order to create statistical values a great amount of data needs to be recorded and evaluated. This then leads to a high amount of either computational resources to first store the data and then evaluate it. Because only when a bubble by accident is in the line of sight it can be measured accurately with the current methods. Mostly 2D based approaches are reported to investigate the shape of the bubble which is a good approach for smaller bubble that are form stable but for bigger bubbles that are either oblate ellipsoids or even

show a random surface the shape cannot be evaluated correctly anymore. Making a full 3D reconstruction necessary. On top of that it is not possible to get a full reconstruction of the flow around a bubble due to the same reasons. The swarm is hindering the view and making it impossible to get information about the flow with for example PIV methods. Since PIV illuminates small tracer particles in the flow to calculate the velocity a free path needs to be assured otherwise the data is either sparse or faulty. On top the bubbles also function, since they are optically lighter than water as mirror and reflect and disperse the laser which can either damage the equipment or just create unusable recordings.

This thesis wants to close this gap between the two aspects and introduce methods and data to simultaneously measure the bubble motion, shape and flow around the bubble. With a newly created channel a physical model swarm similar to existing publications is used to emulate the swarm statistics and with a new 3D measurement technique the shape and path of the bubble are measured. This data gives an insight in the correlation between the bubble shape and the surrounding flow. In the following the channel itself is presented, then the model to create the swarm and the 3D reconstruction. In the last two chapters comparison of freely rising bubbles and bubbles in the model swarm are presented and discussed.

2 Experimental Facility

2.1 Introduction

To emulate the turbulence generated by a bubble swarm and measure the size, shape and motion of a single bubble in this swarm-like turbulence a new facility was designed, constructed and built up as well as qualified. All the experiments conducted in this work were performed in the newly build vertical counter-flow channel at the Universität der Bundeswehr München. In this section the facility itself is described and every component explained as well as the steps and results towards the optimization. The general idea of this facility is to hold a bubble in the area of a desired turbulence background level. This is achieved by creating a counter flow in which the bubbles rise. By setting the velocity to the terminal rise velocity of the bubble it can either be slowed down, stopped or pushed downwards. Additionally, certain criteria have to be met for the planned experiments performed in this channel. The channel needs to be inert, so that it can be used with chemicals like acids. This will also ensure that the channel does not rust with time. Furthermore, optical access to the measurement section is needed from all sides. Finally, it needs to be possible to inject bubbles with different diameters and volume ratio.

In the following section the different parts of the channel are described to fulfill these necessities. For a full characterization the flow, the turbulent fluctuations in the empty channel and the boundary layers are described as well. Parts of this chapter and some figures are published with permission in [Schlüter et al. \(2021\)](#).

2.2 Description of the counter-flow Channel

Water channel

The channel is sketched in [Fig. 2.1](#). It has a height of four meter and is built completely out of stainless steel to avoid corrosion and to allow the usage of chemicals. The fluid falls from the basin (450x450 mm² and 500 mm high) at the top of the channel trough the nozzle into the test section. The nozzle is designed to amplify the intensity of the generated turbulence as well as to increase the turbulent length scales. Due to the contraction of the nozzle the generated eddy is elongated while the strength and rotation is preserved.

The 80 × 80 mm² and 1000 mm long measurement section is optical accessible through borosilicate glass (SCHOTT Technical Glass Solutions GmbH) from all four sides. On one side three 150 × 80 mm² plastic windows are mounted that allow to insert for example a calibration target, chemicals or bubble generators. At the end an electrical valve is installed to regulate the flow in the channel. After passing through the channel the fluid is collected and pumped up by a rotary pump (GRUNDFOS - CME25) into the basin. To ensure a minimal error induced by the channel itself, it is important to generate the flow with minimal and homogeneous initial fluctuations or turbulence, there for a specially designed rain shower like distributor was manufactured as an inlet. The outer dimensions were made to fit the upper basin with a square area of 421.3 mm². The rain shower is connected with 4 individual tubes to the pump that fills up the inner volume of the rain shower. Over the whole area a total amount of 7620 1 mm holes are distributed, that then distribute the water evenly into the channel. The whole inlet is suspended roughly 500 mm above the water level to prevent pressure fluctuations in the channel as well as any residual higher velocity free streams. The electronics are regulated by a in house LabView Program (National Instruments) and a NI-USB6002/PCIe-6321 (USB I/O device and I/O card from

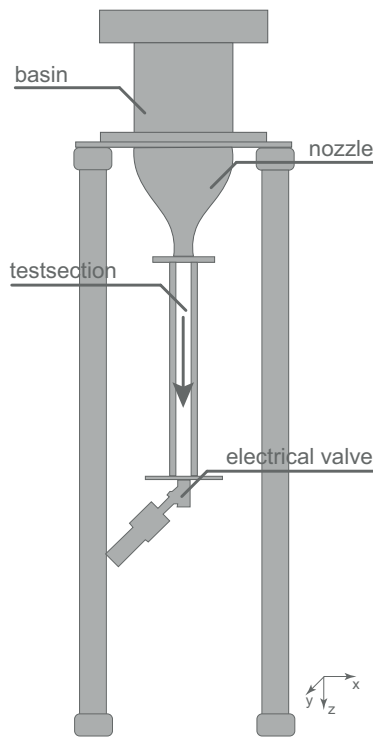


Figure 2.1: Left: Schematic drawing of the channel. Published in [Schlüter et al. \(2021\)](#) and reprinted with permission. Right: Photograph

National Instruments). With the program a target velocity is set, that can be regulated freely. Due to the internal calibration of the regulation valve at the bottom, the trigger signal is not linear to the actual opening position. The program is designed in that way, that the best accordance is met at the bubble rise velocity, in the range between $210\text{-}270\text{ mm s}^{-1}$. Since the material statistics of water are highly dependent on the temperature a sensor is mounted on the bottom of the channel to monitor and note the temperature during a measurement. It is common that the temperature is rising by roughly 5-10 degree during one measurement session when the water is not preheated. The water initially when it is filled from the tap to the channel has a temperature of 16 - 18 degree Celsius, during the measurement this rises up to 23-25 degree Celsius. To get a controlled constant temperature, water in the channel was circulated by the pump prior to measurements to have constant 22-25 degrees during the measurement.

Turbulence generators

As described in [Cha. 1](#) artificial turbulence is generated to simulate bubble swarms and their induced agitations. The different approaches and designs are outlined here. Example pictures of the individual grids are shown in [Fig. 2.2](#). A characterization of those grids and evaluation can be found in chapter [Cha. 3](#). The comparison to real bubble agitations was made with literature data as it was presented in the previous chapter. Different characteristics like the velocity, the turbulence and the turbulent statistics are shown in [Cha. 1](#) and [Cha. 3](#).

1. fractal grids (2D and 3D)

Since the turbulence in real bubbly flow consist of a wide variety of different sized vortices the idea is to



Figure 2.2: Comparison of the three different particle grids. From left to right the fractal grid, the free moving particle grid and the active grid.

use fractal grids with consecutively smaller elements (e.g. squares or I-figures). Another feature of fractal grids is, that they are known to create higher turbulence levels to regular grids with a normally repeated pattern ([Hurst 2007](#)).

2. flexible particle grids (designed and manufactured by U. Kück, University Bremen)

In the literature ([Risso et al. 2008a](#), [Riboux et al. 2013](#)) small spheres in the size of the desired bubble, arranged in a random 3D space, are often used. These simulate a bubble swarm frozen in time. While they accurately describe the influence of the bubble shape and swarm, those grids neglect the bubble movement, which is an important factor in the turbulence generation. With these flexible particle grids the movement can also be considered. While the first two layers of particle elements are fixed in xyz-direction, the lower elements (arranged in five layers) are only attached to the one above and can move freely in the xy-plane.

3. active grid

Similar to the one used in the Twente water tunnel this grid allows to generate nearly homogeneous and isotropic turbulence. Consisting of 24 motors metallic triangles are rotated in different speeds and direction. With this and a special rotation program homogeneous and isotropic turbulence can be created with different length scales and intensity. This grid is used by the group in Twente and used to generate a wide variety of turbulence without the need to change the grid. Due to the measures of the channel it was not possible to install this grid in the Water Channel at the University der Bundeswehr in München. It is however planned to do this in the future.

Bubble generation

To inject gas bubbles in the continuous phase different methods are applied to fit the need of the particular experiment. An overview of the devices used is given here and will be named in the according section which one is used for the experiment. For all experiments blunt needles are used to insert the bubbles into the measurement section. Three small capillary needles are attached to a plate that can be mounted in the calibration windows of the channel. With this, bubbles can be generated at several heights in the channel. The capillary is blunt with

the surface perpendicular to the flow in the channel, to ensure the detachment is uninfluenced by the cut of the surface.

For the measurements two different systems were used. One for the injection in the quiescent water, the other for injection in the counterflow. Due to the counterflow a static pressure generates above the blunt capillary that prevents the bubble from injecting in the channel. This pressure needs to be overcome first before the bubble can be released in the channel.

- quiescent water

To generate single bubbles a fast opening valve from Festo (MHE2-MS1H-3/2G-QS-4-K) can be regulated by a LabView in house program and synchronized to, for example the cameras. So, bubbles in a wide range of size, from 1 mm up to 10 mm can be inserted in an almost freely selectable volume fraction. The size is here mainly determined by the inner diameter of the needle. Bubbles created with this approach are consisting of pressurized and filtered air from the house connection. The air here is under a pressure of initially 5 bar and gets reduced to 0.5 bar before entering the magnetic valve.

For a later measurement with a corrosive NO gas (nitric oxide-bubbles) the magnetic valves were replaced with gas tight syringes and a syringe pump. Even though, the syringe pump has the disadvantage that the compressibility of the gas complicates the injection of a single bubble it is safer and also does not damage the equipment. With a inhouse LabVIEW program the syringe pump was controlled and set to inject a fixed volume. This however was very error prone and the bubbles could only be irregularly injected with the desired volume. Especially the constant static pressure of the counterflow hindered the consistent injection.

- with counterflow

While not only the static pressure was challenging to overcome a second problem was that the bubble is influenced by the turbulence as soon as it detaches from the needle. This leads to the bubble most of the time not to be in the measurement volume, since the probability that the bubble gets transported into the boundary layer and out of the measurement section increases with the distance to the measurement volume. To prevent this and inject the bubble close to the measurement volume a needle system was built into the channel that transports the bubble inside a long capillary close to the measurement volume and ends then again in the same blunt needle. Another option was to regulate the flow in the channel to slowly ramp up the counterflow as the bubble is rising in the channel. This however showed artefacts in the measurement and falsified the data, since the acceleration of the liquid could sometimes still be seen in the data. This led to the decision to work with the inner tubing system.

The outer mechanism with the magnetic valve or the syringe pump needed to be slightly adjusted to overcome the static pressure, but by increasing the outer pressure from 0.5 bars to 1 bar and adjusted open and closure time of the valve single bubbles could also be created in a counterflow with a good reproducibility of the size. The bubble size was determined with a shadow image approach and the error in the radius of 50 bubbles was estimated to less than 2%.

- other methodes (not used)

This method is only mentioned here to complete the list of the used bubble generation methods.

One idea to overcome the problem of the compressible gas in the syringe pump was to use an approach similar to droplet microchannels. A T-shaped channel with the inner dimensions of $2 \times 2 \text{ mm}^2$ was carved into an acrylic plastic and glued to a glass slide. By connecting one side of the T to a syringe with the desired gas and the other to a liquid, that is also present in the channel, the idea was to create pockets of the desired gas inside the microchannel and then use the water to push the gas in the measurement section. This approach was however discontinued, since the method of adjusting the syringes to each other and to

create a suitable water flow was not reliable enough and neither single bubbles nor a reproducible bubble size could be created.

Another idea, that was designed for the usage with the NO Gas was a container with a membrane inside. Inside the membrane the gas would be stored and by regulating the outer pressure the gas could be injected into the channel. As mentioned before a certain outer pressure is necessary to overcome the static pressure and inject the bubbles into the channel. With the pressurised air from the house outlet, that could be freely varied up to 5 bar, the membrane could be put under pressure and the gas would be pumped with the same pressure into the channel. But the NO gas could not be stored or filled into the membrane container at the faculty due to safety reasons. The Bundeswehr University does not possess the facilities to safely and correctly handle this gas and so the gas needed to be transported from the LMU in Munich. This method was also discontinued due to safety reasons during the transport. Finally, the NO gas was transported to the University in a small not pressurized glass container from which the gas could be extracted with the gas tight syringe.

2.3 Characterization of the Counter-flow Channel

In order to generate turbulence that is similar to swarm turbulence, the turbulence generated by the channel itself needs to be known. Several different inlets were tested and optimized to grant a homogeneous and low turbulent inflow. As described earlier the best inflow conditions were achieved with a rain shower like distributor mounted a five centimeters above the water surface. The following chart Fig. 2.3 shows the mean velocity and the turbulence distribution in the free stream part of the measurement section. On the other hand, Fig. 2.4 shows the velocity and the turbulence profile in the boundary layer.

Both characterizations were performed with a planar PIV-System. While the free stream characterization was performed with a single camera, the boundary layer was measured with a stereoscopic system, to determine the influence of the wall. For both systems 1000 images were recorded and the average calculated. Convergence studies showed that 1000 images are sufficient for calculate the mean value. The PIV measurements are performed with sCMOS (pco.edge 5.5) cameras from LaVision in combination with a Nd:YAG - Laser (Innolas Spotlight 4000, $\lambda = 532 \text{ nm}$) and the measurements are evaluated using the commercial software DaVis (LaVision). The light sheet is placed perpendicular to the channel walls in the middle of the channel with an estimated thickness of 0.5 mm. The measurement is performed with a double pulse ($\Delta t = 700 \mu\text{s} - 2000 \mu\text{s}$) and a repetition rate of 10 Hz. An interrogation window of $16 \times 16 \text{ px}$ is achieved after an iterative multi-grid evaluation with interrogation window refinement. In the following, the coordinate system is defined as \vec{z} in flow direction, \vec{x} and \vec{y} normal to that, where \vec{x} is horizontal in the field of view. This was chosen to have an easier comparison with several publications. Systematic errors, resulting from the calibration or light sheet alignment are smaller than the uncertainty of the measurements, since special care is drawn to aligning both the target and light sheet with an error of less than 1° . Random uncertainties are affected by many parameters including particle image size, particle image density, turbulent fluctuations and interrogation window size (Kähler et al. 2012). With a mean pixel displacement between 10-12 pixels in the particle images and a particle images sizes of 3-4 pixels as well as a particle per image ratio of 0.1 the random uncertainties can be estimated to $\sim 1 \%$. From the PIV data the homogeneity, isotropy and statistical values, like the mean velocity field $u(x, z)$ (averaged over 1000 vector fields), the corresponding fluctuations $u'(x, z, t) = u(x, z, t) - \bar{u}(x, z)$ with a good local resolution are calculated. To determine the turbulent intensity Tu [%] the root-mean-square (rms) of the fluctuations is normalized by the mean velocity at that point resulting in $Tu(x, z, t) = u(x, z, t)'_{\text{rms}} \cdot (u(x, z))^{-1} \cdot 100$.

As depicted in Fig. 2.3 the velocity profile across the channel is homogeneous over a wide part in the middle and develops a boundary layer with a thickness of $\sim 3\text{-}5 \text{ mm}$. With a width of 80 mm the full channel can not be resolved due to the beams holding the channel glass walls in place. Thus the graph does not span over the whole channel width. The thickness of a boundary layer is defined for unaffected flows from the wall perpendicular to

the point where U_{99} (99% of the free stream velocity) is reached. The boundary layer is depicted in detail in Fig. 2.4. In theory the velocity should go to 0 at the channel walls. Due to friction, there is a velocity gradient in a flow between the wall and the free flow, since the adhesion condition applies to the wall, i.e. $u_x = 0$ mm/s. However due to measurement uncertainties and the reflective surface of the glass, it is not fully possible to resolve the velocity and the turbulence close to the channel wall.

Those characterizations were performed at the intended measurement position downstream, behind the grids. Since this is shortly after the nozzle the full boundary layer is not developed yet and so it is similar in thickness for different velocities at this measurement point.

Even up to a velocity greater than 300 mm/s the inflow is constant with time and shows a flat profile with a slight increase in the middle section. The turbulent profile shows a similar behavior. For higher flow velocities the turbulence starts to show an increase in the middle of the channel due to the flow not being able to evolve in this short distance. For the interesting velocity ranges (200 - 250 mm/s) needed for these experiments however the turbulent profile is sufficiently homogeneous. The boundary layer also shows an expected behavior. One thing to note here is that the velocity close to the wall cannot be truthfully recorded or measured. It is only with some uncertainty possible to determine the position of the glass channel walls in the measurement images due to reflections on the glass by the laser. It was possible to determine the boundary layer up to a 2 mm, since it was not of interest to resolve the flow close to the channel wall, but the increase and general estimation of the boundary layer size. However, it still shows the expected size of the boundary layer of about 3-4 mm and that it is consistent for the velocities used in the following measurements.

In conclusion it can be said that the channel provides a homogeneous inflow over the measurement section. Both the flow and the turbulence show a satisfactory behavior both in channel normal as well as in channel flow direction. With that the characterization shows that the channel is suitable to carry out the measurements and provides a good basis for the following experiments. In addition, the designed bubble generators allow to reproducibly inject single bubbles in a variety of sizes into the channel both with and without the counterflow. Even the corrosive NO gas could be handled without the need for special chemical facilities or handling tools. With the magnetic valve bubbles from both gasses, air and NO could be reliably inserted into the channel. By using also an inner channel tubing system the bubbles could be transported close to the measurement volume and be generated close to the intended measurement point.

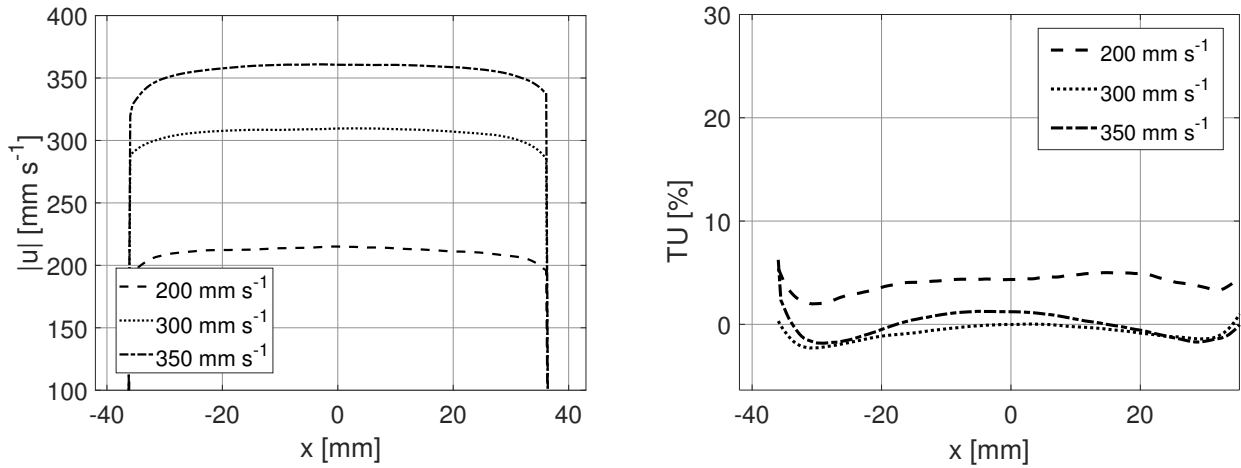


Figure 2.3: Absolute velocity profile across the channel. Left shows the mean velocity profile along the channel normal for three different inflow velocities. The right picture shows the corresponding turbulence level. The graphs don't span the full channel width due to a blockage of the beams holding the glass.

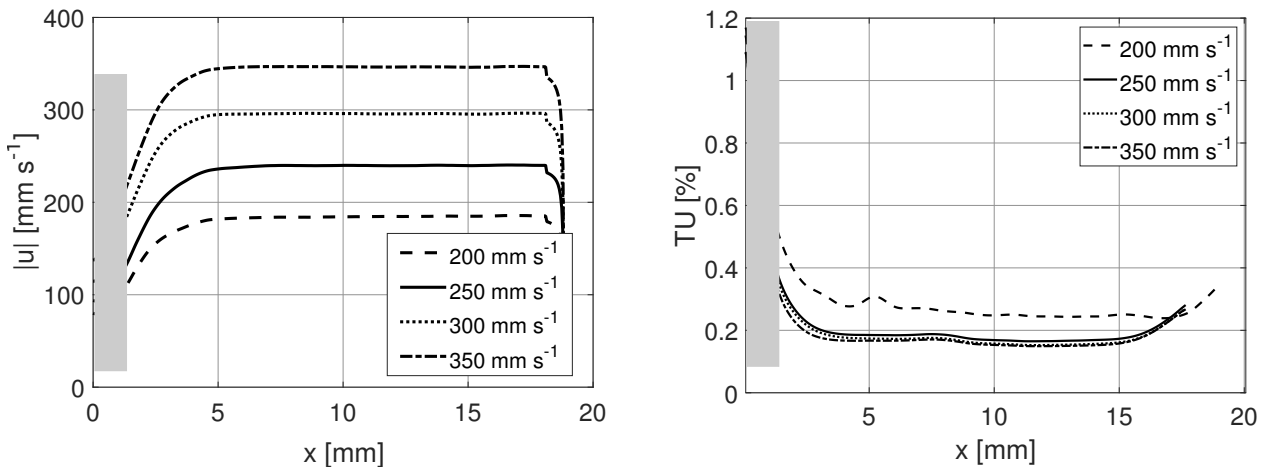


Figure 2.4: Profile characterization of the boundary layer of the channel. The left image shows again the velocity profile along the channel normal for four different velocities. In the right is the corresponding Turbulence level plotted. Published in Schlüter et al. (2021) and reprinted with permission.

3 Emulation of bubble induced turbulence

3.1 Introduction

Today in process modeling the gas bubbles can be seen and are often used as non-intrusive mixing devices due to the induced turbulence. This mixing is more moderate in comparison to mechanical steering. In many technical applications bubbles with an equivalent diameter range of $d_B \sim 1-10$ mm are found in such a homogeneous bubbly flow with up to 18 Vol.-% (Deckwer 1985). To better understand the mechanics of the mixing at high volume fraction, it is necessary to investigate the interaction between bubbles, their motion in a swarm, as well as their interaction with the induced wake turbulence. Attention must be placed on characteristic variables like the bubble size, gas volume fraction and liquid agitation to better understand their influence on aspects like the mass transport from the bubbles in the surrounding fluid.

For higher gas volume fractions, which results in increasing opacity, only intrusive methods are applicable. Due to the usage of probes strong disturbances, not only to the bubbles but also in the flow structures, are generated that affect the result. Therefore, optical measurement techniques are preferred, since they allow for a spatially resolved measurement instead of a point measurement. This gives a more detailed insight into the individual processes without disturbing the physical processes. In addition, optical measurements allow for a high spatial resolution compared to punctual measurements provided by e.g. probes. However, by using optical methods only low volume fractions $\sim 1-2$ Vol.-% can be measured due to shadowing by the outer bubbles of the swarm. In real applications however a much higher volume fraction is used. An optical measurement would be only possible if by chance a free line of sight is visible to the bubble of interest. So, the results are either erroneous or a high number of images of data would be need to be recorded and selected in which the bubbles are visible and only a few recorded images could be evaluated. Since it is impossible due to the shadowing of the swarm, especially high-density swarms to study individual bubbles the idea of this chapter is to find a model swarm that creates agitations similar to real bubble swarms and study single bubbles in this flow.

To emulate those flow conditions various publications presented different methods to create such turbulence for example arranging spheres in a random 3D array (Risso et al. 2008a, Riboux et al. 2013). However, those neglect the motion of the bubbles. The motion of the bubbles is responsible for the high turbulent degrees, as shown in (Risso 2016). Risso describes that the turbulence can be contributed to three different factors the potential flow disturbances around the bubble, the average bubble wake and the turbulent agitation resulting from flow instabilities. He explains that the wake of an individual bubble in a dense bubble swarm, so a swarm with a high-Reynolds-number is dispersed after a few bubble diameters and that the wake is not an important factor in the bubble swarm. Furthermore, Risso states that the shape of the bubbles can be approximated as oblate spheroids but those are mostly contributing to the shape of the fluctuations and not to the overall strength of the agitation. The main factor for the turbulent agitations is contributed by the flow instabilities that are mainly created by the three velocity components of the bubble's movement.

In this chapter the static 3D grids are extended and a new similar grid is introducing that also include the motion of the bubble. For comparison a similar static grid is considered as a comparison to the free moving grids. These two different methods to emulate swarm statistics are measured, characterized and compared to real bubble swarms. The following results have been published in Haase et al. (2017) and in (Schlüter et al. 2021).



Figure 3.1: Photograph of one exemplary particle grid. Only the top two layers are fixed in all spatial directions. Every following layer is solely attached vertically, allowing the particle strings to move freely in a horizontal plane. Published in (Schlüter et al. 2021) and reprinted with permission.

3.2 Free moving Particle Grids

The method utilizes plastic beads which are fixed to flexible fibers (Fig. 3.1) and allow the 'particles' to move randomly in the liquid flow. The grids have been designed and manufactured with different sizes and volume fractions. Before making measurements with bubbles however, the flow turbulence that are created by those grids need to be characterized in regards to their flow statistics and compared to real bubble swarms. If this is feasible, it will make it possible to study the behavior of single bubbles or small bubble swarms in a swarm-like turbulence by using non-intrusive optical methods. With this, a detailed investigation of single bubbles regarding their shape, movement and induced flow as well as the resulting mass transport, would contribute to the better understanding of physical phenomena in a bubble swarm of high-volume fraction. In the work presented herein, the characterization of the particle grid generated turbulence was performed with planar particle image velocimetry (PIV) as well as electro diffusion measurement technique (EDM) and compared to turbulent statistics of real two-phase flows. The EDM measurements were also performed as reference measurements in real bubble swarms. The EDM measurements were performed at the Universität in Bremen. The results of the EDM are briefly shown here and fully published here: Mießner et al. (2017), Haase et al. (2017)

3.2.1 Experimental Setup

Experiments were performed in the newly build vertical counter-flow channel at the Universität der Bundeswehr in Munich. The schematics of this channel is provided in Fig. 2.1. To characterize turbulent flow features behind the grid such as its statistics and special length scales, 2D PIV measurements were conducted. Here a sCMOS camera from PCO was used (PCO edge 5.5). To get a complete picture electromagnetic diffusion measurement were performed at the Universität Bremen to also acquire information about the temporal length scales and as reference to real bubble swarms. The same 2D planar PIV setup as used in Cha. 2 was used again for the grid

	Grid particle shape	Particle size [mm]	Particle volume fraction [Vol.-%]
1.	spheres	10	9.83
2.	spheres	10	3.97
3.	spheres	5	9.83
4.	spheres	5	3.97
5.	ellipsoids	3.91×5.65	3.97
6.	ellipsoids	8×12	9.83

Table 3.1: Overview of the grid shapes, diameters and volume fraction

characterization. The light sheet was placed close to the grids so that the last element of the grid was still visible in the recordings. This resulted in a measurement window of at least 5 particle diameters and spanned over the whole channel cross section, minus the framing. This was about 1 cm on the left and right side that was obscured. This however spans over the boundary layer, that was previously determined to be around 5 mm in the clean channel flow. The boundary layers for the grids are also measured separately with a 2D stereoscopic setup.

The EDM measurement principle is described in [Mießner et al. \(2017\)](#). The particle grid measurements are performed in a flow channel (0.1 m in diameter and 2.5 m in height) according to [Heithoff et al. \(2017\)](#). The EDM only resolves data at a single point (no spatial resolution), but with complete temporal resolution. The EDM provides localized velocity data which is used to calculate frequency-dependent spectral energy density. By combining the results of both measurement techniques, temporally and spatially resolved data can be obtained. The developers of the electro diffusion measurement technique (EDM) ([Pauli 1992](#)) report a performance comparison to the hot-film anemometry (HFA). [Mizushima \(1971\)](#) calculated a critical detection frequency of 6.5 kHz for EDM wires of 10 μm thickness at a Schmidt-number of $Sc = 2431$. Assuming the analogy of heat and mass transfer, the heat boundary layer is characterized by the Prandtl number Pr . For comparable set-up parameters the critical detectable frequency of the HFA is reported to be 45.9 kHz at $Pr = 7$. In accordance with [Fortuna & Hanratty \(1971\)](#) the critical detection frequency is for the HFA seven times higher compared to the EDM. Later [Pannek et al. \(1994\)](#) investigated the influence of defined disturbances on the EDM signal. Within the observed frequency range up to 200 Hz, no influences of superimposed signal fluctuation on the measurement accuracy are found. The convective transport towards an EDM probe with a thickness of about 0.7 mm and three active surfaces in combination with the characteristic bubble rising velocity of $u_b = 28 \text{ cm s}^{-1}$ delivers a volume exchange rate at the detector surface in the range of 1 kHz. The according hydrodynamic boundary layer for flows around cylinders delivers a thickness of about 12 μm on the approaching flow side.

In [Tab. 3.1](#) the specifications of the measured grids are listed. The grids have different particle shapes e.g. spheres or ellipses in two sizes $d_b = 5 \text{ mm}$ and 10 mm as well as particle volume fractions α ranging from 3.97 Vol.-% to 9.83 Vol.-%. Each grid consists of at least five layers of beads with different spacing according to the desired volume fraction (ranging between 5 and 10 mm). While the first two layers are fixed, the following individual particles are only tethered to the one above to secure the vertical distance. All elements in the bottom layers can move randomly in x and y plane. The setup can be seen as a swarm of bubbles held in place above the measurement plane, so that the wake and induced liquid fluctuations behind this three-dimensional grid can be measured. As mentioned in the beginning of the chapter, next to the free moving particle grids a rigid grid with the threefold length (~ 15 layers) is characterized as well. This will give insight in the contribution of the particle motion to the turbulence, since the bubble-induced turbulence is a collective effect induced by the bubbles wake and the motion of the bubbles.

3.2.2 Characterization of the particle grids and turbulence analysis

As described in Riboux et al. (2009) a good model to generate swarm-like turbulence is achieved by using small spheres with the size of the desired bubble, arranged in a random pattern at fixed places in space. This model, however, neglects one aspect, the random bubble movement. Since the turbulence created in bubbly flows results from a combination of the bubble motion, wake and the agitated liquid phase, it is important to take all these factors into account for emulating bubbly flow. With the proposed model of the free moving particle grids, these factors are included and can be modified freely. For this assessment, the mean velocity in the main and perpendicular flow direction are evaluated followed by the analysis of the fluctuations, turbulence levels, and energy spectra. To verify the validity of the particle-induced turbulence a comparison to the real bubbly flow of each characteristic will be given after each paragraph.

Velocity Profile

It is well known that in a bubbly flow with low gas volume fractions α a velocity profile like a laminar one is present, but with increasing volume fraction α a change from the laminar flow profile can be observed. The bubble rise velocity is nearly constant over the cross section of a channel with a slight decrease in the near wall region due to the boundary layers at the channel walls (Kim et al. 2012). In bubbly flows the liquid velocity is strongly altered by the void fraction of the swarm. At low to moderate volume fractions the bubbles are distributed statistically which results in a velocity profile resembling a turbulent flow (Liu & Bankoff 1993, Risso & Ellingsen 2002). With increasing α the shape deviates from the flat profile and the mean velocity lowers at the core and rises near the wall (Kim et al. 2016).

In Fig. 3.2 (left) the velocity components in span wise direction \vec{x} and flow direction \vec{z} behind the grids, three particle diameters d_p behind the last layer of grid elements respectively the velocity underneath a particle element is plotted against the distance normalized with the particle diameter d_p . For better evaluation velocities are normalized by the bulk velocity $u(x, z)^{-1}$. The field of view was placed to have the last row of particles in the top of the picture. The mean velocity behind the grid takes roughly four particle diameters to be homogeneous since the wake of each individual particle is still present in the vicinity behind the particle grid but subsides within the range of ≈ 4 particle diameters and a homogenous velocity distribution is present on average. The horizontal velocity $u_x(x, z)$ is small in comparison to $u_z(x, z)$. In Fig. 3.2 (right) the decay of the flow behind the grids is compared between each other and to real bubbly flows. Further, the wake interactions are described as responsible for a faster dissipation (Risso et al. 2008a). Three regions are defined in Risso (2016):

1. a strong decay near the bubble where the flow is similar to that behind a single bubble
2. a region where only the wakes interaction is significant and decays much faster and
3. a region where the velocity fluctuations reach an asymptotic state.

It is noted that the velocity agitation settles after roughly five bubble diameters and decays exponentially behind a small bubble swarm. For all the particle grids a constant exponential decay is observed, which declines in a similar fashion as described in Risso (2016) with the best agreement present for the velocity $u_z(x, z)$ behind the elliptical 5 mm and 4 Vol.-% grid. While the velocity behind the grids with bigger elements is enhanced more than the smaller ones, the decay is also faster ($\sim \exp(-1.1)$ for the big elements and $\sim \exp(-0.46)$ for small grid elements). In comparison, the rigid grid shows a much thinner wake region and it takes roughly 6-7 sphere diameters until the profile becomes homogeneous. With increasing velocity, the oscillation frequency around the initial position enhances and the entrainment intensifies but the wake is a result of the amplitude of this oscillation, which implies that it takes roughly the same distance for all velocities to decay back to the same level. Due to the particles moving in a random pattern the free stream between two grid elements can flow freely until it gets entrained and enhanced. Because of the random movement of the grid elements the free

stream gets continuously altered in its velocity, which creates different shear stresses on the particles and thus generates different turbulent length scales. So, the movement of the particle enhances the development of the homogeneity of the flow profile but also the intensity of the turbulent fluctuations, which is again similar to real bubbly flows, making it again clear that the movement in the swarm is the most important factor in creating the swarm turbulence.

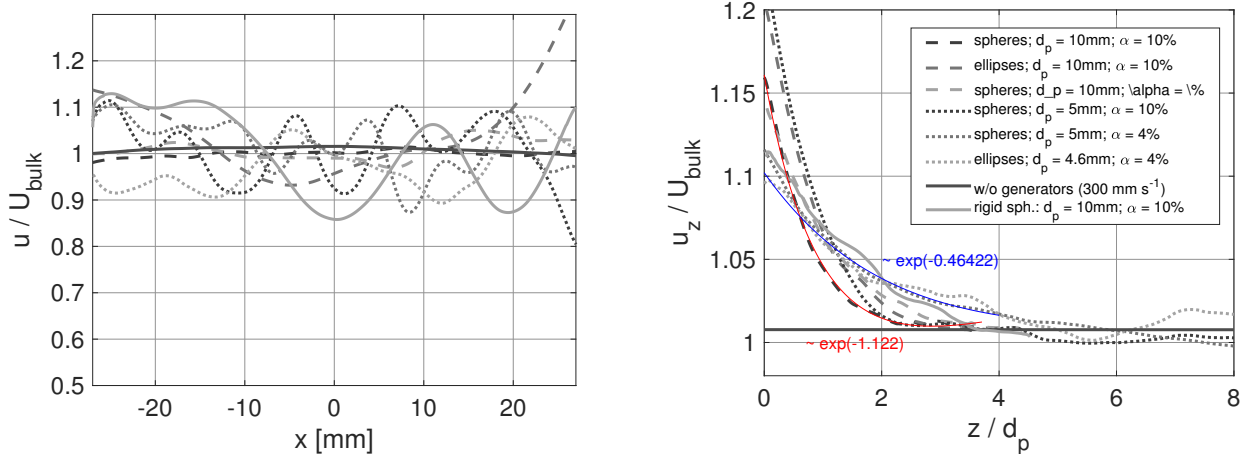


Figure 3.2: A comparison of the flow velocities behind the free moving particle grids. Left image: Comparison of the velocity profile in spanwise direction at $\sim 3 d_p$ behind the last layer of grid elements. Right image: Vertical velocity component (u_z) in flow direction under a grid element against the distance in particle diameters of the grid. The flow behind grids with big elements decays proportional to $\exp(-1.12)$, while the flow behind smaller elements decays slower, proportional to $\exp(-0.46)$. Published in [Schlüter et al. \(2021\)](#) and reprinted with permission.

Turbulence and Isotropy

In [Fig. 3.3](#) the turbulence level Tu is plotted, where the left image shows the profile normal to the channel direction \vec{z} as a comparison for the different grids and the right the decay in flow direction \vec{z} . Again, the influence of the individual spheres is measurable but with increasing distance from the grid the profile becomes flatter and the influence of each individual row tails off until it becomes similar in shape to the undisturbed channel flow but with increased magnitude about 10%. Due to the vortex shedding around the moving spheres the turbulence is enhanced underneath a row of obstacles, which is the same behavior for real two-phase flows. In the core regions, where the bubbles are concentrated, the induced turbulence becomes larger. [Fig. 3.3](#) compares the turbulence decay and stress that are introduced by the grids. The lateral motion of the spheres has an influence on the turbulence level, so grids with a high-volume fraction induce a greater turbulence, as well as bigger spheres due to their greater blockage effect in downstream direction. Both fluctuations in flow direction and span wise direction are in the same order, considered for all sphere distances. Due to the random particle movement, different turbulent length scales can be generated. The free stream between two grid element strings gets entrained and continuously altered which results in different shear stress on the particles and generates different turbulent length scales. Again, do the grids with 10 mm particle diameter introduce a higher agitation after the last layer of spheres, which decays rapidly in comparison to the small spheres. Both again decay exponentially. After two sphere diameters for the small and big spheres, the turbulence decreases in the same way. The flow velocity influences the magnitude of the enhancement while the volume fraction and size determine the shape

and decay. Taken from [Lance & Bataille \(1991\)](#) the turbulence level for swarms with 2% is $\sim 6\%$, which would, by extrapolating lead to a turbulence of 30% for swarms with 10% volume fraction. In [Liu & Bankoff \(1993\)](#) and [Wang et al. \(1987\)](#) the turbulence is described with the fluctuations $u'(x, z, t)_{\text{rms}}$ and $\sqrt{\langle u'^2 \rangle} / u$. The fluctuations in vertical and horizontal directions for real bubble flows are comparable to each other due to the oscillating path of bubbles, even though the main flow direction is vertical ([Liu & Bankoff 1993](#)). Again, using the grids shows, that the bubble motion has a significant influence on the turbulence level as well. As shown in [Fig. 3.3](#) the overall turbulent intensity is lower by 5-10% under the rigid grid element and it takes almost double the length downstream until the inhomogeneity decays and a homogeneous flow profile is present.

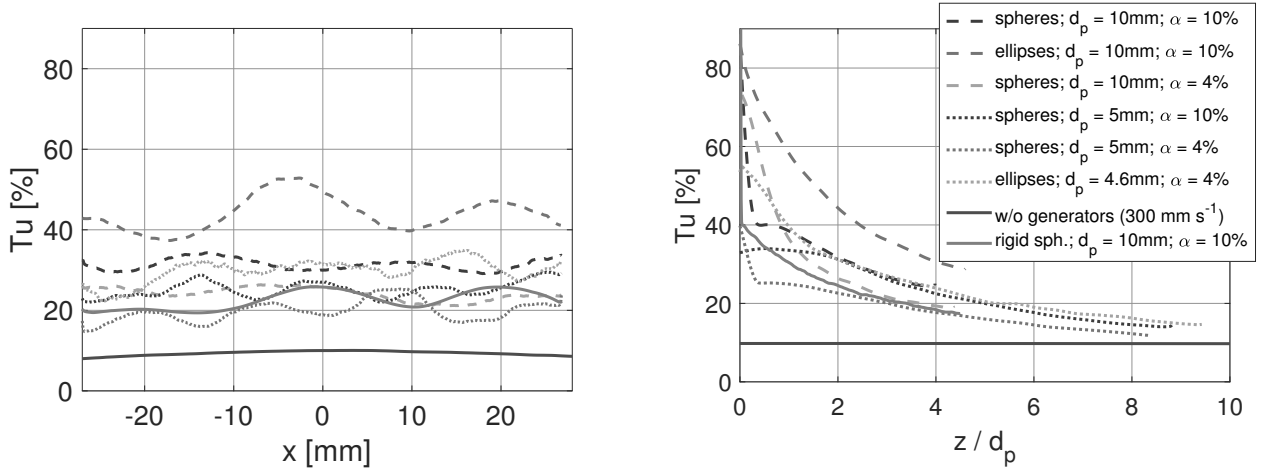


Figure 3.3: Comparison of the introduced turbulence by the different grids. Left image: Comparison of the turbulence profile in spanwise direction at $\sim 3d_p$ behind the last layer of grid elements. Right image: Vertical decay of the turbulence Tu under a grid element against the distance in particle diameters of the grid. Published in [Schlüter et al. \(2021\)](#) and reprinted with permission.

Influence on the turbulent boundary layer

Additionally, it is of interest how the induced turbulence of the different grids is affecting the boundary layer. For that similar experiments were conducted. However, to get a better resolution near the channel walls a stereoscopic setup was installed. Three particle grids as well as the empty channel, as a comparison were measured at different velocity. The inflow velocity is set to $u_\infty = 200$ mm/s and the resulting velocity u as well as the turbulence degree averaged over the measuring range are considered. [Cha. 2](#) shows results for the empty channel in [Fig. 2.4](#). The turbulence on the wall goes towards 100% and falls within the boundary layer to a value of $Tu \leq 30\%$. Due to the restrictions of the measurement technique and the fact that the wall position can only be determined with a great uncertainty, the measurements close to the wall (< 1 mm) are unreliable. In [Fig. 3.4](#) a comparison for the different grids is shown.

The characteristics of the boundary layer for the grid with small spheres (5 mm), a high volume fraction ($\alpha = 9.87\%$) and the grid with ellipsoidal elements ($\alpha = 3.8\%$) are similar, since in both cases the elements with a reference diameter of $d_p = 5$ mm induce turbulence. However, the volume fraction α specifies the elements distance to the wall. A higher packing density means that more spheres are hanging close to the wall and the influence on the boundary layer increases. This has hardly any influence on the boundary layer, but only becomes apparent at a greater distance from the wall, at which a boundary layer is fully developed. With both grids a velocity peak occurs, which indicates an interaction between the induced wakes of the spheres with the boundary

layer. For both grids the velocity peak is at an equal distance from the wall. The grids with a higher density show a more pronounced peak, which gets even more obvious for higher velocities. For grids the velocity peak is located at an equal distance d_x from the wall, where for the empty channel the boundary layer is separated from the undisturbed inflow.

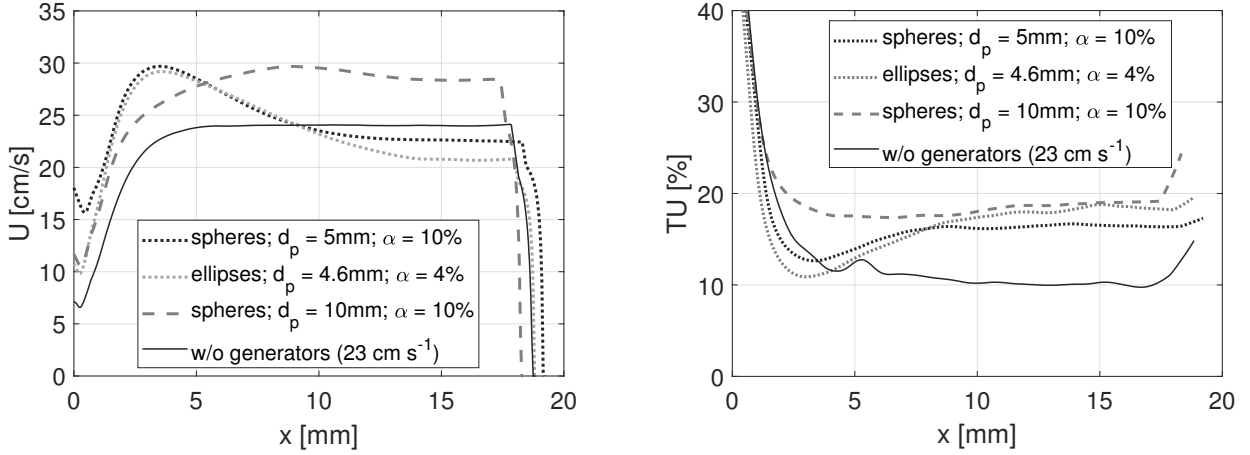


Figure 3.4: Comparison of the velocity and turbulence in the boundary layer profile behind different particle grids. The falloff in the left image results from the end of the measured image and is an artifact from the PIV evaluation. This is not physical and solely an error in the measurement.

For further investigation, the distance d_z from the turbulence grids at which the boundary layers are to be evaluated is taken into account. Fig. 3.5 and Fig. 3.6 show the velocity field and the turbulence level behind the turbulence grid with elliptical elements. The measuring range is divided into four equally sized sections d_1 to d_4 , which extend from below the turbulence grid to $d_z = 4d_p$ and in which the turbulence is averaged. The fact that the graph does not reach zero is because that the particle movement cannot be resolved directly at the wall. Also, the finite evaluation-window-size and the reflection of the particles at the wall falsify the averaging. The thickness of the boundary layer cannot be described with the conventional definition, since the flow is on the one hand influenced by the turbulence grids and are not fully developed. There is a local interaction between the small induced vortices of the spheres and the turbulence in the boundary layer. In order to be able to make exact statements about the boundary layer, one would have to separate the different turbulence, nevertheless the increase in velocity up to 20 mm/s provides a clear indication of the vortex interaction. The set velocity of $u_0 = 200$ mm/s should deviate by a maximum of ± 10 mm/s from the actual flow velocity in the channel.

The turbulence level within the boundary layer decrease to a value of $TU = 25\%$. In the flow further away from the wall, the turbulence increases again, but the greater the distance d_z from the turbulence grid, the smaller the increase. The reason for this behavior of velocity and turbulence level is the wake induced by the vortices of the grid elements.

Subsequently, the characteristics of the boundary layer are examined at different velocities. The result of the ellipsoidal grid with the quantities averaged over the entire measuring plane is used as an example. With increasing inflow velocity u_∞ , the average velocity also increases, as can be seen from Fig. 3.6 the already mentioned a velocity peak due to induced turbulence is more pronounced with increasing u_∞ with respect to the mean flow velocity. As a result, the interaction area between the boundary layer and the induced vortex is constantly at the desired measurement distance of $d = 3d_p$. The subsequent drop in velocity occurs with increasing u_∞ ($u_5 = 320$ mm/s) to values that are clearly above the set value in the section under consideration. As can be seen in Fig. 3.6, the degree of turbulence decreases slightly with increasing speed. This may also

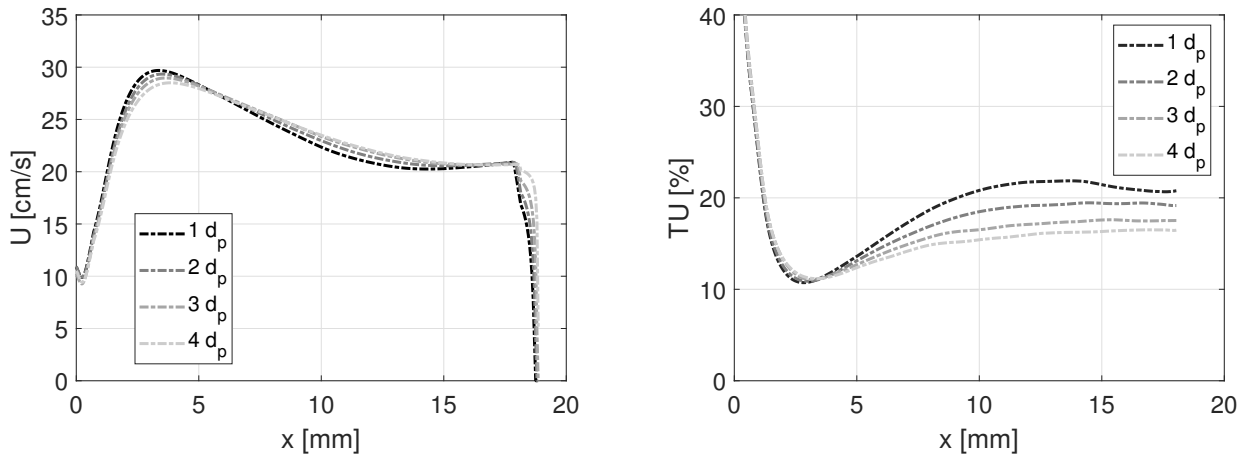


Figure 3.5: Comparison of the velocity and turbulence in the boundary layer profile in increasing distances behind the elliptical particle grid. Close to $x = 0.5$ in the Minimum of the graph the wall was positioned. Theoretically the velocity should go to 0, but due to the finite PIV evaluation windows the wall cannot fully be resolved. The small increase on the left side of the minimum is the mirror image of the particle in the glass channel walls. The same would be visible in the image for the turbulence but the values here are cut off by the graph. The fall off on the right side can also be explained by the finite measurement windows at the edge of the recording.

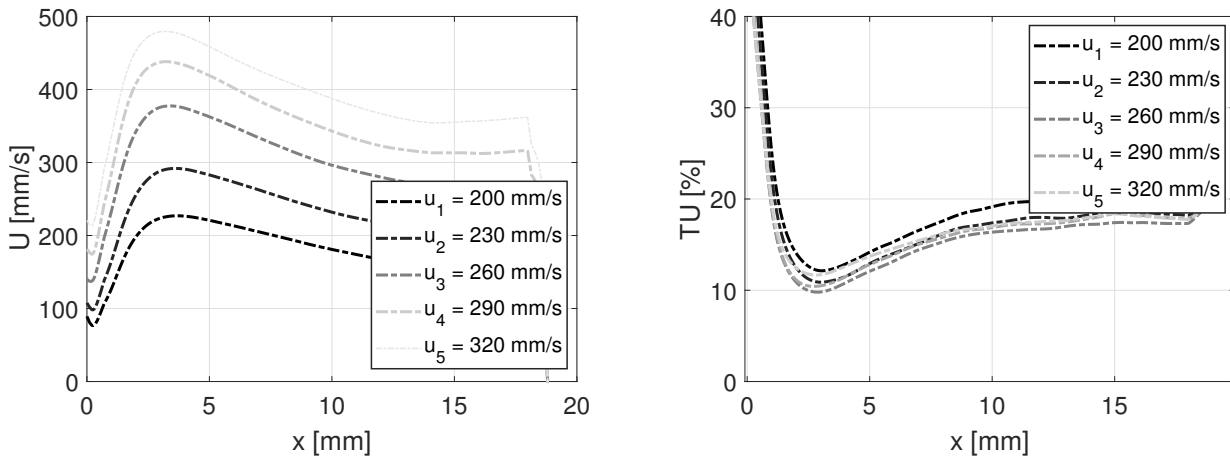


Figure 3.6: Comparison of the velocity and turbulence profile in the boundary layer for different bulk velocities with the elliptical grid mounted. and turbulence in the boundary layer profile in increasing distances behind the elliptical particle grid. Close to $x = 0.5$ in the Minimum of the graph the wall was positioned. Theoretically the velocity should go to 0, but due to the finite PIV evaluation windows the wall cannot fully be resolved. The small increase on the left side of the minimum is the mirror image of the particle in the glass channel walls. The same would be visible in the image for the turbulence but the values here are cut off by the graph. The fall off on the right side can also be explained by the finite measurement windows at the edge of the recording.

be due to the measurement error caused by the wall, like the reflection in the glass. In the boundary layer, the course of the turbulence degree is similar, only the initial values at the wall deviate from each other, which can be attributed to a measurement inaccuracy. Therefore, the increase of the external velocity in the investigated velocity range has no great effect on the boundary layer.

The greatest influence on the turbulent boundary layer is exerted by the choice of the turbulence grid, while the distance d_z and the flow velocity u_∞ do not have a great influence on the boundary layer.

Liquid fluctuations and PDF

Gas bubbles induce a characteristic kind of turbulence, that is also called pseudo-turbulence or bubble-induced turbulence. In contrast to shear-induced turbulence, the probability density function (p.d.f.s) show a non-Gaussian behavior (Risso 2016). When trying to emulate this specific bubble turbulence the design of the grids must take these into account, since the shear-induced turbulence is increased and shifts the p.d.f. more and more to a Gaussian profile. In Risso (2016) and Cha. 1 a detailed description of the p.d.f.s behavior is given. Measurements with a homogeneous swarm at a wide variety of Reynolds numbers were evaluated and normalized by an empirical factor $u_b \cdot (\alpha/\alpha_0)^{0.4}$, with u_b being the bubble rise velocity, α the gas volume fraction and α_0 a reference volume fraction of 0.01. The fluctuation profile $u'(x, z, t) = u(x, z, t) - \overline{u(x, z)}$ in the single-phase flow has a convex hull in the middle and peaks near the wall (Fig. 3.7). Due to the bubble induced turbulence, the plateau widens and the peaks disappear. In the core region, the shear induced turbulence is not dominant and the bubbles and wakes are responsible for the creation of fluctuations. The shear induced turbulence becomes more influential at the wall regions with increasing liquid velocity. While $|u'_x|$ and $|u'_y|$ (span wise directions) are in the same order and isotropic, $|u'_z|$ (flow direction) reaches larger values (Kim et al. 2016). The turbulent profile is evenly distributed over the whole channel and shows no preferences in a peak development, neither at the center nor near the wall (Wang et al. 1987, Hosokawa & Tomiyama 2013). This can be also seen in the p.d.f. While the horizontal ones are axisymmetric, the vertical p.d.f. has a tail pointing to greater fluctuations (Abbas et al. 2006, Riboux et al. 2009).

In real bubbly flows the velocity fluctuation u' is mainly determined by the gas hold up α (Serizawa et al. 1975). At moderate gas volume fractions the liquid is entrained by a random bubble accumulation. In the core region the bubble wakes are more influential, while the bubbles in the near wall region reduce the fluctuations significantly.

In Fig. 3.7 the normalized p.d.f.s of the axial and radial velocity fluctuations for the various particle grids are shown. The horizontal fluctuations Fig. 3.7 (top) for all grids are symmetric, while the fluctuations in flow direction show a non-isotropic behavior with strong upward fluctuations. In both plots, a comparison with the results published in Riboux et al. (2009) is made. Also, a scaling factor $u = U_0 \cdot \alpha^{0.4}$ for the velocity fluctuations is provided so that the p.d.f.s become self-similar. This scaling was first proposed by Risso & Ellingsen (2002). For this experiment, the bulk velocity U_0 was chosen as the bubble rise velocity. For the different grids, the overall shape is similar to the one in real bubbly flows, but some of the grids compare better to the data taken from real bubble flows. As stated, the vertical fluctuations decay exponentially. All the grids show this behavior. However, in comparison to the real bubble flows show differences in the horizontal fluctuations. Due to the strong wake, the p.d.f. shows a trail to higher fluctuations that can only be seen in some of the grids. For example, as can be seen in Fig. 3.7 and Fig. 3.8, the spherical 10 mm - 10 Vol.-% and elliptical 5 mm - 3 Vol.-% shows a developed shifted p.d.f.. For the other grids, the p.d.f. are almost symmetric in the vertical direction, like the 5 mm - 10 Vol.-% or the rigid grid. Therefore, a detailed comparison with the data published in Risso (2016) is shown in Fig. 3.8 for the horizontal fluctuations and for the vertical fluctuations. Risso describes the turbulence is comprised of three different effects, the wakes, the turbulence in the liquid and the potential flow generated by the bubble rising while assuming the bubbles move independently of each other. For the

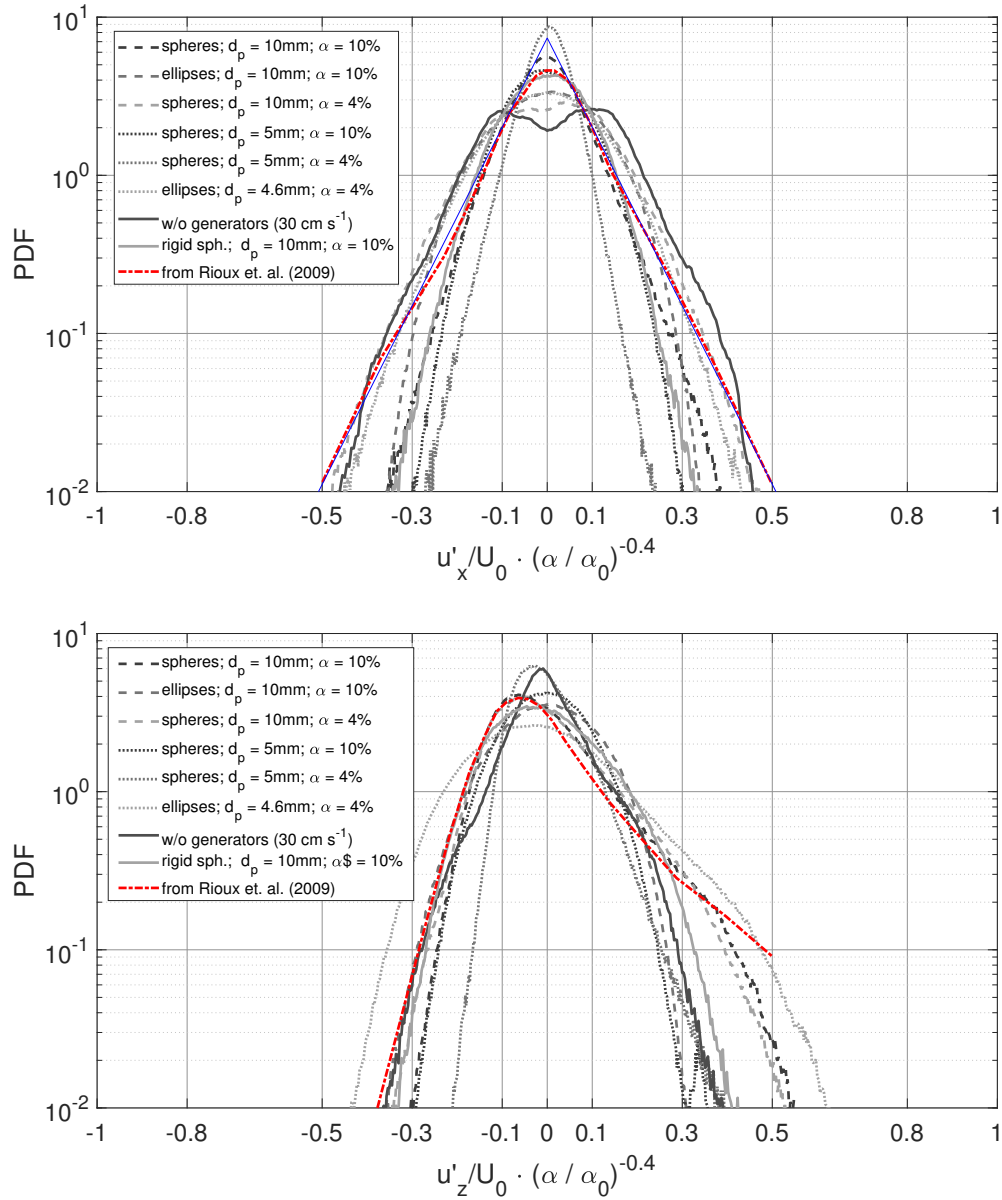


Figure 3.7: Comparison of the normalized p.d.f. of horizontal (top image) and vertical fluctuations (bottom image) for all grids. Both are normalized and scaled with the volume fraction. ($\alpha_0 = 0.001$ and U_0 is the mean bulk velocity). Published in Schlüter et al. (2021) and reprinted with permission.

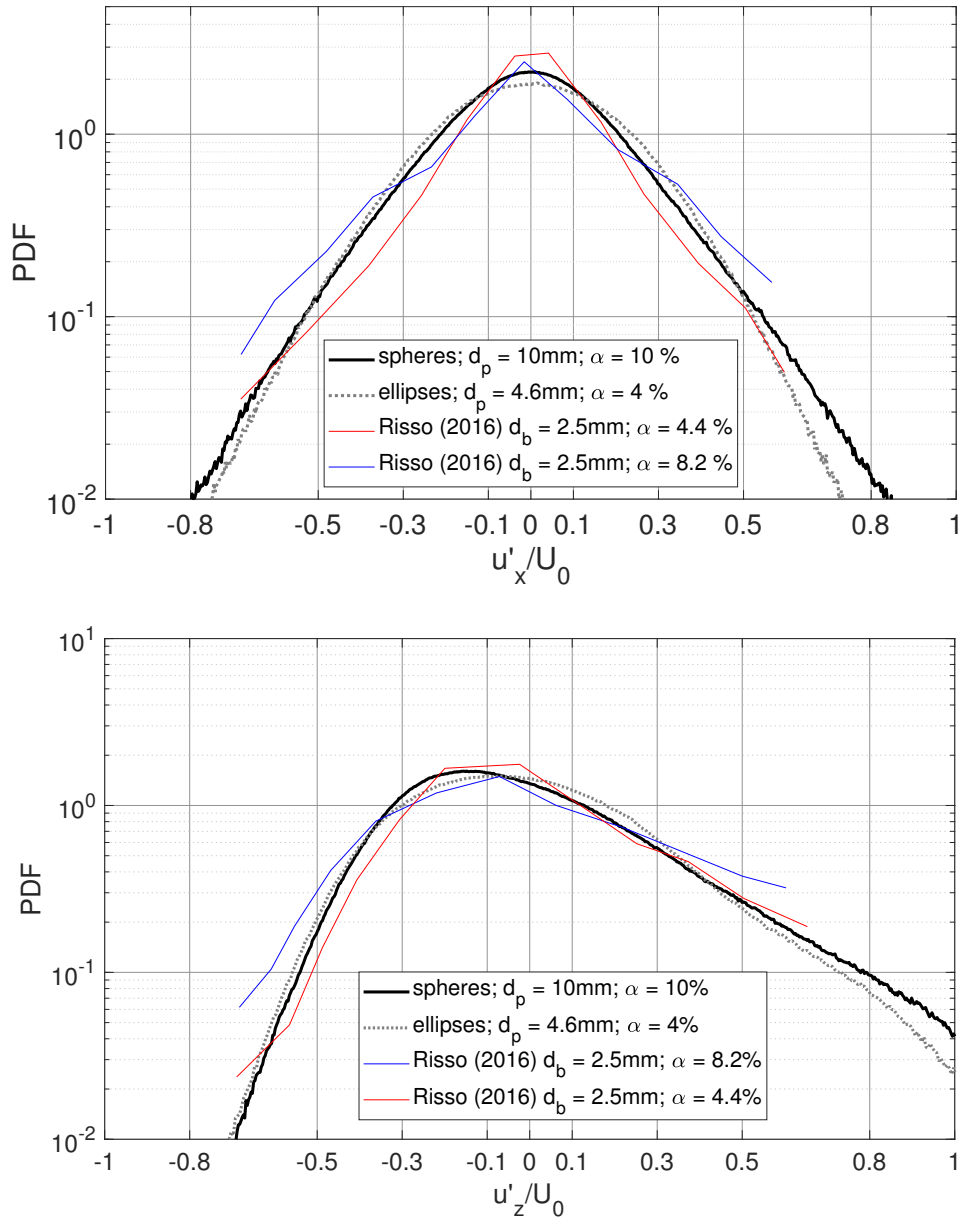


Figure 3.8: Top image Shows the normalized p.d.f. of liquid velocity fluctuations in span wise direction and the bottom in the flow direction in comparison with measurements published in [Risso \(2016\)](#) that were performed for different bubbles sizes and volume fractions. Published in [Schlüter et al. \(2021\)](#) and reprinted with permission.

grids, these different agitations can be explained by the following. The wake effect is mainly introduced by the sphere/bubble size which for the grids is fixed and set by the grid element diameter. For the 10 mm spheres the wakes are brought and induce constantly strong fluctuations, which results in an overall shift of the p.d.f. shape to higher fluctuations. With the elliptical shape of the small elements mainly fluctuation in the size of the particle are induced, but due to the tumbling motion and changing of the effective radius, a broad range of fluctuation scales are generated. This phenomenon gives the p.d.f. also a shift to higher fluctuations but with a slower decline. The second portion is due to the particle movement, the volume fraction and space the particle strings can move in. While the grids with a high-volume fraction do not allow the elements to move, the p.d.f. becomes thinner and the volume fraction is overall responsible for the width of the p.d.f. . The potential flow in this setup is provided by the counter flow since this emulates the bubble rise velocity. This effect is responsible for the height of the p.d.f. . However, since the data is normalized with both the volume fraction and the mean bulk velocity the shape is only dictated by the induced wake and freestream entrainment, and following from that the fluctuations. One can conclude that the grid induced turbulence, resulting from the spherical 10 mm and 10 Vol.-% and elliptical 5 mm and 4 Vol.-% shows the best accordance with the p.d.f. and generated by a real bubble swarm the best agreement with real bubble swarms (Risso 2016).

Liquid energy spectra

Various experimental and numerical publications report a specific behavior of the energy spectra in pseudo turbulences such as the bubble-induced one (Risso 2011, Martinez et al. 2009). The energy spectra of bubble induced turbulence are independent of d_b and α (Risso 2011). In Risso (2011) the energy spectra of a bubble swarm, after it passed the measurement section, are calculated from PIV with a spatial fast Fourier transformation (FFT) in flow direction. Pannek et al. (1994) measured the spectra with constant temperature anemometry. Divided into three sections the spectra can be described as follows: Below 10^2 Hz the spectra show a $\lambda^{-5/3}$ slope, which describes the classic Kolmogorov inertial subrange. Above 10^2 Hz till approximately 10^3 Hz the spectral energy density follows a λ^{-3} law. These regions are both independent of d_b , the bubble diameter and α , but scale with the integral length scale Λ . In Riboux et al. (2009) a value of $\Lambda = 15$ mm for the spectra in flow direction is given. The integral length scale Λ can be calculated as the first value in the spectra normalized by the mean velocity and indicate the biggest possible fluctuation. The $-5/3$ law describes an isotropic turbulence, where the eddy cascade is resulting purely from shear flows. In Michiyoshi & Serizawa (1986), hot film anemometry is presented that revealed a $-8/3$ power law. This adjustment of the exponent can be used as an indication to distinguish between purely isotropic turbulence and turbulence induced by bubbles.

To characterize the time-resolved energy spectra of particle grids, EDM is used to measure the power spectral density. These measurements are performed utilizing the flow channel at the University of Bremen. Comparable grids are used and the results evaluated with the measurements in a real bubble column. Mießner et al. (2017) compare the energy spectra taken in real high dense bubble swarms with that under the elliptical particle grids ($d_p = 4.6$ mm, 4 Vol.-% and 10 Vol.-%). Both, a real bubble column in co-flow ($u = 80$ mm/s) with a volume fraction $\alpha = 4.24$ Vol.-% and the free moving particle grids are characterized with the time-resolved EDM. The mean counter flow is set to 0.15 and 0.30 ms^{-1} . In Fig. 3.9 the $-5/3$ slope derived from Kolmogorov's law as well as the $-8/3$ to indicate the energy cascade slope of bubble-induced swarm turbulence is inserted. The transition is between the initial turbulent energy, and the onset of the energy cascade can serve as a reference length L since the wake structures of swarm turbulence arise in the bubble dimension ($d_b = 5$ mm). In Mießner et al. (2017) a deduction of this scaling is provided. The largest eddies that need to be considered for the bubble motion and deformation are in the order of three times the diameter. Larger ones result in a lateral movement of the bubble. The appropriate frequencies to this range of bubble diameter are between $15 < f < 50$ Hz, which are highlighted in Fig. 3.9. In the energy dissipation range, different zones with characteristics comparable to Kolmogorov's law can be recognized. The slope of the spectra for real bubble flows, and the particle grid is in good agreement with each other as can be seen in the highlighted area in Fig. 3.9. Thus, a good comparison between the particle

induced and real bubbly flow turbulence can be observed for the given conditions.

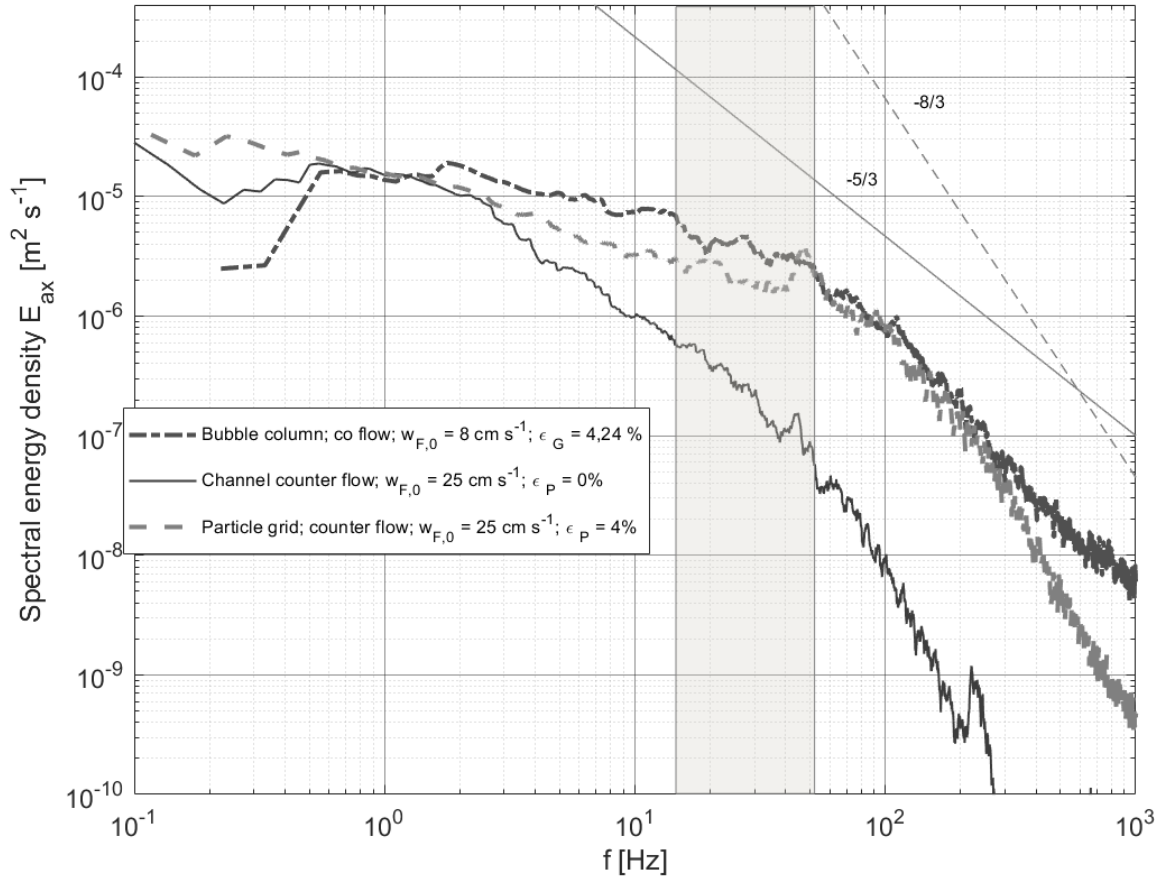


Figure 3.9: Energy spectra measured with EDM at the facility at the University in Bremen. The $-5/3$ and $-8/3$ slopes are added. The range of frequencies that are responsible for the bubble deformation are marked. Published in [Schlüter et al. \(2021\)](#) and reprinted with permission.

To further describe the flow, the integral time and length scales for the dominant largest structures can be derived from this time resolved signal and its auto-correlation function. The similar time scale describes the longest periodic flow structure that can in turn be used to describe the length scales by applying the Taylor's hypothesis. In [Mießner et al. \(2017\)](#) a detailed analysis regarding the length scale and turbulence level is given. Mießner describes that the particles introduce turbulence with the initial length scale of swarm turbulence. As well as stated by Mießner the devices generate a variety of length scales. While on the lower half of the considered range the grids produce smaller values while in the higher frequency ranges larger scales.

Determination of diffusion as a function of Turbulence

One important factor to take into account when evaluating the grids, or rather their capability of recreating bubble-like agitations, is the diffusion behind them. This is important especially for the mass- and heat transport. Due to the fact that the mixing is strongly dependent on the turbulent diffusion, this is also one aspect that needs to be looked into. For this purpose, tracer particles were injected locally at different positions in and below the

grids and their propagation was recorded and analyzed over time. In order to achieve a high contrast, the tracer particles were illuminated with a laser sheet. To determine the diffusion, the time-averaged cone formed after the addition of the particles was examined. Care was taken to ensure that the injection velocity was adapted to the velocity of the fluid in order to avoid shear effects due to speed differences. An adaptive threshold method was used for segmentation. This method considers the average image intensity for different threshold values and applies them to each other. If the slope of the graph changes, the final threshold value is set and a binary image is created. An entropy filter was used to determine the contour of the cone. For the evaluation of the diffusion the respective opening angle was considered. As was to be expected from the turbulence measurements, grids with an increased degree of turbulence show a wider cone. As the distance between the injection device and the grid increases, the cone also becomes narrower; this shows that the turbulent diffusion decreases with the distance to the grid.

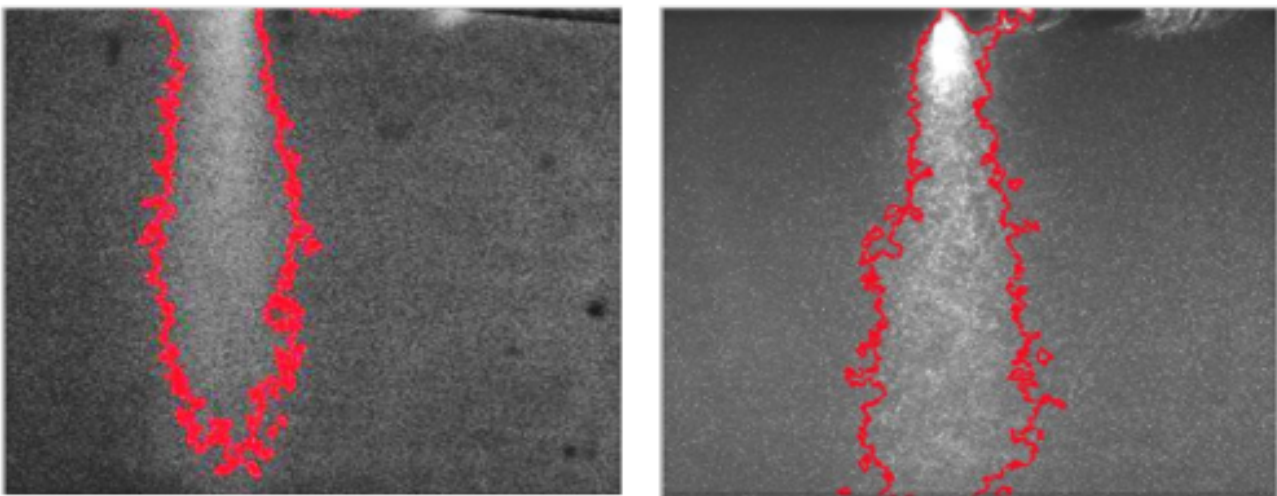


Figure 3.10: Example of diffusion visualization using PIV tracer particles. Shown is the time-averaged image behind (right) a grid with round particles (left) with elliptical particles.

The first aspect looked into is the flow rate. The higher the flow rate is, the narrower the cone gets. This is a direct result of the increased flow velocity that prevents the flow to develop and transports the larger structures perpendicular to the flow of the channel. Due to a lower flow rate the turbulent structures are not immediately transported away but rather have time to develop. Also, important here was the position of the inlet with which the tracer solution was injected. Three different positions were picked, one above, one in and one below the grid. The first position discussed had the tip placed below the last row of the grid elements; the second image has the outlet roughly in the middle of the grid, and the third image roughly in line with the top row on the grid. Is the tip placed below the grid, the induced turbulence from the grid mostly already decayed or lost the strength to influence the jet. The higher it is placed the stronger the turbulence are and a greater diffusion is archived. The third comparison was of the particle shape and volume fraction that is mounted in the grid. In agreement with the turbulence levels shown in [Fig. 3.10](#) the ellipsoid particle grids show greater diffusion strength. Same holds true for the grids volume fraction. In conclusion the particle size shows a biggest influence on the diffusion compared to the volume fraction.

Conclusion

In the present work, the flow statistics behind free moving particle grids with different characteristics were evaluated by using PIV. Also, EDM was used to measure the spectral density of selected particle grids with elliptical elements and a volume fraction of 4 % as well as in comparison to a bubble swarm with properties like multiphase flows in industrial reactors. The aim of this chapter is to characterize the specially designed particle grids and evaluate the induced turbulence to clarify whether they mimic the flow and turbulence introduced by real bubble swarms or not. From the PIV data, the spatial distribution of the velocity, turbulence, and the velocity fluctuations are calculated. It is shown that the turbulence characteristics can be controlled over a broad parameter range by varying the size, shape and volume fraction of the particles and by selecting the suitable location measurement position. It can be stated that the larger the particles and the higher the volume fraction, the larger the turbulence level behind the particle grid becomes. While grids with 10 mm particles introduce greater velocity fluctuations than the small 5 mm spheres, for all grids it takes ~ 5 particle diameters for the disturbed flow to relax back to the bulk velocity and generate a flow with homogeneous turbulence. By comparing the particle form, the elliptical particles introduce a greater turbulence level than the spherical one. Regarding the velocity and turbulence decay with increasing distance, the grid with small elliptical elements shows an exponential decay that is in the same order as the real bubble induced turbulence (Risso et al. 2008a). By comparing the p.d.f.s for the velocity fluctuations behind the different grids, not only the small elliptical grid, but also the spherical grid with 10 mm and 10 Vol.-% show good agreement. This in turn is also comparable to real bubble swarms with 2.5 mm and 4-8 Vol.-%, as shown by comparing to the p.d.f.s taken from Risso's publication (Risso 2016).

The EDM measurements further give insight into the integral length scales and scale distribution. For this, a real bubble swarm with a gas hold-up of 4.24 Vol.-% was measured as a reference. By comparing the respective energy spectra in the relevant frequency range, a good agreement can be found for the grid with 5 mm elliptical elements and a volume fraction of 4 Vol.-%. To find the right condition for designing an experiment, it has to be considered that the influence of the individual grid elements is still measurable in the vicinity of the grids. It can be solved by conducting experiments roughly 3-4 particle diameters further downstream from the grid this leads to a homogeneous flow profile several particle diameters downstream.

The rigid particle grids produce much lower turbulence levels due to the missing random motion of the particles. Due to the random movement of the particles in different particle layers, the turbulence varies strongly, as typical for real bubble flows.

Furthermore, different length scales are generated by the randomly moving particles and constantly changing entrainment of the free stream between the particle strings. These length scales were measured and characterized by EDM and discussed in detail in Mießner et al. (2017). The devices induce a range of length scale, while on the lower half of the considered range the grids produce smaller values while in the higher frequency ranges larger scales. Taking all these factors into account, we can conclude that these flexible grids generate a good, but not perfect model swarm-turbulence. Hence, it allows conducting experiments with small bubble swarms or even single bubbles in a swarm like background turbulence with optical measurement techniques without introducing disturbances with probes.

3.3 Fractal Grids

Since the particle grids still utilize moving parts, it would be desired to eliminate them and create the same turbulent statistics with a rigid grid. Taking inspiration from wind tunnel experiments, fractal grids are often used to create and model turbulence with specific parameters. In Hurst (2007) rigid grids are described to induce fluctuations that are homogeneous and isotropic, but with only moderate Reynolds numbers. To reach higher Reynolds numbers Hurst suggests fractal grids. These are self-repeating patterns, like squares, cross-shapes or I-shapes. The shape and family (number of repeating elements) of the grid as well as the number of iterations

and the bar dimensions (length and thickness) can be completely described. For the experiments presented here, a space filling square grid was used. This means that the grid parameters were chosen in a way that as little as possible undesired free space was left. For example can it happen that a grid with an I-shape as its repeatable object is designed, that some spaces especially in the middle of the grid is unoccupied (see Fig. 3.11). The grid used in this experiment consisted of squares and had the following statistics: blockage ratio is 25% and the thickness and the length of the biggest element in the middle is 45 mm and 3 mm respectively. To the next iteration the length and the thickness are halved. In total the grid has 4 iterations (See Fig. 3.11). Analog to the free moving particle grids the flow behind the fractal grid is evaluated according to the velocity profile, turbulence and p.d.f.s. Since the spectra was measured at the University in Bremen with the EDM probe this could not be done for the fractal grids.

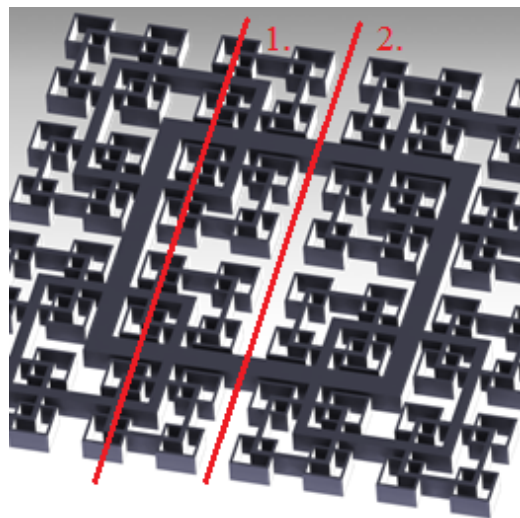


Figure 3.11: Example of a square fractal grid.

Velocity Profile

As can be seen in Fig. 3.12 there is significant difference between the center line profile (Fig. 3.11 2) and the one under the smallest structures (Fig. 3.11 1). Due to the gap in the middle of the space filling fractal grid, it was expected to see a jet like profile in the middle. Hurst (2007) showed that the turbulent profile in flow direction has a peak, at $x_{\text{peak}} = 75 \cdot t_{\text{min}} T / L_{\text{min}}$ For the current setup this would lead to a peak position ~ 700 mm downstream and cannot be seen in the measurements. While the rising slope of the turbulence is visible in the center line measurement, it decays, similar to the flexible grids underneath the small structures.

Turbulence and Isotropy

In Fig. 3.13 the turbulence, calculated analog to the free moving particle grids is shown. The left image again plots the turbulence distribution under the small elements. Line 1 in Fig. 3.11. The right image shows the turbulence under line 2. While the turbulence is rather homogeneous under line 1 and the profile under the small structures evenly distributed, the distribution under line 2 shows a reduction of the turbulence of about 20%. In order to create also a homogeneous inflow in the middle area one would need to design the fractal properties

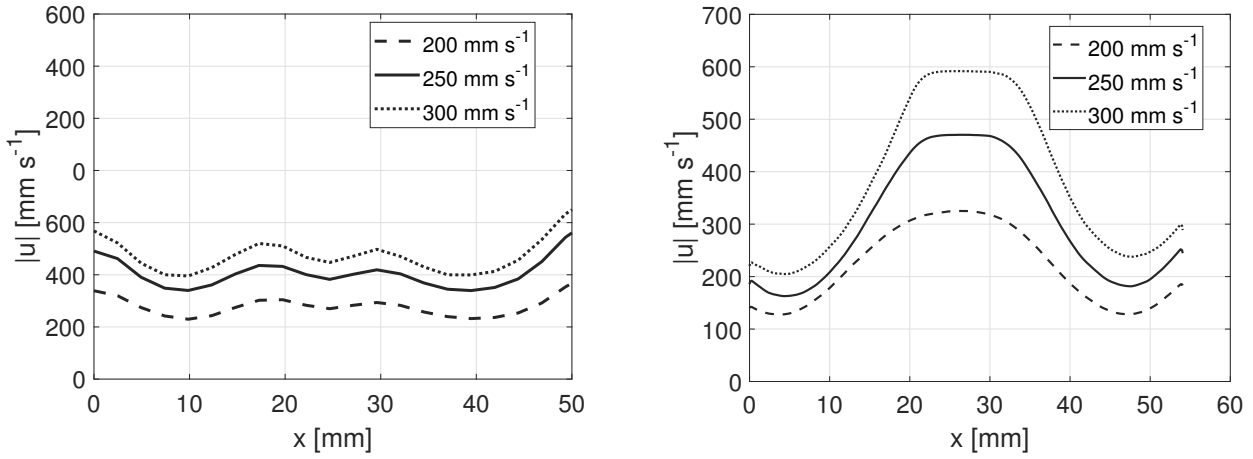


Figure 3.12: Mean velocities left: across small grid elements (line 1); right: in the center of the grid (line 2)

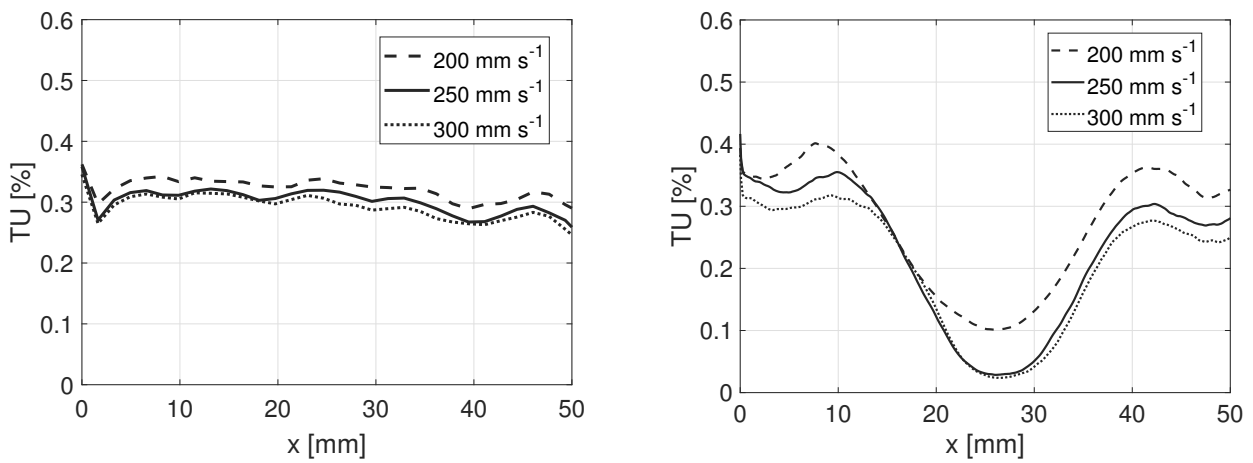


Figure 3.13: turbulent intensity left: across small grid elements (line 1); right: in the center of the grid (line 2)

differently to create similar statistics to the free moving particles. Due to the small width of the channel, t_{\min} needs to be smaller than 0.6 mm which cannot be achieved in the current channel setup.

For the fractal grids also the p.d.f.s were calculated at the same positions as the mean velocity or the turbulence field. A comparison of the different positions at a velocity of 250 mm/s is shown. In comparison to the free moving particle grids, this data is normalized with the swarm density, since it is not feasible to define a swarm density for the fractal grids. Therefore, the raw data is plotted, even though the absolute values cannot be compared, the shape however can still be evaluated. In Fig. 3.14 (left) the p.d.f. in channel normal direction and in Fig. 3.14 (right) in flow direction is shown. The different lines show positions underneath the grid. One measurement was taken directly in the middle of the channel (in Fig. 3.11 line 2) and one parallel to it underneath the smallest grid elements (in Fig. 3.11 line 1)

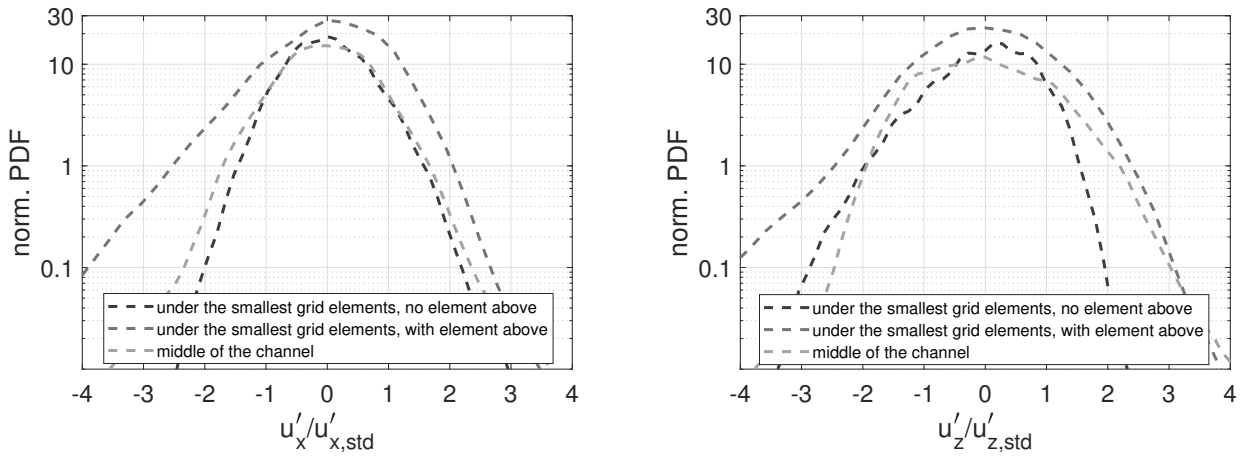


Figure 3.14: Comparison of the p.d.f.s underneath the fractal grids. In contrast to the free moving particle grids, there was no scaling of normalization done, since a definitive volume fraction that is comparable to real bubble swarms cannot be made. across small grid elements (line 1); right: in the center of the grid (line 2)

It can again be seen that the p.d.f. leans to one side, however for the fractal grids to the negative side. Both the horizontal and the vertical fluctuations show an asymmetry which is not present in either the real bubble flow or the free moving particle grids. Besides that, the measurement shows a strongly divergent behavior depending on the measurement position. Is the measurement taken underneath the smallest grid elements, the p.d.f.s show some resemblance with real bubble flows. Is the p.d.f. compared underneath the free stream no such resemblance can be seen and it rather compares to a free jet.

Results

The free moving particle grids and fractal grids are compared. A PIV measurement at different locations, here in the middle of the channel and underneath the smallest elements, give insight in the flow and the flow structures that are created with those grids. In comparison to the free moving particle grids, the flow generated, by the fractal grids shows strong inhomogeneous fluctuations shortly downstream. According to the literature the homogeneity starts to develop for this certain grid around 700 mm after the grids. Which is not feasible in the channel in our setup with a maximum length of 1000 mm and the first option to produce bubbles at 100 mm. However, there would be design options to reduce that length by introducing smaller elements, but these would be hard to manufacture and are also unstable. If a channel provides ample length though, as well as a suitable

measurement section, regarding the width, a fractal grid could be designed to fit those needs. Other factors that need to be taken into account are the fluctuations and the energy spectra. Not only is a homogeneous flow important, but so is the statistics of the fluctuations. Here the p.d.f.s show a difference in the cross-section in regards if there are small elements present or not. For real bubble swarms the p.d.f. perpendicular to the flow direction was rather symmetrical, while in flow direction more leaning into to the negative side with a long arm in the positive. The p.d.f. taken underneath the small elements show a similar shape however leaning towards the right side with a long arm into the left/negative side. To note is, that no comparison can be made in regards to the absolute values due to a lack of normalization. It can be said that even though the p.d.f.s do show some sort of similarity it's not enough in that regard to be able to say that the flow characteristics are similar. The last aspect, the energy spectra, was however measured in the University in Bremen and no comment can be made in that regard. In conclusion, the fractal grids do not compare to free moving grids since they show too many differences to be comparable with the real bubbly agitation. They can be used however to create high intensity, homogeneous flow with enough length, but for this experiment they are not suitable and the free moving particle grids will be used further in the experiments.

3.4 Summary and Conclusion

Overall, the chapter can be summarized with that the free moving particle grids are a good way to emulate bubbly flow statistics similar to real bubble swarms. One thing to be aware of is that the right sphere size and volume fraction is chosen. A good agreement with the flow statistics in a bubble swarm could be found in the particle grids with elliptical elements and a volume fraction of 4 % and the one with 10 mm spheres and a volume fraction of 10 %. Those show in the velocity distribution, the distribution of the fluctuations, the p.d.f and the energy spectra a good resemblance to real bubble swarms. Of course, one need to keep in mind that they are still just a model and are not an accurate recreation of a bubble swarm. For example, an interaction of the bubbles is not modeled and even if the flow statistics are similar other bubbles are not physical present in this flow, which also effect the behavior of the bubble. This can be seen later in [Cha. 5](#). But not the less those grids create a satisfactory flow statistic and will be used in the further experiments. If not specified otherwise the elliptical grid is commonly used in the experiments.

In contrast to the free moving grids, the fractal grids show a big discrepancies and disadvantages compared to the free moving grids. Not only are they hard to manufacture, especially the smaller repeating parts. The grid used here was 3D printed and the resolution was not sufficient enough to create smaller iterations of the pattern. In addition the flow only fully develops roughly 700 mm behind the grid and with a total length of 1000 mm for the measurement section this is not acceptable. Furthermore, the p.d.f.s don't show the desired shape nor the turbulence distribution.

To conclude this chapter the free moving grids, provide an easy and good way to create the desired turbulence. As a small outlook the active grid should also be mentioned again here. While this grid would provide a easy way to quickly change the turbulence statistics, intensities and even the length scale it was not possible to physically install it in the channel. This requires a either new location for the measurement channel or a redesign. This would go beyond the scope of this thesis.

4 A novel approach to describe 3D bubble deformation with a tomographic reconstruction

4.1 Introduction

The transfer of chemicals from the bubbles into the liquid depends strongly on the shape of that bubble that is not only oscillating on its own but also highly influenced by the flow state of the surrounding medium (laminar/turbulent). The size of the bubble is therefore an important parameter, since larger bubbles deform in a more complex manner (Clift et al. 1978) than smaller bubbles that are more from stable. This results in a variation of the surface area, which can have an effect on the transfer of chemicals through the interface. The wake structure of the bubbles and the generated turbulence level depends on the size, shape and oscillatory mode. In order to understand how the mass transfer depends on the flow state and the bubble deformation, it is necessary to investigate the details of the bubble dynamics in a turbulent flow. In addition, since the flow and the influence on the bubble is a three-dimensional problem it is also necessary to evaluate this in all three dimensions and not only with a 2D projection. In the last few decades bubble oscillations have been discussed in a various numbers of literature, in Loth (2008), Hasslberger et al. (2018) and Liu et al. (2005) an overview over this topic can be found. However, those examinations mainly focus on small bubbles, or freely rising bubbles without the influence of flow statistic of the liquid. The specific aim of this chapter is to create an experimental method to characterize the three-dimensional shape of small and large bubbles and compare it to the methods published. Another criterion is that the surface should not be contaminated to not influence material properties, like the surface tension. Even though one method with markers on the surface is introduced the main focus is on an optical method. The here proposed method is used based on a tomographic reconstruction (the image is based on the view of four or more cameras from different directions) and is solely based on the shadow images of a bubble. First the experimental setup is described, followed by an analysis of other methods already published and finally compared with each other. Parts of this chapter and some figures are published with permission in Schlüter et al. (2021).

4.2 Experimental setup

The experiments were conducted in the counter current channel (see Fig. 4.1) at the Universität der Bundeswehr in Munich. Four LaVision Imager Pro HS cameras were used to record data. To improve the bubble shadow images, LED backlights were installed on the opposite side of the cameras. The commercial software DaVis from LaVision was used for the recording. Since the bubbles can move freely over the whole channel, a large measurement volume is desired. However, for the tomographic reconstruction a high spatial resolution is wanted to get a good reconstruction result, so the volume has to be rather small. A small measurement volume also allows resolving small amplitudes of the shape oscillations. A compromise was found with a $20 \times 20 \times 20 \text{ mm}^3$ volume. The measurement volume was located in the middle of the channel to avoid wall interactions and boundary layer effects.

By adding additional tracer particles in the fluid, it is also possible to simultaneously measure the flow around the bubble. However, in this chapter only the shadow images of the bubbles are needed. Thus 'images' only refers to the shadow images, even though the particle images were recorded simultaneously. The laser was

triggered alternating between the LED shadow images. The laser and LEDs are alternating between each other. The total recording frequency was 1200 Hz. This results in a frequency of 600 Hz, for both shadow images and particle images. With this recording rate oscillations up to 300 Hz can be resolved.

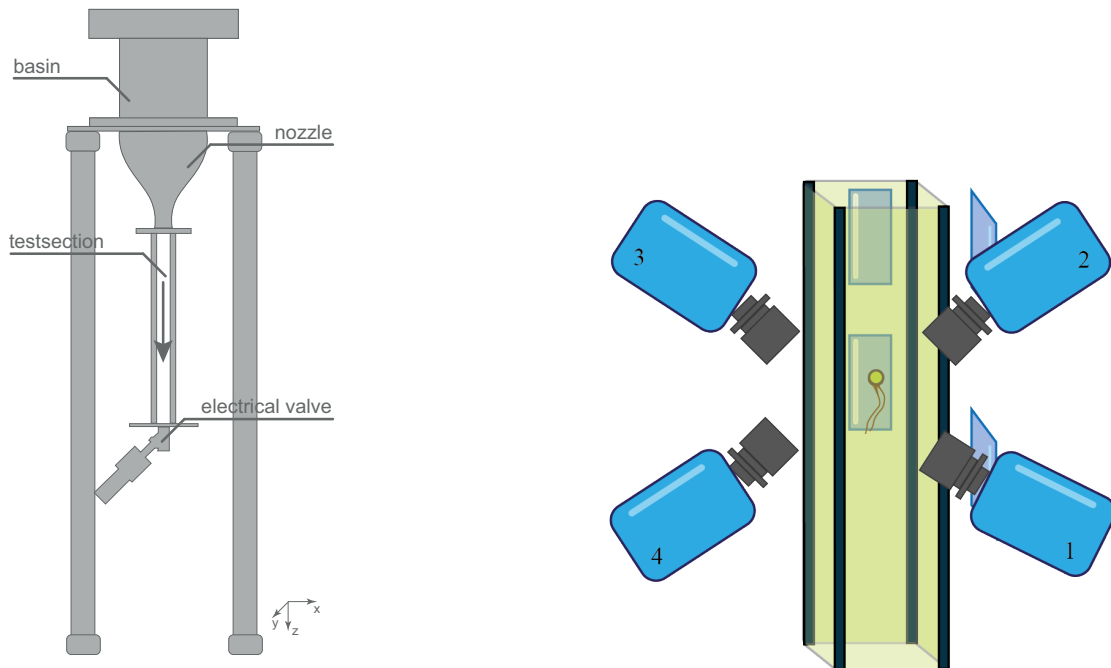


Figure 4.1: Schematic diagram of the counter current channel (left). The flow velocity is regulated by an electric valve at the end of the measuring section. In order to generate a continuous flow, the fluid is pumped back into the water basin. The turbulence generators are located between the measuring section and the nozzle. Schematic representation of the camera setup (right) with controlled background lighting. White LEDs are used as backlight for better contrast in the shadows. Published in [Schlüter et al. \(2021\)](#) and reprinted with permission.

To keep the bubble in this measurement volume for a sufficiently long period of time, the flow speed in the test section was aligned with the raising speed of the bubbles by using an electronic control valve at the lower end of the channel. To ensure a homogeneous inflow with desired turbulent velocity fluctuations, a turbulence generator (described in [Cha. 3](#)) was installed above the measuring section. The turbulence generator consists of solid particles with a specific size, shape, and volume densities that were arranged in a regular manner by using thin yarn. Thanks to the flexibility of the yarn, the particles can oscillate around their equilibrium location under the influence of the flow. For the experiments, a grid with 5 mm ellipses and 10 % by volume was used. These grids can be used to create flow agitations similar to bubbly swarms in the near field behind the particles. The comparison can either be found in [Cha. 3](#) or [Haase et al. \(2017\)](#). However, due to spatial restrictions in the channel the measurement volume was placed roughly 50 mm behind the grids. Here the turbulence intensity is roughly 15-20%, which is depending on the grid 5% lower than in real bubble swarms, however the velocity is more homogeneous (compare [Fig. 3.3](#) and [Fig. 3.2](#)). This has to be done since the spatial restrictions in the channel mount did not allow for a higher placement of the cameras. It would have been possible to place the cameras in a way that they look at a flatter angle, but this reduces the quality of the reconstruction. In addition this made it also possible to compare the results with numerical simulations done by [Hasslberger et al. \(2018\)](#).

The four camera images were binarized and both evaluated in a 2D manner and with the new 3D algorithm. To preprocess the raw images only a mean image (taken over all recorded images) was subtracted and finally binarized with a threshold. Due to the background illumination the bubble could easily be detected by a threshold. The data itself was not enhanced or otherwise post processed. 2D evaluation was performed to compare it to published results and verify the 3D reconstruction. For the 2D evaluation two perpendicular projections of the 3D bubble were used to calculate the in-plane deformation. The 3D evaluation uses all four images. Note that the experiment did not use telecentric lenses and the axis has a dependence on the 3D position. And therefore, an artificial oscillation that represents the path movement is embedded in the data. One additional method is shortly introduced as well that would allow for a full reconstruction of either concave or convex surfaces based on attached particles to the surface. For the reconstruction measurement, 3.5 mm and 4 mm bubbles are used. The bubbles were created 0.5 m below the measurement volume with appropriate nozzles to ensure the path is established before the measurement was taken. The size of the bubbles is highly reproducible (tested with a 2D shadow image of 50 bubbles, the error was below 1%). For each measurement, several bubbles were released in the channel with at least 50 bubble diameters between them to avoid wake interactions. Some aspects that lead to errors in the measurement are the surface tension. Even though the channel was cleaned of all remaining surfactants, the water from the distillation was not fully cleaned and the rhodamine tracer particles also tend to stick to the bubbles surface, which also have an influence on the surface tension and the deformability. The influence of the surfactants and the terminal rise velocity and the shape deformation dependent on the surfactant have been measured by [Tomiyama et al. \(2002\)](#). They state that the shape and the velocity is highly dependent on the purity of the system. The primal role of the surfactant is to hinder the shape oscillations.

4.3 Comparison of different methods

Tracer particles on the Bubbles surface

The simplest approach for a truthful reconstruction is to sample the bubble surface with tracer particles. The position of those particles could then be triangulated to create the 3D bubble surface. This would allow constructing any kind of surface. For that specially designed particles, so called Janus Particles (bought from Cospheric) can be used. These particles have a hydrophobic and hydrophilic side. A example of the particles attached to a set of bubbles in a test tube is shown in [Fig. 4.2](#). To attach the particles to the bubble various methods, like micro channels and simple shaking of a tub were conducted. However, the particles either did not stay at the surface or are moved to the lower pole of the bubble due to gravitational forces. Because no satisfying result could be achieved this approach was not continued and is only mentioned here. Besides that, the particles are not stable on the bubbles surface and have a massive influence on the surface tension, which makes optical and non-intrusive methods more attractive.

2D reconstruction

The next easiest step is to evaluate the bubbles shape by a 2D stereoscopic recording. This was used in several publications: Shadow images recorded from two perpendicular sites ([Brücker 1999](#), [Veldhuis 2007](#), [Veldhuis et al. 2008](#)). From the binary images the major half axis for all views were determined by fitting an ellipse to the data points. Analog the equivalent major axis was calculated with $e = \sqrt{d_D d_M}$ and the Ratio with $R = \frac{d_D}{d_M}$, where d_D and d_M denote the measured major axis in the direct and mirrored image. Since Lunde and Perkins used a mirror to record the bubbles from two sides the subscript M (mirror) was chosen. For a in detail description refer to [Lunde & Perkins \(1995\)](#) and [Lunde & Perkins \(1998\)](#). In the work presented in here the notation was kept for a better comparison, but note that all the images were taken with an individual camera. So, in this work D and M mark two cameras that are viewing the bubbles under a 90 angle.

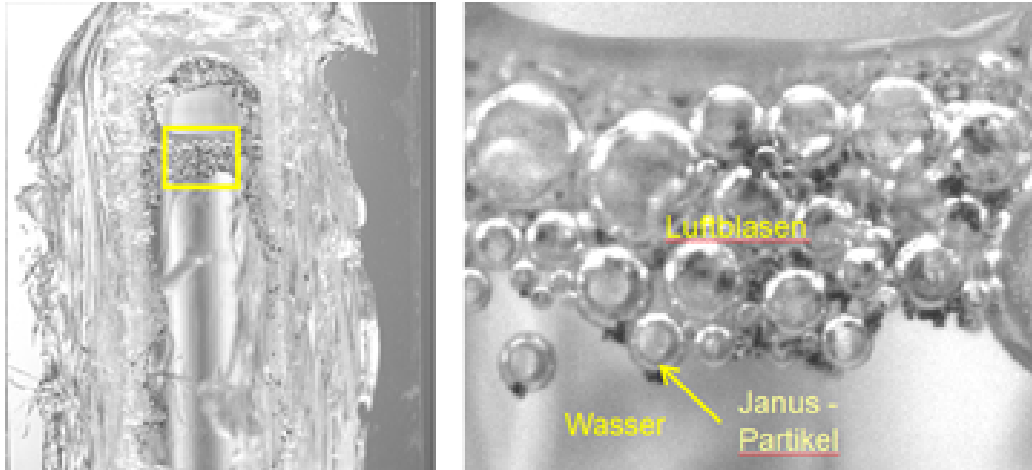


Figure 4.2: Example of bubbles with attached Januspartikles. The left shows the bubbles and particles in a testing tube, while the right one shows that the particle are moved to the bottom pole of the bubble.

The fitting method used by [Lunde & Perkins \(1998\)](#) is also often used in pattern recognition ([Granlund 1972](#), [McLeod 2011](#)). This will allow describing bubble outlines that cannot be approximated with ellipses anymore. They used Fourier descriptors to fit ellipses to the bubble outline. But by using the higher harmonics the bubble shape can be described in more detail. The Fourier descriptors (FDs in the following) are calculated with:

$$A_n = \frac{1}{K} \sum_{k=0}^K (x(k) + iy(k)) \exp\left(\frac{2\pi ink}{K}\right) \quad \text{and} \quad -\frac{k}{2} \leq n \leq \frac{k}{2} \quad (4.1)$$

In [Eq. 6.4](#) x and y are the coordinates of the bubble outline, n is the wave number in the period L and K is the length of the bubble outline or number of boundary points. The boundary (in xy -coordinates) can be written as a complex function and can be represented as a periodic function and rewritten as a Fourier representation:

$$B(l) = x(l) + iy(l) = \sum_{n=-\infty}^{\infty} A_n \exp\left(\frac{2\pi inl}{L}\right) \quad (4.2)$$

An illustrative description of the first few FDs can be given if we use only some of them for reconstructing the shape back with an inverse Fourier transformation. Are only the first two FDs used to reconstruct the outline, a circle around the center A_0 with the radius A_{-1} is calculated. By adding a factor, A_1 an ellipse is created. The outline of the bubble can be reconstructed with a certain number of FDs. In most cases, especially for small bubbles this is sufficient to describe the outline. With the data obtained from the elliptical fit, the frequencies of the major axis $e = \sqrt{d_D d_M}$ the ratio of both axis $R = \frac{d_D}{d_M}$ and the path oscillations are calculated. But for bigger bubbles additional FDs need to be taken into account to truthfully reconstruct and describe the outline (see [Fig. 4.3](#)). For more information about the reconstruction algorithm please refer to [McLeod \(2011\)](#), [Bookstein et al. \(1982\)](#).

As seen in [Fig. 4.3](#) a description with only ellipses is not sufficient anymore for large bubbles and deformations. [Bozzano & Dente \(2000\)](#) proposed a different description by separating the bubble outline into two basic shapes for the upper and lower cap of the bubble. But this is also only suitable for axisymmetric shapes. With the e -Axis and the axis ratio the shape oscillation is described. An example evaluation is shown in [Fig. 4.4](#) (left). With a Welch-spectral analysis the dominant frequencies $f_{2,0}$ and $f_{2,2}$ are then calculated from those [Fig. 4.4](#) (right). With these frequencies the bubble shape oscillation is described. For a analysis of those refer to either [Cha. 1](#) or [Cha. 5](#). In this chapter only the methods are described. From the data $f_{2,0}$ and $f_{2,2}$ were calculated to be between 40-50 Hz and 28-38 Hz respectively.

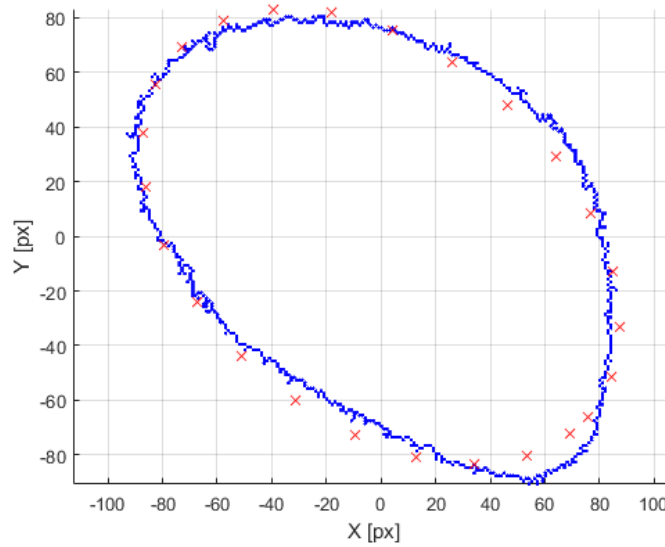


Figure 4.3: Comparison of the real boundary (blue dots) and a fitted ellipse (red crosses) of a 4 mm bubble moving in turbulent flow. It can clearly be seen that the contour is not described correctly.

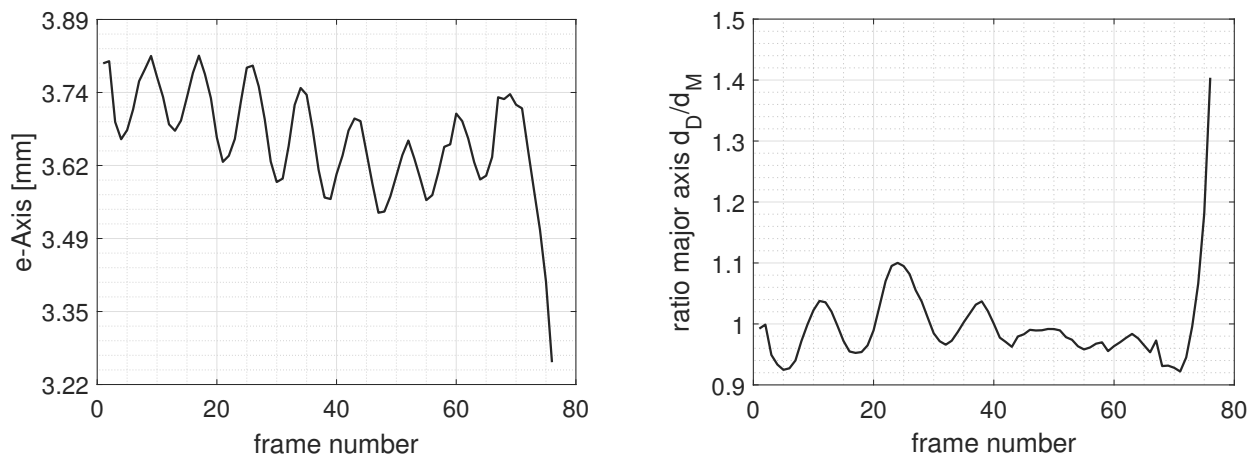


Figure 4.4: Example plot of the e-Axis (left) and the ratio of the direct and mirror major axis (right).

It is easy to see that this approach is valid for smaller bubbles that can be described by ellipses. For bigger bubbles however it is not suitable anymore to describe the shape with an ellipse and it is necessary to find a different way to describe the shape. It is important to understand the commonly used 2D analysis methods and how the published results are generated (e.g. Brücker (1999), Veldhuis (2007), Veldhuis et al. (2008)) in order to understand where the advantages and disadvantages with those methods are and how they can be improved. While the 2D methods are easy to use and evaluate, they are still just an approximation of the real bubble and introduce a systematic error and give a wrong result of the bubble shape. A detailed analysis of the errors can be found at the end of the chapter. But they are an important factor to validate and serve as a basis for the understanding of the 3D analysis of a bubble and also for comparison with the literature.

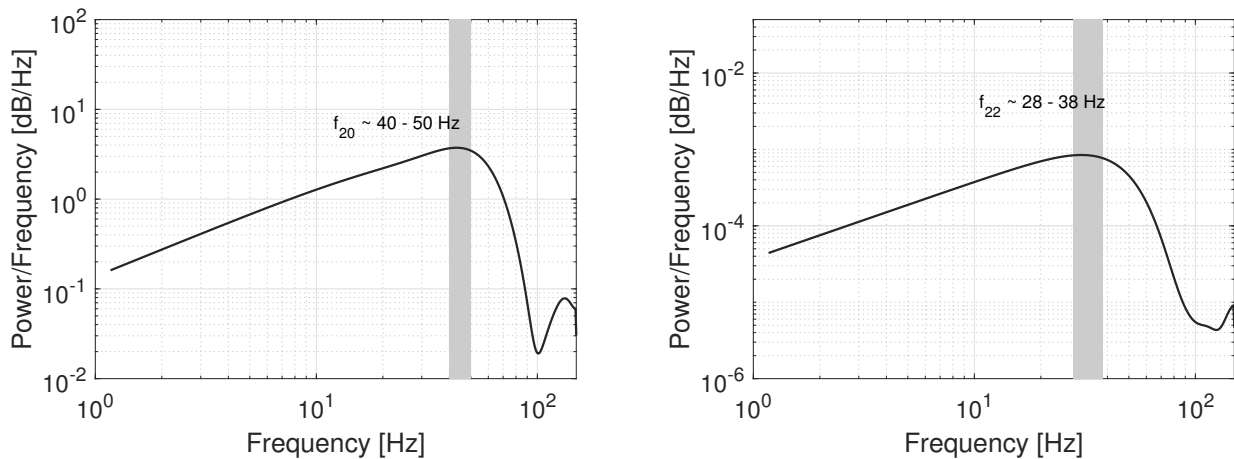


Figure 4.5: Example evaluation of the spectral analysis of the two dominant frequencies.

3D reconstruction

Even though the images are correlated with each other, a complete 3D image was not reconstructed or evaluated so far and published in the literature. Thanks to the 3D analysis approach that is presented in this chapter, it becomes possible to analyze the surface-to-volume ratio of the bubbles and its oscillation with time. The surface-to-volume ratio covers 3D effects and is in particular relevant for the estimation of the mass transfer from the bubble into the liquid medium. It will be shown that the surface-to-volume ratio is a good measure to detect and characterize periodic bubble deformations.

To fully describe not only bigger bubbles but also smaller ones a complete reconstruction of the surface is necessary. A new approach is introduced here that allows obtaining the full surface of the bubble. Similar to the 2D method again only the shadow images are needed. This eliminates the need for complicated tracer systems or other methods and allows it to use the set-up in any experimental facility as long as an optical access from at least two sides that are perpendicular to each other is available.

The 3D-surface of the bubble was reconstructed based on the shadow images of four high speed cameras with a MLOS algorithm (Elsinga et al. 2006), as it is implemented in the commercial software DaVis. The algorithm needs binarized images to calculate the 3D shape. The images were only processed by removing a background image followed by a binarization with a threshold. With a good quality image, meaning a homogeneous background image the bubble masks can be accurately created with an error of ± 2 pixels. Which translates to real world distance of 0.05 mm. Which is an error of $<1\%$ for a bubble with 3 mm diameter. Those images are then unfolded by the MLOS algorithm parallel to the calibration plate in different distances for every camera. The images are then multiplied with each other and the remaining image represent the slice of the bubble in a

certain distance to the calibration plate. In this case the calibration plate was placed horizontally in the middle of the measurement volume. Depending on the setup and the quality of the camera image, including lighting and the quality of the calibration target itself the calibration is calculated with an error of max 0.4 pixel. This error is then again introduced in the evaluation. Special care needs to be placed in the setup and the accuracy of the calibration. To improve on that, a so-called self-calibration is made to further improve the calibration. This is done by evaluation a particle image with a low particle density (less than 0.1 particles per pixel). With the low particle density, the corresponding particles can be found with a high accuracy and the calibration is corrected. This process can be made multiple times to further improve on the calibration. So, the algorithm calculates the bubble shape in a certain xy -plane (parallel to the calibration plate) with a certain z -value (distance to the to the calibration plate) and stacks them on top of each other. This can be imagined as the bubbles are built up stack wise from pole to pole. With a MATLAB-Code, splines were fitted to the data of each slice to measure the shape and finally calculate the surface area. In Fig. 4.6 an example of a reconstructed bubble is shown. Each ring represents one reconstructed z -plane. For a better visualization only, a few rings are plotted. Due to the camera arrangement the pole areas of the bubble still show artifacts. These could be removed by adding further cameras.

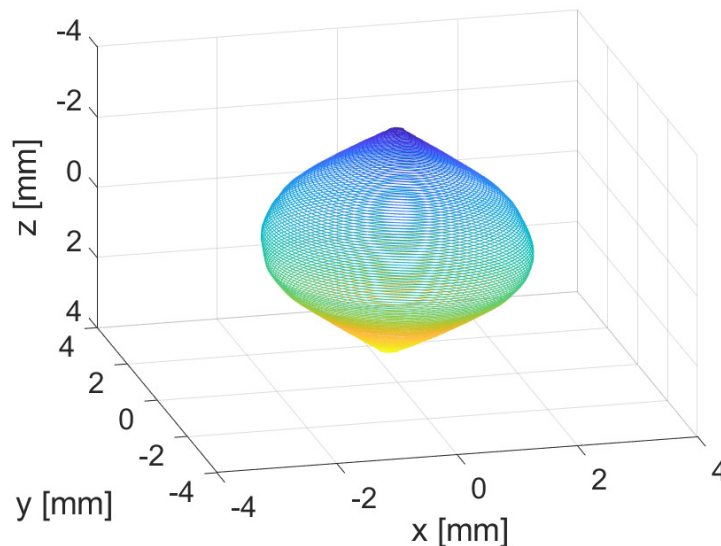


Figure 4.6: Example reconstruction. Each line represents one fit in the z -plane. The color only visualizes the heights to make it easier to see the shape.

To evaluate the 3D-shape the surface-to-volume ratio was calculated. For that a surface was fitted around the xyz -point cloud created from the previously fitted splines. The MATLAB function 'alphashape', provided a tool to fit a surface to the point clouds and did allow to measure the surface area and the volume. The surface-to-volume ratio covers 3D effects and is in particular relevant for the estimation of the mass transfer from the bubble into the liquid medium. With a spectral analysis of the surface-to-volume ratio a range for the two dominant frequencies can be determined. An example of the energy spectra, calculated with the Welch's estimation is shown in Fig. 4.7. With this method, as it is implemented in MATLAB the energy density spectra reveal two dominant frequencies f_R and f_S . However, since some of the measurements, especially the free rising bubbles are rather short in signal length due to the short measurement time the energy spectra are noisy. From a single measurement the calculated range is rather big, so the mean over several spectra of different bubble measurements is used to narrow the frequency band.

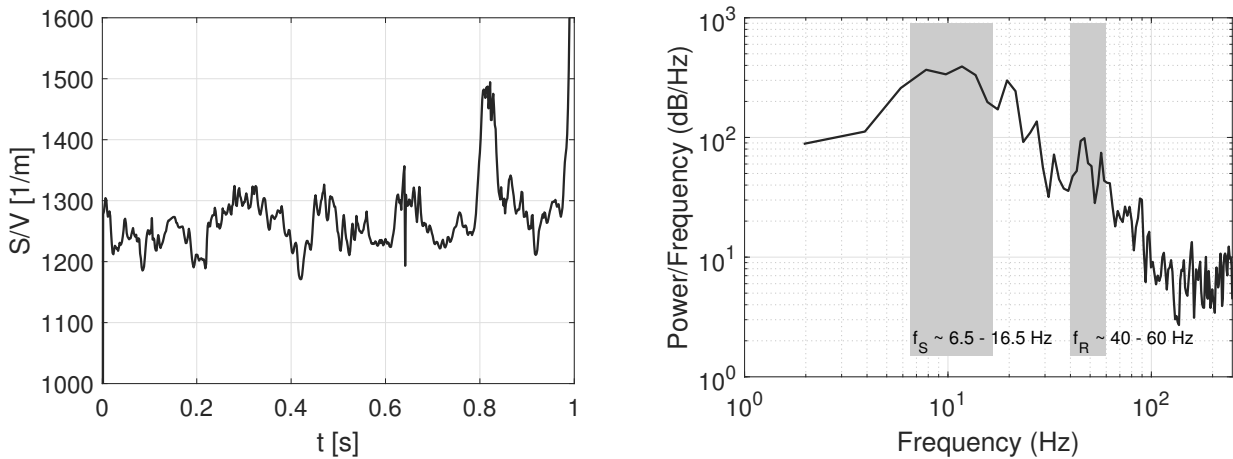


Figure 4.7: Evaluation of the surface-to-volume ratio. On the left the surface-to-volume ratio is plotted over time. To the right is the according energy spectrum. From that the two dominant frequencies are determined.

Thanks to the 3D reconstruction, it is possible to investigate the surface-to-volume ratio in order to gain a better understanding of the complexity of the 3D bubble deformation. Again similar to the 2D-method the data shall not be evaluated here but in the later chapter of [Cha. 5](#) and [Cha. 6](#).

4.4 Sensitivity analysis

To estimate the error introduced by the 3D reconstruction first the error that are made with the 2D approach shall be discussed. To simplify the first case a perfect circle or sphere is assumed.

In various publications [Veldhuis \(2007\)](#) or [Brücker \(1999\)](#) the volume or shape of the bubble was estimated from two 2D images. This can be visualized similar to the here described algorithm, just with two cameras, from the first image a cut through the bubble is made, that is then projected in the second image. From the length of both lines a bounding box can be made. With a circular fit in this bounding box, the bubble is then similarly stacked up. Is the bubble or the bubble slice a perfect circles the fit yields an errorless result. However, to make an accurate allocation between the two images, the bubble images in both cameras need to have the same resolution to have a nearly identical number of pixels rows, otherwise an unknown error is introduced. However, both approaches have another disadvantage. The correct bubble form can only be reconstructed, when the bubble is rising perpendicular to the camera planes, if it is tilted or angled to the camera the 2D approach reconstructs a false image. This is easily avoided with the 3D reconstruction. A sketch to visualize this is shown in [Fig. 4.8](#).

The error can be estimated with a few assumptions, first, that the calibration is without error, the bubble is perfectly circular or spherical. With two cameras the line of sight encases a square, with three a hexagon and with three an octagon and so on. Since the circle creates an inner circle for all figures the area of all the shapes can easily be calculated. So, with four cameras the error would be 5%. By a simple illustration in [Fig. 4.9](#) this can be visualized, making the given 5% the biggest error. If the estimation is done in a three-dimensional space the calculation gets more complicated.

Is the approach taken by either [Brücker \(1999\)](#) or [Veldhuis \(2007\)](#) with either the stacking approach or calculation of the two-mayor axis (which in essence is an intersection of the two line of sight cylinders) an error of roughly 27% can be estimated. This was calculated by comparing the volume that the intersection of two

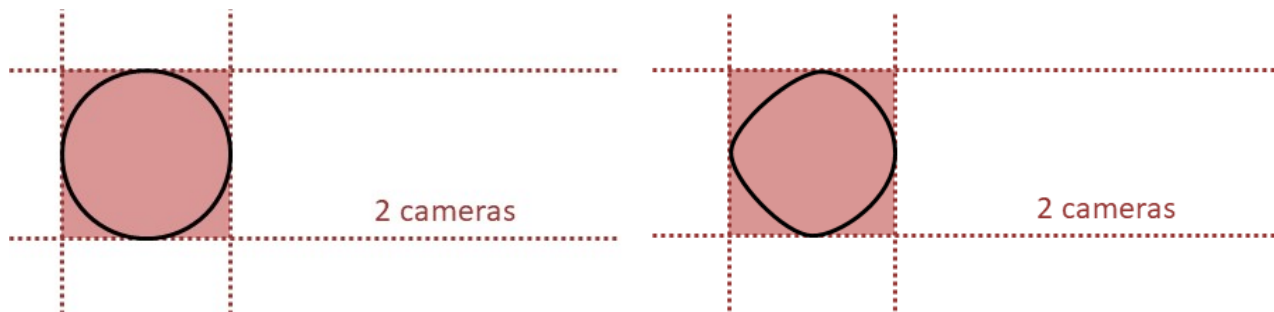


Figure 4.8: Sketch of the reconstruction principle with a perfect circle (right) and a deformed shape (left). If only 2 cameras or views are used to reconstruct the shape, Information is lost as can be seen when comparing the right and left black line.

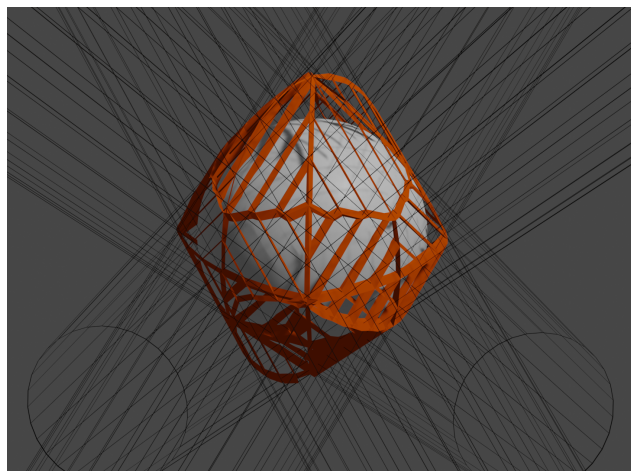
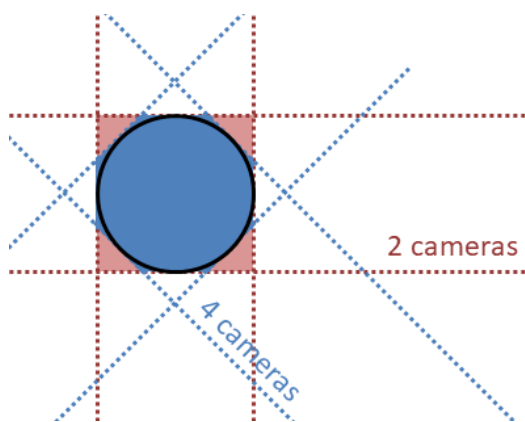


Figure 4.9: Sketch of the 2D (left) and 3D (right) reconstruction principle. If four cameras are used even in 2D the shape can be approximated better than with only 2 cameras. In the right image gray lines indicate the line-of-sights of the individual characters that are intersected in space. The Boolean intersection of those lines is marked with the orange shape. The white sphere in the middle is the desired bubble.

cylinders encasing a circle would yield and the real volume of the sphere. The same was done for the four-camera reconstruction. The reconstruction was simulated with a perfect sphere. By comparing the two volumes an error of 11% was calculated. A rendering of the 3D simulation is shown in [Fig. 4.9](#). The gray lines symbolize the line of sights of each camera and the orange wireframe the intersection of said line of sights. The solid sphere is the ideal body that is supposed to be reconstructed.

Since real bubbles are not perfectly spherical but rather elliptical, the error is smaller, since the circle is the extreme form of the ellipses. But then again, the errors that are made by the mask, the calibration and the reconstruction add up to the final error. Like stated above the error made with the mask can be neglected or be estimated to be less than 1%. The error of the calibration or rms value of the calibration can be recursively improved to a value below 0.01, so also below 1%. Therefore, the biggest error that is made is a systematical error by the nature of the reconstruction. However, with the 3D reconstruction bubble shapes can be reconstructed that would otherwise with the 2D approach not be possible or only if the bubble is oriented correctly.

4.5 Conclusions

The shape of a bubble, even smaller bubbles is a complex 3D mechanism. By evaluating only, the 2D information taken from single binary images and by using a not appropriate fitting method information is lost with these measurement techniques and evaluation methods. As shown by focusing only on the first mode of the Fourier descriptor or just an elliptical 2D fit, the higher modes are neglected. As can be seen later in [Cha. 5](#) and [Cha. 6](#) that neglecting these higher modes result, especially for bubbles with a higher radius in not correct values.

With the provided method an extension of this evaluation is proposed. It is also an easy and simple to use technique that truthfully reconstruct the 3D shape of a bubble. Even though highspeed cameras were used in this setup also low speed cameras up to 500 Hz can be used also making it more accessible. Depending on the accessibility of the measurement facility three cameras would already suffice to fully reconstruct the bubble, as long as it does not show convex surfaces. Four cameras have been used in this setup due to the construction of the channel. The best way to improve on this method is the placement of the cameras. While four cameras already generate a satisfactory image with the addition of more cameras Depending on the number of cameras used the reconstruction can be further improved. With an estimation the error can be calculated to around 11% compared to the 27% that are made with the 2D approach. Furthermore, for example the artifacts on the poles could be eliminated by adding an additional camera that records the bubbles from the front in between the two other cameras the artifacts could be drastically reduced and the reconstruction even improved further. This would lower the error to around 2% of the actual bubble volume.

One drawback of this method however is that, the algorithm can only reconstruct concave surfaces. These are hidden, due to the shadowing of the outer bubble parts. But neither the 2D nor the 3D method would be able to recreate or measure these. If concave surfaces are desired to be measured, tracer particles would need to be applied to the surface of the bubble. This however provides different challenges. For once these particles influence the surface of the bubble and alter the surface tension. Secondly due to the flow in and on the surface of the bubble they are moving on the surface, making it not clear if the surface itself or the particle is moving.

The error that is introduced due to the reconstruction was estimated to roughly 5 % of the desired reconstruction volume. This error is however a statistical error and can be taken into account in future evaluations. In conclusion the 3D MLOS reconstruction provides an excellent tool to describe the shape and allows for the characterization of it.

5 Behavior of a free rising single bubbles

5.1 Introduction

Bubble swarms are a complex problem with interactions of the flow and the bubbles. To break down this problem in smaller aspects, a single bubble in a quiescent water is analyzed first for comparison with the literature. A lot of different publications have been made about this topic, including [Clift et al. \(1978\)](#), [Veldhuis et al. \(2008\)](#), [Brücker \(1999\)](#). It is necessary to describe and understand the hydrodynamics of a single bubble in all its aspects. This chapter shows methods to measure the path, deformation and the wake of a single bubble rising in stagnant water. Additionally, this chapter utilizes the new 3D reconstruction to measure the oscillations and the wake structures behind the bubbles. To begin this chapter the experimental setup is outlined followed by the results and a detailed discussion. Parts of this chapter and some figures are published with permission in [Schlüter et al. \(2021\)](#).

5.2 Experimental Setup

To characterize the shape of the bubble and the flow around it two different experimental setups were used. The movement of a free rising bubble was recorded with a 2D stereoscopic camera setup, so that the 3D position can easily be triangulated. Since the bubbles motion is not fast, with a mean rising velocity of 320 mm/s it would be sufficient to use low speed cameras. In contrast to the stereoscopic setup the oscillations occur in a higher frequency and can only be resolved with a higher framerate. As stated in [Cha. 1](#) the maximum frequency of the shape oscillation that can be expected is 300 Hz. To resolve these oscillations a minimum recording frequency of 600 Hz is needed. Since the setups are quite similar to each other and were adjusted between the two measurements highspeed cameras (pco.dimax S4 from PCO) are used for both the path, the oscillation and 3D shape measurements. For the second measurement the 2D setup was expanded with two additional cameras to create a tomographic setup. With the tomographic setup a full 3D reconstruction of the flow and the shape can be measured simultaneously. With the algorithm described in [Cha. 4](#) the volume and surface of bubbles can be accurately reconstructed from shadow images. Those are images with a high contrast between the bubble and the background. An ideal image just shows the bubble as a darkened shape. To increase the contrast background LED (CCS TH2 from Stemmer Imaging in combination with a GARDASOFT RT220-20 controller to trigger the LED lights) are installed on the opposite side of the channel and cameras. The 3D flow was measured with a standard tomographic PTV setup as described in [Elsinga et al. \(2006\)](#). Schematics of both setups can be found in [Fig. 5.1](#) and [Fig. 4.1](#). As tracer particles fluorescent (~566 nm) rhodamine B particles from Dantec Dynamics are dissolved in the channel. These particles prevent a strong reflection of the laser light from the bubble on the camera. Due to the different refractive index of the water and the air in the bubble, the laser gets strongly diffused and the cameras would record a bright glare. With corresponding filters (Notch filter 532nm from Thorlabs) on the cameras, the green laser light is filtered so only the fluorescent rhodamine B is visible to the cameras. This however has the downside that the intensity of the PIV tracer particle is greatly reduced since the fluorescence efficiency cannot be increased with a higher laser intensity as it would be possible with glass beads. Thus, the measurement volume has to be chosen smaller to decrease the path the light has to travel and to increase the particle density on the recorded image. With an average particle density of 0.05 particle per pixel the density is not high enough to calculate accurate PIV images, especially in 3D the correlation peaks would not be sufficiently high.

So, particle tracking was utilized to calculate the paths of the tracer particles to measure the flow.

To correlate the shape oscillations with the flow field however the two images need to be recorded simultaneously in time, but on separate cameras to increase the quality of the images. This would require to measure each phase with an individual camera totaling the needed number of cameras to eight. Four for the flow and another set of four for the bubble shape. By separating the two aspects the shape of the bubble can be reconstructed with a higher accuracy, since a high contrast image is easily segmented into bubble and background. This however would make it impossible to measure the flow and the PTV tracer particle. This applies also vice versa, if the particle images are of high quality the shape of the bubble cannot be recorded. This is due to the amount of cameras and the necessary adjustments not feasible, thus the separation was made by alternating the recorded phase. So, the shape oscillations can solely be recorded with the shadow images of the bubble and the flow field with PTV. To separate these two, the particle image and the shadow image were recorded alternately, separated by a phase shift. First the Davis Software would trigger the laser to record one particle image and in the next timestep the LEDs to record a shadow image. The total recording rate was 1.2 kHz, which results in a recording rate of 0.6 kHz for each the particle- and shadow images. The limiting factor in this setup are the LED lamps. When they are triggered with a higher rate than 1 kHz the intensity decreases. However, a framerate of 0.6 kHz would already be sufficient to resolve the desired oscillation and path movements. Thus, with this setup the shape oscillation and the flow around the bubble can be measured simultaneously. Since the MLOS algorithm works best for a small measurement volume this has to be chosen as small as possible. Since the bubbles are freely moving over the channel it is not possible to predict the actual position, thus a rather big volume is desired on the other hand. To accommodate both restrictions a $20 \times 20 \times 20 \text{ mm}^3$ volume was chosen. This volume was placed in the middle of the glass channel to avoid wall interactions.

The bubbles were rising in quiescent water inside the measurement section of the counter flow channel. The bubble generator was placed 500 mm above the outlet of the water channel, 400 mm away from the desired measurement point. Two bubble sizes, ranging from 4 and 4.5 mm with several individual bubbles are recorded and evaluated. For the rising path also bigger bubbles up to 10 mm were recorded and evaluated. The cameras were mounted close to the top of the channel to ensure a sufficient time for the bubble to rise in order to establish its path. First the path was measured so both cameras were looking perpendicular through the glass. Therefore, no distortion due to the refractive index is to be expected. Secondly the flow around the bubble was measured with the four-camera setup, where all four cameras are looking under a 45° angle through the glass. This increases the reconstruction quality and minimizes the error. This however introduces an error due to the refractive index with the glass and water. To correct this, the cameras are looking through prisms filled with water. Specially designed prisms with an angle of 45 degrees are attached to the glass walls of the channel. Additionally, scheinplugg adapters are mounted on the cameras, with a maximum angle, to allow the cameras to be focused on the whole measurement and reconstruction plane, which is perpendicular to the channel walls.

One additional setup was used in a collaboration with the Chemical department at the LMU and Prof. Klüfers to visualize the wake structures with a chemical tracer. For this three highspeed cameras were installed like seen in [Fig. 5.3](#). This setup was chosen to focus on the wake structure behind the bubble, the cameras are again the pco highspeed cameras. The chemical tracer system was used to visualize the wake. The chemical system was originally designed to visualize the mass transport from the bubbles interface in the liquid ([Aas & Klüfers 2017](#)). For this Iron(II) sulfate heptahydrate, Sodium hydroxide and N-(2-Hydroxyethyl) ethylenediamine -N,N,N'-triacetic acid is dissolved in the liquid to invoke a chemical reaction, if it comes in contact with oxygen. For this, nitric oxide-bubbles (NO-bubble) were created with a capillary and a gastight syringe. When the oxygen in the bubble is moving through the bubbles surface into the continuous phase, it is bound to the iron in the liquid, which causes a visual darkening that can be detected with the cameras. A slightly different setup was used, as can be seen in [Fig. 5.3](#). This was done to increase the accuracy of the reconstruction in the wake area. By placing three cameras at the bottom a higher resolution can be achieved when reconstructing the wake.

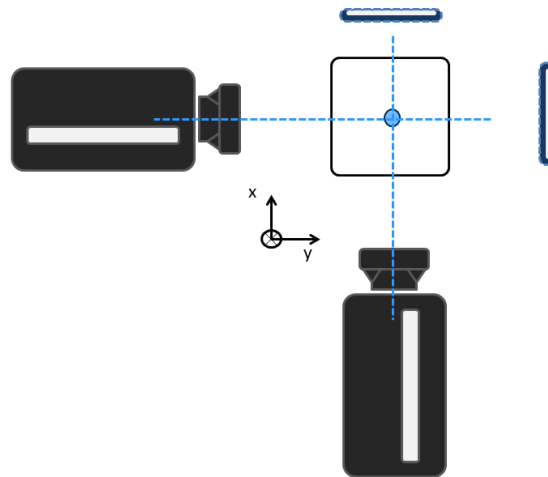


Figure 5.1: Sketch of the camera setup. Two cameras are positioned in a 90-degree angle to each other and look straight through the channel glass, so no reflective index matching is necessary. To enhance the contrast on the shadow images background LEDs were installed. They were triggered to the camera images to get higher intensities.

5.3 Results and discussions

5.3.1 Rising path in quiescent water

As described in [Cha. 1](#) bubbles describe different path depending on their size. While small bubbles up to 3 mm tend to rise in a spiraling motion, the medium sized bubbles (3-5 mm) do a zigzagging motion. Above that size the surface of the bubble gets strongly deformed and the bubbles describe a chaotic path. Some examples can be found in [Fig. 5.2](#). It can be seen that with increasing size the ellipse/zigzag motion becomes less defined. To no surprise the same results, as expected from the literature can also be measured with this setup. It should be noted that, the path is partially influenced by the sphere grid that were present in the channel.

The grids are only moved by bubbles passing by it at a previous time, consequently the excitation of the grids is only minimal, however the presence of those fluctuation can be measured in the bubble patch. Especially the small and medium bubbles are easily diverted from their path. This can be seen in the top left image of [Fig. 5.2](#). While the bubbles follow the zigzagging motion, at the top they tend sometimes deviate from this path. The biggest bubbles, in this case bubbles up to 10 mm still describe a rather chaotic spiraling motion. This shows that even the smallest disturbances, cause the bubbles to alter their path. So, it is understandable that already small fluctuations influence the bubbles path. If the grid is not present or the measurement is done sufficiently far away, the bubbles show their expected spiraling and zigzagging motion.

5.3.2 Deformation of the surface

The shape of a bubble fluctuates in response to oscillations in the pressure field in the liquid surrounding the bubble. The intermittent vortex shedding associated with the lateral motion of bubbles, see, e.g., [De Vries \(2001\)](#), will cause regular fluctuations in the velocity and therefore in the pressure field around the bubble. In their review on bubble wakes, [Fan & Tsuchiya \(1990\)](#) refer to several instances where the shape of (mainly large) bubbles was observed to oscillate at the frequency of the lateral motion. It is evident that the fluctuating shape of the bubble is a result of the turbulent shear and pressure forces of the surrounding liquid. In addition to that,

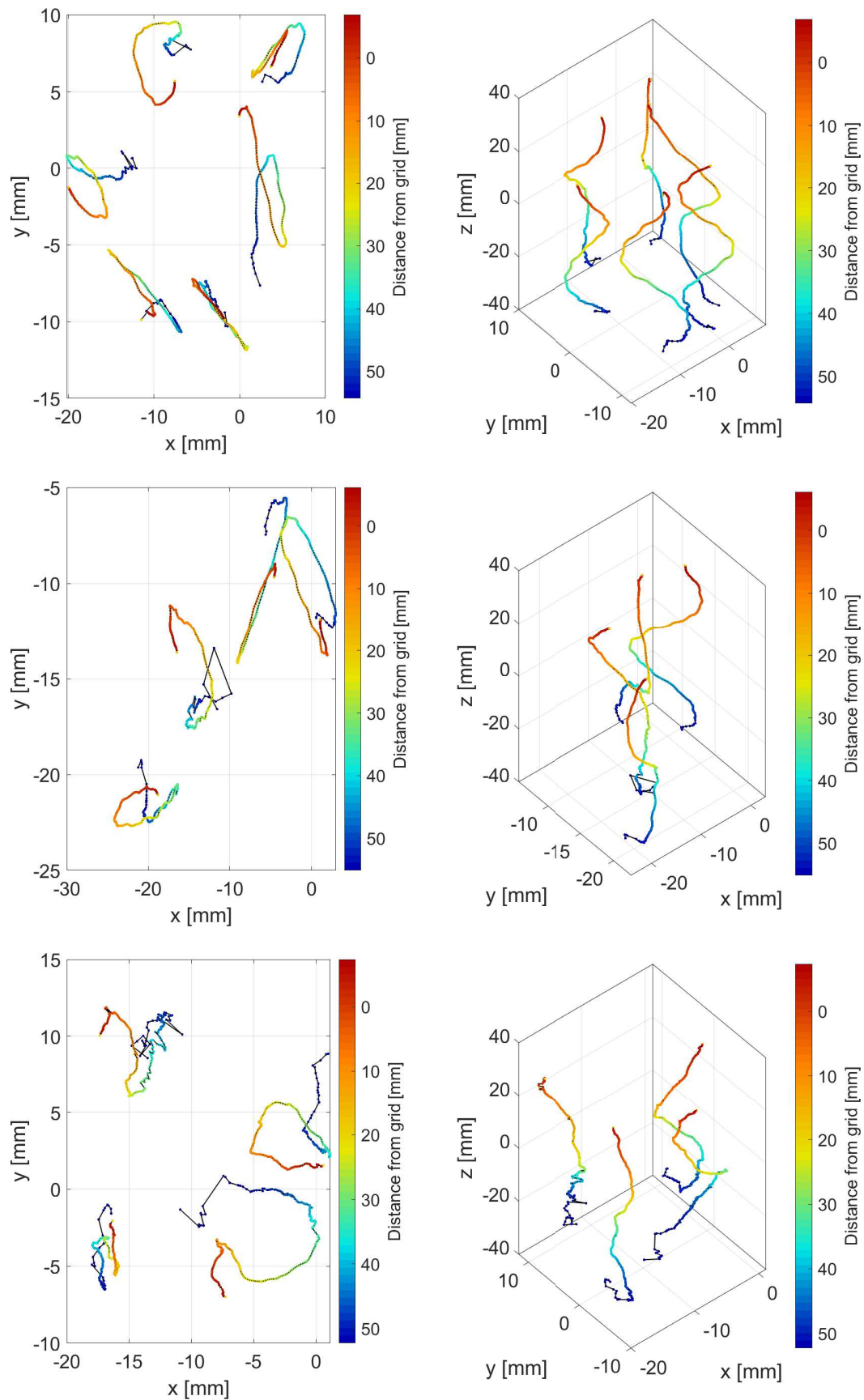


Figure 5.2: Comparison of different bubble path depending on the size. From top to bottom the bubble size is increasing. The smallest bubbles had a size of 1-3 mm. The medium sized bubbles were around 3-7 mm. While the biggest one was 7-10 mm in diameter. The left column shows a top to bottom view, on the right-hand side a perspective view.

the coupled vortex shedding behind a rising bubbles leads to lateral motion of the bubbles, inducing drag and lift forces on the bubbles. The oscillations frequencies for small bubbles with a diameter up to 2–5 mm are well reported in the literature, but the deformation dynamics of larger bubbles is less well documented, see [Lunde & Perkins \(1998\)](#) or [de Vries et al. \(2002\)](#). Bubbles with a larger diameter become unstable and start to deform in such a manner that it is more difficult to measure or simulate their dynamics and surface motion.

To describe these oscillations, two different modes are discussed in the literature: the oscillations in the equivalent major axis e , named mode 2,0 and of that in the axes ratio R , as mode 2,2. In [Lunde & Perkins \(1998\)](#), a simple model is described linking the shape oscillations to capillary waves traveling on the bubble surface. The 2,0 waves are moving from the front to the rear stagnation points (from pole the pole), and mode 2,2 waves are traveling around the equator of the bubbles. In [Fig. 1.5](#) a sketch visualizing the two modes is shown. It is further described in [Lunde & Perkins \(1998\)](#) that the modes correlate with the bubble volume and deformation. It is also noted that the 2,0 mode has a strong correlation with the motion of the bubble itself. The 2,2 mode however does not show any relation to the bubble motion.

The frequencies of the oscillations can be formulated in terms of the spherical equivalent diameter and the ellipticity ϵ . In this formula σ the surface tension, and ρ the density of the liquid. The mode 2,0 and 2,2 frequencies can be calculated according to [Lunde & Perkins \(1998\)](#) as follows:

$$f_{2,0} = \frac{1}{2\pi} \sqrt{\frac{16\sqrt{2}\epsilon^2\sigma}{\rho_L(\epsilon^2+1)^{3/2}r_\epsilon^3}} \quad (5.1)$$

$$f_{2,2} = \frac{1}{2\pi} \sqrt{\frac{8\sigma}{\rho_L\epsilon r_\epsilon^3}} \quad (5.2)$$

With the in [Cha. 4](#) introduced measurement technique, the oscillation behavior was studied in more detail. With both approaches (2D and 3D) different sizes are evaluated and presented in [Tab. 6.2](#). The 2D measurement shows values in the range that are also reported by [Lunde & Perkins \(1998\)](#). Unlike Perkins, that used the Fourier descriptors in this evaluation a ellipses was fitted around the bubble to measure the two frequencies $f_{2,0}$ and $f_{2,2}$. With a spectral analysis the modes were then extracted from the signal. These are written in [Tab. 6.2](#). It is easy to see that the 2D evaluation yields the same results as the literature values. The small discrepancies arise from the different qualities of the water that were used. As stated before, surfactants show a significant influence on the behavior. Even small amounts of surfactants influence the behavior of the bubble greatly ([Takagi & Matsumoto 2011](#)). But nevertheless, all values are in good agreement, within an uncertainty of 5%.

On the contrast however from the 3D data the frequencies f_R and f_S are measured. From the spectral analysis of the surface-to-volume ratio the frequencies can be identified. With the following correlation the two sets can be calculated into each other: $f_R = (f_{2,0} + f_{2,2})/2$ and $f_S = |f_{2,0} - f_{2,2}|/2$. Since a bubble was only a short time in the measurement volume the recorded signal is not long enough for a reliable Fourier transformation. Thus, three bubbles with a similar radius were evaluated and a mean range for the frequencies calculated. Again the data is written in [Tab. 6.2](#). Here the oscillation frequencies are increased by almost a factor of three, from the expected ones and the one yielded by the 2D data. This can especially be seen in the measurement with 4 mm bubbles that are moving freely. This clearly shows that even for smaller bubbles a 2D evaluation is not sufficient to fully describe the shape oscillations with the simple approach of 2D elliptical fitting. The 3D method clearly indicates that the two modes $f_{2,0}$ and $f_{2,2}$ superimpose on each other and create a complex oscillating motion and the resulting frequencies vary in the 3D and 2D approach. Suggesting, that the bubble oscillation even for smaller bubbles is already a 3D phenomenon. From publications from [Brücker \(1999\)](#) it is known that a spiraling motion as a frequency of 5.8 Hz. In addition [Lunde & Perkins \(1998\)](#) correlate the 2,0 mode with the oscillation of the bubble. For both bubbles the 4.0 and 5.0 mm bubbles the data from the 2D evaluation does not match the data that was measured by [Brücker \(1999\)](#) deviating by a factor of 4.8. Are however the two frequencies used to calculate the frequencies f_R and f_S . The range of the to be expected data is reached. Again, suggesting that

surface-to-volume approach delivers the desired results. However the measured 3D data is unfortunately on in range of the in the literature presented data, this is mostly due to the sparse data that was available due to the short time the bubble was in the measurement volume, can this be improved upon, for example with a camera system that is moving with the bubble better data can give more insight into this topic. Nevertheless, it was shown that even for smaller bubbles a 3D approach is necessary to understand the shape oscillations.

d_b (mm)	$f_{2,0}$ (Hz)	$f_{2,2}$ (Hz)	f_R (Hz)	f_S (Hz)
literature/theoretical				
4.0	41	28		
5.0	28	20		
experimental 2D				
4.0	37-47	24-34	30-40	~6
4.5	20-30	18-28	19-29	~1
experimental 3D				
4.0	108-128	~72	90-100	18-28
4.5	98-118	~68	83-93	15-25

Table 5.1: Comparison of the different frequencies from the reconstruction (exp.), and theoretical calculation taken from literature [de Vries et al. \(2002\)](#).

5.3.3 Wake structures

The wakes of free rising bubbles are direct result of the size of the bubble. The size of the bubble determines the path, which in contrast determines the wake structures. A detailed explanation is given in [Cha. 1](#) and can also be read upon in various publications like [Brücker \(1999\)](#). So far however only 2D measurements of the wake have been performed and extrapolated. Brücker for example measured the wake in a fixed plane and used a spatial temporal reconstruction to gain a three-dimensional view of the wake. This gives a great insight in the nature of the vortices, but it cannot resolve three dimensional or out of plane effects especially time dependent or short events. In this experiment a three-camera setup was installed around the measurement test section. A schematic drawing is shown in [Fig. 5.3](#). As describe in previous sections to visualize the wake of a free rising bubble a chemical tracer ([Aas & Klüfers 2017](#)) was used to colorize the wake. Similar to Brückers experiment the color tracer gets trapped in the vortex cores.

Similar to the shadow images of the regular bubbles the wakes are clearly visible in the shadow images ([Fig. 5.3](#) right image). A full motion of a spiraling bubble is shown in [Fig. 5.4](#). The wake and it's evolution is depicted. While the bubble is still rising in a straight path after detaching from the capillary a cone like shape is observable until, the path changes and the bubble goes into a zigzagging motion ([Fig. 5.4](#) $t = 0 - 0.026$ s). Two trails start to form behind the bubble as seen in ([Fig. 5.4](#) $t = 0.026 - 0.053$ s). These tails grow in length until the bubble changes it's direction and the ends start to diffuse ([Fig. 5.4](#) $t = 0.07$ s). After the change in curvature, the two trails begin to reform until the next change occurs ([Fig. 5.4](#) $t = 0.07$ s - 0.1 s). As can be seen the bubbles create a wake and the vortices stay stationary.

The free rising bubble and the visualization of the mass transport revealed that the gas is transported through and along the interface, to the rear end of the bubble and gets trapped in the hairpin vortices until those start to decay and diffuse. The wake of spiraling and zigzagging bubbles are similar to each other; however, the wake of a zigzagging bubbles exist on a shorter timescale. The spiraling wake persist roughly 2 seconds longer

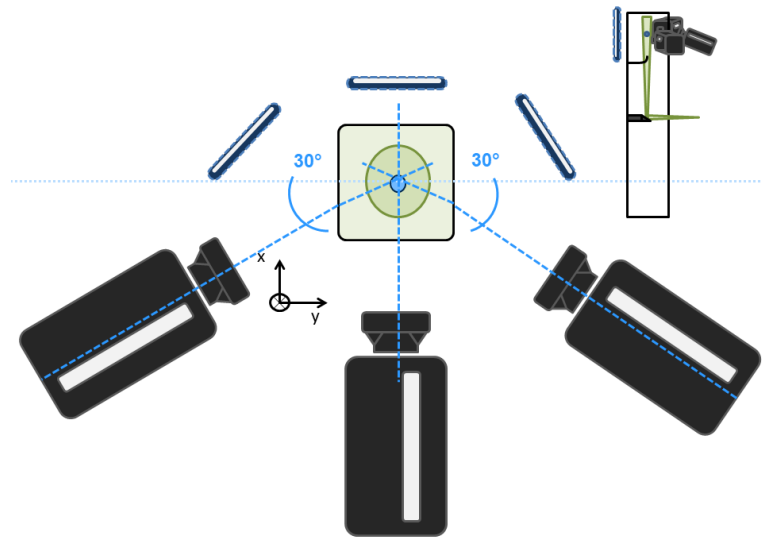


Figure 5.3: Schematic tomographic camera setup with triggered background light. For the visualization of the wake, background LEDs were setup to enhance the contrast and create shadow images. Snapshot of a colored wake structures behind a free rising NO bubble.

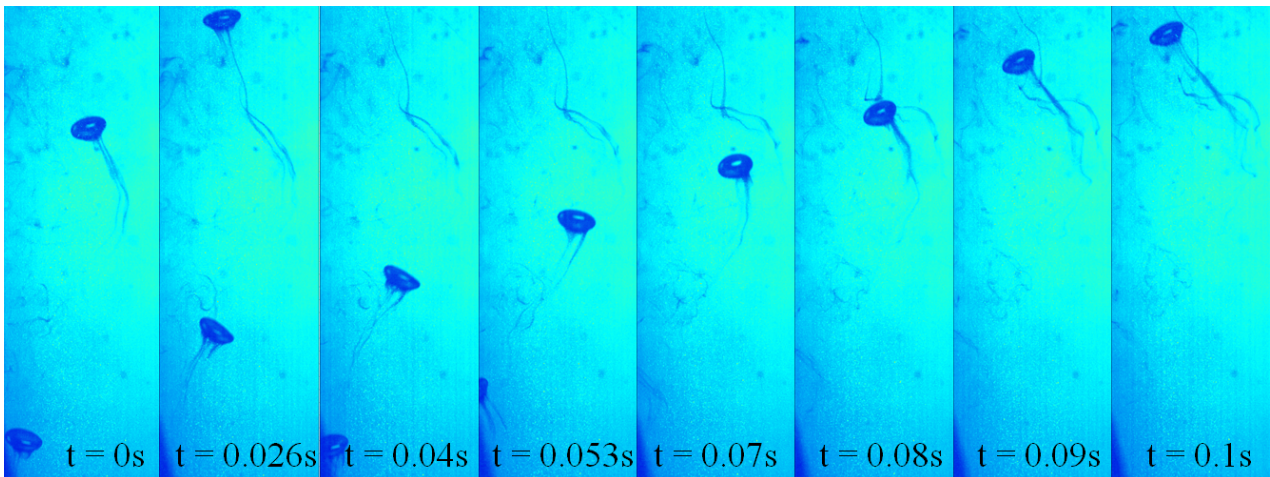


Figure 5.4: Different time steps of a free rising bubble with colored vortex trails. Through the chemical reaction of the NO gas and the iron in the solution a substance is formed that darkens the solution. The chemical reaction takes place on the surface of the bubble as soon as the gas diffuses through the interface. The product is then transported along the surface channel and gets trapped in the vortices behind the bubble.

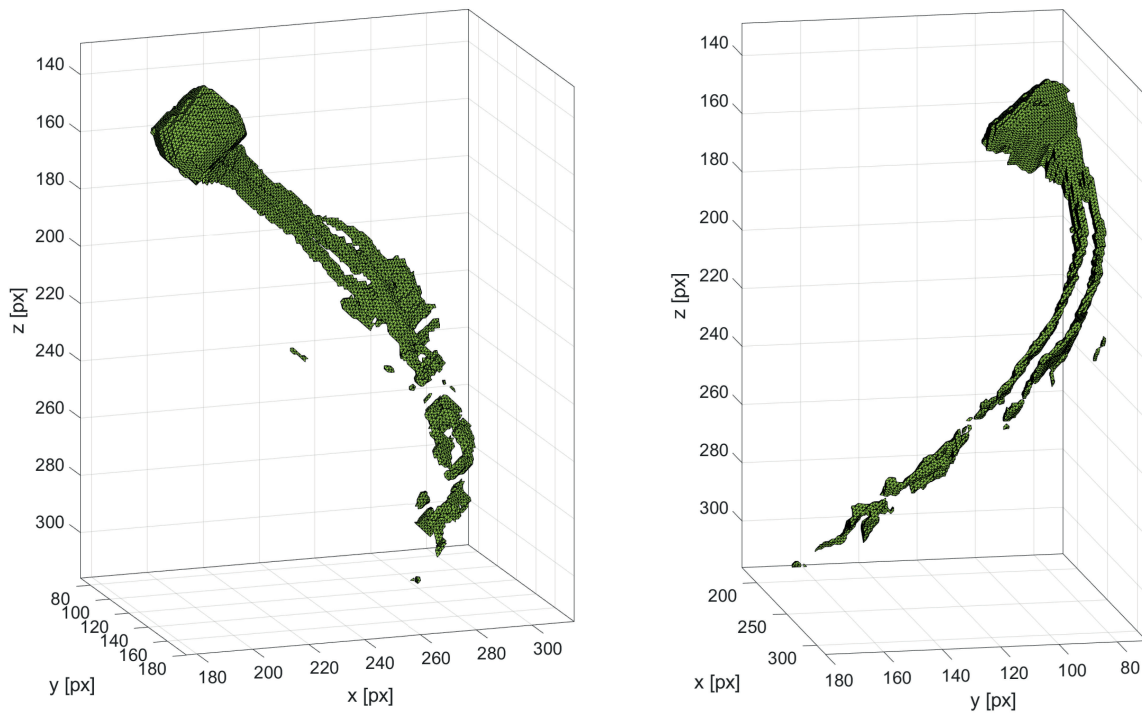


Figure 5.5: One time step of a freely rising NO-bubble in the FeEDTA solution. The reconstruction was done analog to the one in [Cha. 4](#). The two wakes behind the bubble are clearly visible and the wake diffuses roughly 3 bubble diameters behind the bubble. Both images show the bubble from different angles.

than the zigzagging one. This phenomena was already described in [Abdulmouti \(2014\)](#) and [Veldhuis \(2007\)](#). Before they dissolve, the two separate legs undergo so called Crow instabilities ([Crow 1970](#)). The instabilities are triggered by small perturbations, like the reconnection of the vortex legs. This occurs closer to the bubble for a zigzagging path and since the wake of spiraling bubble is more stable the instability occurs about 300 bubble diameters behind the bubble ([Abdulmouti 2014](#)). In [Fig. 5.6](#) a example as it was observed with the chemical system. Analog to the shape of the bubble the wake can also be reconstructed with the shadow images. An example is shown in [Fig. 5.5](#). However, in the shadow images it was complicated to separate the wake from the background due to residue of older bubble wakes and a general darker image due to the chemical tracer. This makes the reconstruction of smaller structures, especially at the end of the wake error-prone and are often not reconstructed, since the separation algorithm could not detect the smaller parts. Nevertheless [Fig. 5.5](#) shows not only the capability of the algorithm but also shows the stability of the wake and the length and size. The wake pair behind the bubble is well defined 3-4 bubble diameter behind the bubble and then starts to diffuse into the surrounding liquid, similar to the two dimensional analysis above and [Fig. 5.4](#). This can be especially seen in the right image. While a small portion of the chemical is trapped half a bubble diameter behind the bubble in the immediate wake, the chemical gets then transported through the wakes core downstream away from the bubbles. Even the crow instabilities can be seen at the bottom of the wake. Even though this gives great insight into the overall structure of the bubbles wake a more in-depth analysis can be made by measuring the flow statistics in the bubbles wakes with other measurement tools.

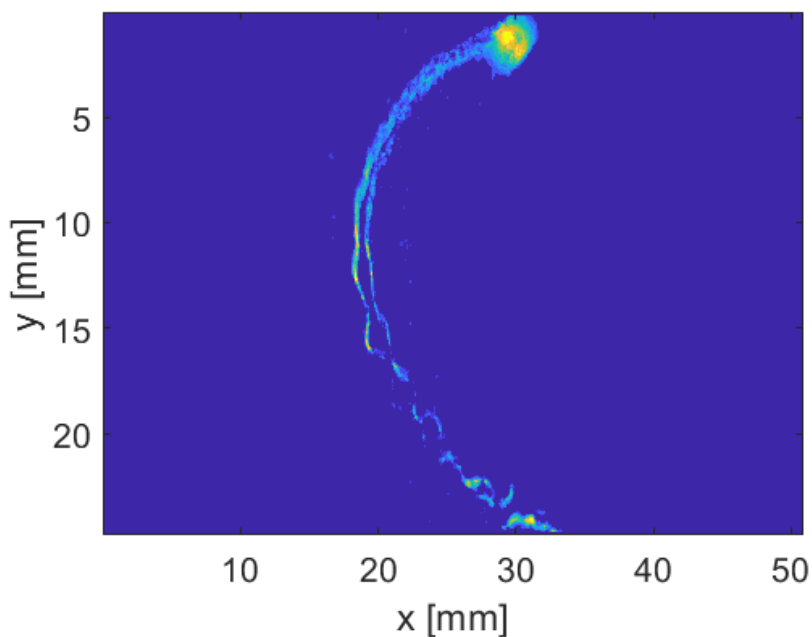


Figure 5.6: Visualization of the crow instabilities behind a zigzagging bubble. To enhance the image and increase the visibility of the instabilities the mean value over 10 images was taken.

To measure the flow structures in the wake and to improve on the spatial reconstruction an additional camera was setup to allow for a better reconstruction of the particle tracks. With the standard MLOS algorithm the particle tracks were reconstructed and similar to [Brücker \(1999\)](#) a spatial temporal reconstruction was applied to the particle tracks [Fig. 5.7](#). This means that each time step was shifted with the position of the bubble, which keeps the bubble in a fixed coordinate system. The particles are color coded with their velocity and only the particles that are influenced by the bubbles are clearly marked. The others are made transparent. The particles

were chosen with a velocity threshold 30 mm/s. Particles below that are categorized as not influenced by the bubble.

Since the bubble only spends a short amount of time in the actual measurement volume a full spatial reconstruction is not possible. Making it only possible that the distance downstream (z -axis) is correlated to the bubble velocity. Thus, the wake seems to lose its spiraling motion, which is not true. Would the bubble position be known for every time step the full reconstruction of the spiraling motion could be made correctly. Therefore, only the length and width of the wake can be described with this evaluation. One other thing to note is that the algorithm only allowed particles that can be reconstructed from all four cameras. For this reason, the particle density close to the bubble is rather low. One drawback however is the low seeding density that prevents the measurements of exact values like the sheer or vortex strength of bubble wake, let alone the crow instabilities. But nevertheless, this measurement clearly shows the length of a bubble trail and the dimensions in the cross section. It becomes also visible that the length is up to 20 bubble diameters. Both vortex feet have roughly the same dimension as the bubble itself. Much in contrast to the chemical tracer visualization, that only showed the inner core parts. In the core regions the flow behind the bubble gets accelerated up to 100-125 mm/s while the whole wake itself is close to the rising velocity of the bubble with around 35 mm/s. This was also seen by Brücker in his 2D analysis (Brücker 1999). He measured a mean velocity of 130 mm/s for spiraling bubbles. Thus, this method proves to be accurate in regards of reconstructing the velocities in the bubbles wake.

5.4 Conclusion

To create a basis for first comparison for later experiments and to verify the measurement and evaluation techniques, free rising bubbles were investigated in regards to their undisturbed rising pattern, their surface oscillation and wake structures. With a simple two camera stereo setup the rising path was reconstructed and compared between different sizes. In this experiment spiraling, zigzagging and chaotic movement with increasing bubble diameter was measured. It was also seen that even small random disturbances in the flow, from a previous bubble, slightly exciting the particle grids, result in path alterations. Not only the path but also the surface was measured in 2D and 3D and from those the oscillation frequency of the surface with a) the 2D images and b) the 3D surface-to-volume-ratio. This gave insight that with increasing diameter a plane 2D evaluation of the diameter is not sufficient anymore to describe the bubble deformation. This makes a full 3D evaluation necessary to accurately describe the waves moving around the bubble surface. It was shown that bubbles with 4 mm diameter and above need to be described as a 3D object due to the increasingly complex surface shape. A novel 3D reconstruction method was introduced that allows describing bigger bubbles as long as they don't show concave surface elements. With increasing number of cameras this reconstruction can be further improved and the reconstruction errors minimized. Third the bubble wakes are visualized with the aid of a chemical tracer. The oxygen in the bubbles is bound to the iron complex in the fluid and darkens the water. These can be recorded on the shadow images. From the time resolved data it could be shown, that while a bubble is rising, the wakes develop depending on the position of the bubble in the path. Is the bubble rising the wakes start to grow. In the turning points however the feet of the wake close, the bubble turns and the closed structures stay stationary while the bubble is rising again and the wake starts to form again. In some of the images, especially in the first few spiraling turns, Crow instability can be seen as they dissolve the wake tails of the bubbles. They occur when small disturbances happen in the system, just like the closing of the vortex pairs. The MLOS reconstruction was used to create 3D images of the rising bubble and its wake structures. From a spatial temporal reconstruction, the overall shape and size of the bubble wakes can be estimated. A rather big measurement volume was chosen, because the bubble position varies over the channel cross section. Due to the rather big measurement volume the seeding density and by extension the density of the measurement points is rather low. However, the shape and size of the wakes can be estimated to be in the size of 2 bubble diameters and

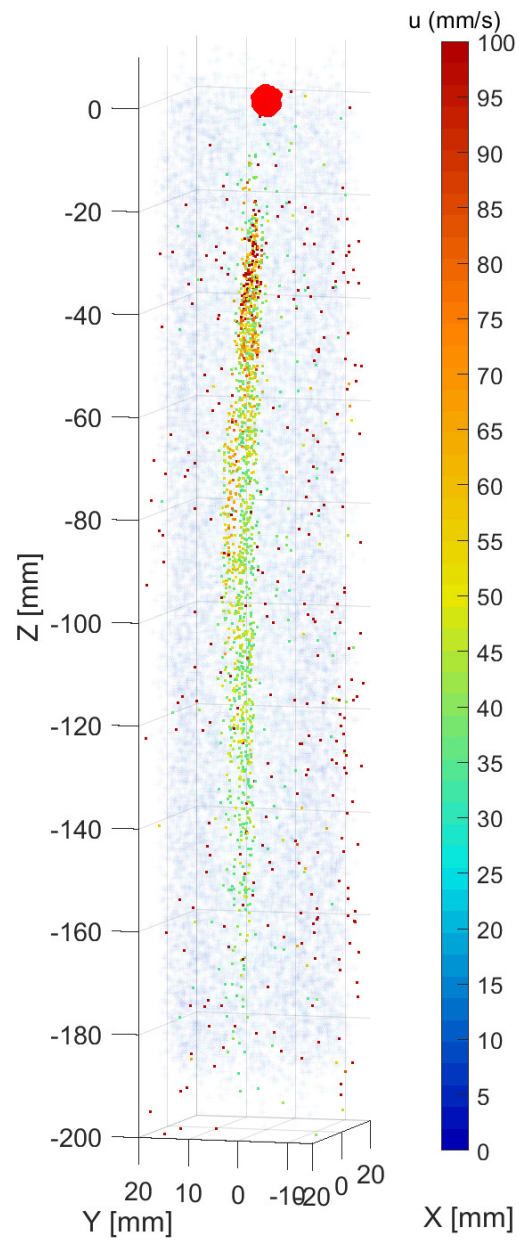


Figure 5.7: Spatial temporal reconstructed particle tracks. Each time step was spatially moved according to the bubble motion. The bubble motion is marked with black x. The reconstructed volume in each time step is shifted in x,y and z direction with the bubble path.

one wake vortices spans over the size of one bubble diameter. In addition, the separated and close structures stay stationary for roughly 20 bubble diameters before they diffuse. This shows that the chemical tracer is only trapped in the inner most regions and does not span over the whole vortex. In conclusion it can be said that with these methods a good variety of information regarding the shape, the path and the wake could be made. A new way of investigating the shape oscillation was introduced with the tomographic reconstruction. The chemical tracer allowed resolving the small structures in the lower wake region with a higher resolution, while the tomographic particle tracing gave insight into the bigger structures.

6 Behavior of a single bubble in swarm like background turbulence

6.1 Introduction

It is obvious that the transfer of chemicals from the bubbles in the liquid depends strongly on the flow state of the surrounding media (laminar/turbulent). But also, the size of the bubble is an important parameter since larger bubbles deform which results in a variation of the surface area and changes the transfer of chemicals through the interface. In order to better understand the procedure and its effects or individual mechanics, it is necessary to investigate the interactions between bubbles and the induced wake turbulence. Special value has to be placed on characteristic variables like the bubble size, gas volume fraction and liquid agitation and their influence on the mass transport from the bubbles in the surrounding fluid.

The, in [Cha. 3](#) introduced turbulence generating grids, were used to perform experiments to gain further insight in the movement and behavior of individual bubbles in a swarm. As a comparison and reference, free rising bubbles have been studied in [Cha. 5](#). This allows to make a correlation between the bubble shape, the wake's shape and the overall flow structures of a single bubble. In the following, the experimental setup is outlined with an explanation of the camera setup, a detailed description of the evaluation and reconstruction can be found in [Cha. 4](#). Parts of this chapter and some figures are published with permission in [Schlüter et al. \(2021\)](#).

6.2 Experimental Set-up

To understand the motion of the bubble and how it is influenced by the grid or the emulated bubble swarm, both the path of the bubble and the grid needs to be reconstructed. To record the movement of the bubbles in the turbulence the 3D path was recorded with a stereoscopic two camera set-up. In the first part only, the path is of importance, which makes two cameras sufficient to record the position of the bubbles. In [Fig. 5.1](#) a sketch of the experimental set-up is shown. Different bubble sizes, one smaller than the grid element one in the size of the grid element and one bigger were released in the counter-flow and recorded until the bubble moves either out of the camera view or gets transported into the channel wall boundary layers. With the counter-flow the rising of the bubble can be slowed down or even held in place. Thus between 1000 and 6000 images were recorded, which correlates to a recording times between 1 and 15 s that the bubble moves in the turbulence. To binarize the images with higher accuracy the cameras were again equipped with a LED background light, as already shown in [Cha. 5](#). Analog the same equipment as in [Cha. 5](#) was utilized for this experiment. The cameras were pco.dimax S4 from PCO and the background illumination were CCS TH2 from Stemmer Imaging in combination with a GARDASOFT RT220-20 controller to trigger the LED lights.

To correlate the bubbles position with the grid the grid elements are as well illuminated with the back light and with a circle finder algorithm detected. This circle finder was able to truthfully detect the position of the grid element even if the spheres overlap. It is to note however, that the correct triangulation of the 3D position is only possible for low density grids like the grids with 5% volume fraction. If the volume fraction is to high, like for the 10% grids the triangulation is not unambiguously anymore. From the binarized images of both cameras the position of the bubbles as well as the lowest grid elements are triangulated. From which the 3D position of

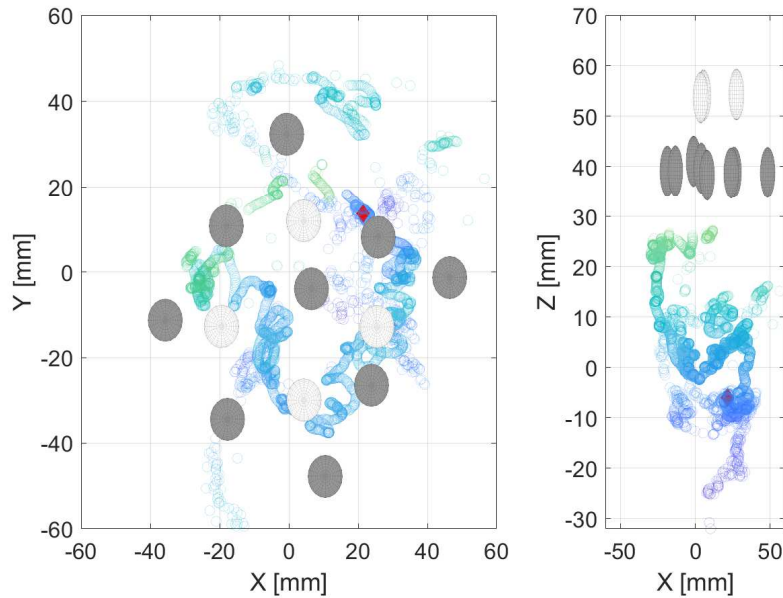


Figure 6.1: Example of a path and sphere position evaluation. Both the position of the two lowest grid layers as well as the bubble path is reconstructed. The path of the bubble over the whole measurement is printed in blue. The coloring denotes the distance to the grid. The red marker shows the current position in relation to the grid. The left image shows a top view, the right image a side view of the channel. Published in [Schlüter et al. \(2021\)](#) and reprinted with permission.

the bubble relative to the grid can be determined. In [Fig. 6.1](#) an example of the evaluation result is shown. For the shape oscillation and the wake structures the setup and evaluation as described in [Cha. 4](#) and [Cha. 5](#) was used.

6.3 Results of path measurements, oscillations and flow structures

6.3.1 Movement in emulated turbulence

At first the bubbles are slowly rising towards the grids. The bubbles are slowed down by the counter flow. It is noticeable that the bubbles still follow their original path pattern, even though it is sometimes contracted in z -direction, so that the distance between the spirals gets shorter until they experience a certain turbulence level. An example is shown in [Fig. 6.2](#). The z -position of the bubble is color coded to better visualize the path. With a certain threshold of background turbulence, the bubbles start either to contract their path even further in z -direction or the bubble starts to be moved by the surrounding turbulence, rather than its own motion. In some cases, the bubble even got moved downwards out of the measurement region again. It can be seen that there is a threshold around 15 % that the bubbles are influenced and it is assumed that depending on the size a different threshold is necessary, but the range seems to be narrower than what can be resolved in this measurement.

If the bubbles are now moving in the emulated turbulence the bubbles have a higher probability to stay in regions with lower turbulence/higher velocity such as between the grid elements ([Fig. 6.1](#)). Between the particles higher velocity fluctuations, both in flow direction and perpendicular to it, are present. This can be seen in the p.d.f.s in [Cha. 3](#). Depending on their initial position the bubbles move to the nearest position between the spheres or regions with high turbulence. When they pass underneath a sphere, they get accelerated towards the

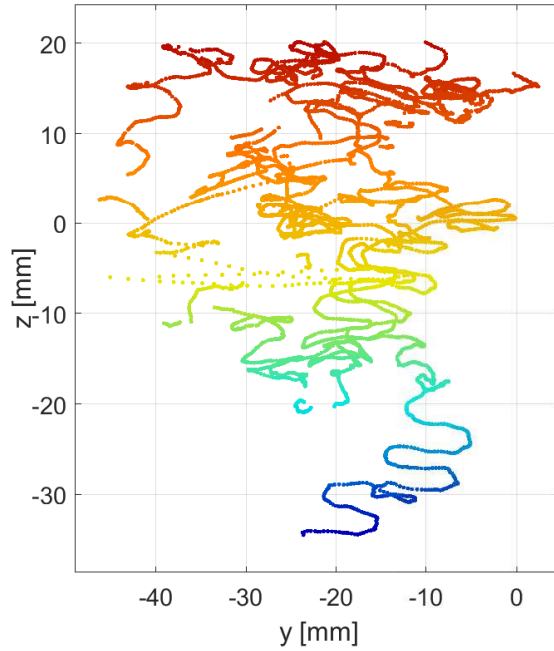


Figure 6.2: Example of a path and sphere position evaluation. The height of the bubble is color coded. the spheres of the grid are hanging at the top of the graph at around 20 mm. For this measurement a medium sized bubble and a turbulence grid with 10 mm sphere and a volume fraction of 5 % was used.

grid elements due to the slow wake behind a sphere. The spheres however are also moving. The lowest elements describe a circular motion and depending on the density of the grid the amplitude of that circle changes. For the low-density grids, the amplitude can be up to two particle diameters. It should be noted, that it takes some time for the wake to get transported from the grid element to the bubble. Usually the bubbles are about three sphere diameters downstream and with a counter flow velocity of 200 - 250 mm/s the fluctuations need 0.1 - 0.12 s to reach the bubble. With a recording rate of 600 frames per second the grid position 60 - 72 frames in the past needs to be used to compare the bubble and the grid position. Therefore, in the images shown in Fig. 6.1 the bubble position and the grid position 75 frames in the past is shown.

The bubble tends to stay longer at position in between the grid elements and move depending on their size only small distances. This can be explained by the velocity gradient that is induced by the slower wakes behind the grid elements. This velocity gradient in return creates pressure gradients that can be described by the Bernoulli equation.

$$p_t = p + \rho g z + \frac{\rho}{2} u^2 \quad (6.1)$$

The Bernoulli equation states that the dynamic pressure is proportional to the square of the velocity. In the measurements it is shown that small bubbles ($d_b < \text{sphere element}$) tend to follow this well. On the contrary, big bubbles are more deformable and experience a wider pressure gradient over the whole bubble volume and cannot settle in the small low-pressure regions between the grid particles like the small ones. The bubbles get instead more deformed and tend to follow the bigger or stronger structures. In a real bubble swarm, a single bubble is spatially restricted by the swarm, this stabilizes the path the bubble can take and is forced to rise in a confined space. When moving in a turbulent fluid by itself, the bubble seems to take the path of lowest turbulence and is not confined by the swarm, which results in a more random nature of the path movement.

gridelement	d_k [mm]	α_k [%]	F_D [N/m ³]	F_T [N/m ³]	F_R [N/m ³]
sphere	10	10	2.3	0.24	1.26
spheres	10	05	2.5	0.24	1.26
spheres	05	10	30.01	0.24	1.26
ellipses	05	03	5	0.24	1.26
ellipses	10	10	38.61	0.24	1.26

Table 6.1: Comparison of the different estimated forces resulting from the pressure F_D , the inertia F_T and the friction F_R . Listed are different grid compositions. The data is calculated for a 5 mm bubble and 3 sphere diameters behind the grids.

From the Navier-Stokes-Equation, dimensionless numbers and forces can be derived and used to estimate the effects that are dominant in this flow structure.

$$\rho \left(u \frac{\partial u}{\partial x} + v \frac{\partial u}{\partial y} + w \frac{\partial u}{\partial z} \right) = -\frac{\partial p}{\partial x} + \eta \left(\frac{\partial^2 u}{\partial x^2} + \frac{\partial^2 u}{\partial y^2} + \frac{\partial^2 u}{\partial z^2} \right) \quad (6.2)$$

By introducing characteristic length scales, the Navier-Stokes-Equation can be used to calculate dimensionless numbers to estimate the forces that apply in the current system. For this case three characteristic length are introduced, the distance between the spheres a_K , the bubble diameter d_b and the bubble rising velocity u_b . With the three forces that results from pressure gradients F_D [N/m³], the force that is introduced by the inertia of the bubble F_T and the one from friction effects F_R can be estimated.

$$\rho \cdot \rho_C \frac{u_C^2}{l_C} \left(u \frac{\partial u}{\partial x} + v \frac{\partial u}{\partial y} + w \frac{\partial u}{\partial z} \right) = -\frac{\rho_C}{l_C} \frac{\partial p}{\partial x} + \eta \frac{u_C}{l_C^2} \left(\frac{\partial^2 u}{\partial x^2} + \frac{\partial^2 u}{\partial y^2} + \frac{\partial^2 u}{\partial z^2} \right) \quad (6.3)$$

In this case for the individual terms the following data can be used for the critical values: l_C is the distance between the spheres, u_C the rising velocity of the bubble, ρ is again the density, v the velocity of the liquid, a_K the mean distance between the grid elements, μ the viscosity and finally u the effective rising velocity of the bubble ($u_{\text{bulk}} - u_{\text{rising}}$). Δv is the velocity difference between the free stream between the elements and the wake right under a sphere element. As written in Eq. 6.3, normally the pressure gradient is used to calculate F_D , but since the pressure can't be measured in this system, the pressure was approximated with the Bernoulli equation Eq. 6.1 and the velocity. The subscript L denotes that the property of the liquid is used, while B the properties from the bubble. This leads to the following approximations for the forces present in this system:

$$F_D = 1/2 \cdot \rho_L \cdot \Delta v^2 / a_K \quad (6.4)$$

$$F_T = \rho_B \cdot u_b^2 / d_b \quad (6.5)$$

$$F_R = \mu_L \cdot u_b / a_K^2 \quad (6.6)$$

For five grids, three spheres and two elliptical grids, those forces were approximated. The specifications are listed in Tab. 6.1 with the corresponding results. The inertia force is dependent on the bubble diameter, hence Tab. 6.1 5 mm is calculated with a. In Fig. 6.2 a comparison of different bubble diameters is shown.

As can be seen in Tab. 6.1 the forces introduced by the pressure are a factor 10 higher in comparison to the inertia forces. To note is, that the friction force cannot be compared directly, since its calculated with both parameters from the liquid and the bubbles. Therefore, only the pressure force and the inertia force are compared. Since the inertia force is dependent on the bubble diameter, a critical diameter can be calculated when the bubble

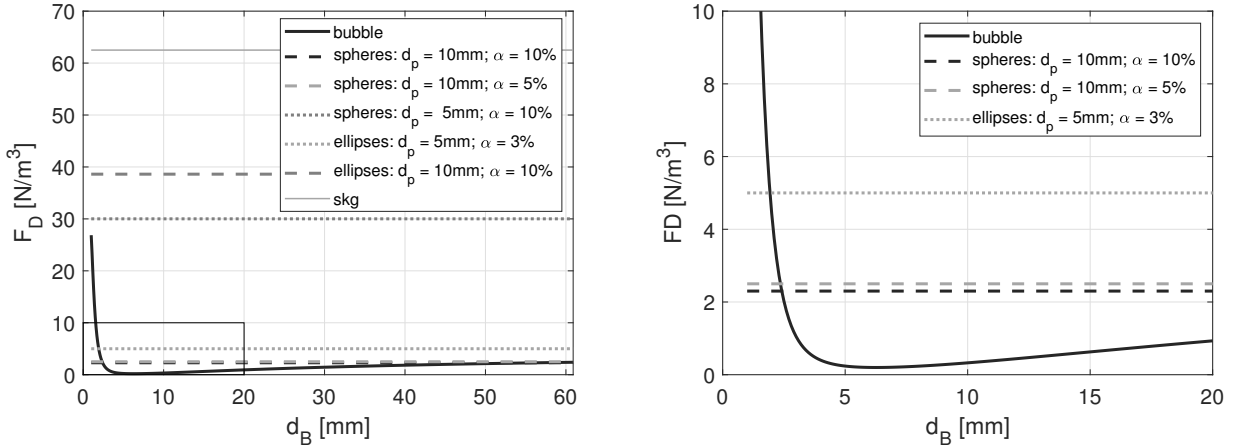


Figure 6.3: Comparison of the estimated forces introduced by the pressure gradient through the grids. In the left image on the x-axis is plotted until the bubble diameter is big enough, that the inertia forces outweigh the pressure forces. On the right a zoom in on the range is shown for the bubble diameters that are used in this work of 10 mm beyond.

is no longer affected by the pressure introduced from the grids. As in Fig. 6.3 plotted this critical diameter of bubbles would be around 50 mm bubble diameter. However, these bubbles will not be evaluated in this work, since they are five times bigger than bubbles usually used in industrial applications and are redacted from this work. For comparison a graph for the here relevant bubble diameters is shown. Furthermore, bubbles with sizes bigger than 7-8 mm start to deform and the pressure gradient does not result in a path shift anymore, but in a deformation of the bubble. For the other grids even, higher diameters would be needed which is not feasible anymore. Concluding, that the motion effects are mainly due to pressure and velocity gradients introduced, by the grid elements and are moved in between the grid elements.

6.3.2 Shape oscillations induced by emulated turbulence

In the literature various different publications explain the oscillation of free rising bubbles and describe their behavior (Lunde & Perkins 1998, De Vries 2001, Fan & Tsuchiya 1990). But to the authors knowledge the behavior in turbulent background was not reported before.

Thanks to the 3D reconstruction, it is possible to investigate the surface-to-volume ratio in order to resolve the complexity of the 3D deformation. Fig. 6.2 shows the surface-to-volume ratio calculated from the 3D measurement. Two dominant frequencies can be clearly seen in the measured data, called f_R and f_S . f_R describes the frequency of the superimposed oscillation (mean value of the individual frequencies), and f_S the frequency of the envelope. With a spectral analysis the two frequencies or rather a range for those frequencies can be determined. By considering the specific frequencies of the bubble deformation modes that describe the lateral $f_{2,0}$ and axial deformation $f_{2,2}$ oscillations, we can write $f_R = (f_{2,0} + f_{2,2})/2$ and $f_S = |f_{2,0} - f_{2,2}|/2$. A summary of all frequencies for the measured bubble diameters is given in Tab. 6.2. And a comparison of the spectral analysis in Fig. 6.4.

Similar to the evaluation for the free rising bubble both a 2D and 3D evaluation was performed. As can be seen in Tab. 6.2 all four frequencies are in a similar range if the data is evaluated in a 2D manner. The data shows that all bubbles no matter the size are oscillating in the same frequency range. This would suggest that the native bubble oscillation is overwritten by the turbulence. If the bubbles are however evaluated with the 3D approach a different picture can be seen. The superimposed turbulence seems to hinder the eigenfrequency

d_b (mm)	$f_{2,0}$ (Hz)	$f_{2,2}$ (Hz)	f_R (Hz)	f_S (Hz)
literature/theoretical	4.0	41	28	34.5
	5.0	29	20	24.5
experimental 2D				
2.2	15-25	16-26	15.5-25.5	~0.5
3.5	17-27	19.75-29.75	18.37-28.37	~1.37
4.1	14-24	14-24	14-24	-
5.0	17-27	15-25	16-26	~0.5
5.3	17.5-27.5	17-27	17.25-27.25	~0.25
6.5	17-28	19.5-29.5	18.75-28.75	~0.875
experimental 3D				
2.2	44-58	28-34	36-46	8-12
3.5	46.5-64	34.5-36	40-50	6.5-14
3.5	46.5-75	33.5-45	40-60	6.5-15
4.1	33-38	23-29	28-38	5-9
5.0	23-37	17-23	20-30	3-7
5.3	13-23	10-16	13-23	3-7
6.5	-	-	-	-

Table 6.2: Comparison of the different frequencies from the reconstruction (exp.), and theoretical calculation taken from literature. For the first literature/theoretical values f_R and f_S are calculated from $f_{2,0}$, $f_{2,2}$. From the experimental data f_R and f_S are measured and from those values $f_{2,0}$ and $f_{2,2}$ are derived.

of the bubble oscillation and forces a slower shape oscillation on the bubble. But the know decrease in the oscillation frequency, from the literature is visible again. Similar to the free rising bubbles this suggests that the oscillations need to be measured and described in a 3D manner.

Even for smaller bubbles the influence is significant. The oscillation frequencies are reduced by a factor of three, even greater for bubbles with a higher diameter. A comparison of the different frequencies are listed in Tab. 6.2 and in Fig. 6.4 the FFTs for each bubble size is shown. The grey rectangles mark indicate the range in which the range of the two dominant frequencies occur. For smaller bubbles the turbulence length scales are in the range of the bubble size and the turbulent fluctuations lead more to a change in the path then a deformation. This is further suggested by the fact, that, like it was shown in the previous section, smaller bubbles are more prone to be displaced by the fluctuations then bigger bubbles, that get more deformed and hence a bigger change to the oscillation. Here the fluctuations are not big enough to cause a displacement of the bubble but rather deform the surface which in return causes the bubble to change their oscillation frequencies. For the biggest bubble these frequencies also seem to merge at 3-7 Hz, suggesting that for even bigger bubbles this behavior becomes quite chaotic and cannot be truthfully reconstructed since it shows concave parts or the bubble oscillation is fully random or that no oscillation takes place anymore. As can be seen for the 6 mm bubble This is also shown in the 2D evaluation for the free rising bubble that the two frequencies merge for higher bubbles and the oscillation is not describable any longer.

6.3.3 Influence of the bubble on the velocity and fluctuations inside the liquid flow

Experimental Set-up

To analyze the velocity and the induced turbulent fluctuations the same four camera setup as in Cha. 4 was used. With a tomographic MLOS reconstruction and particle tracking of the tracer particles the velocity along the

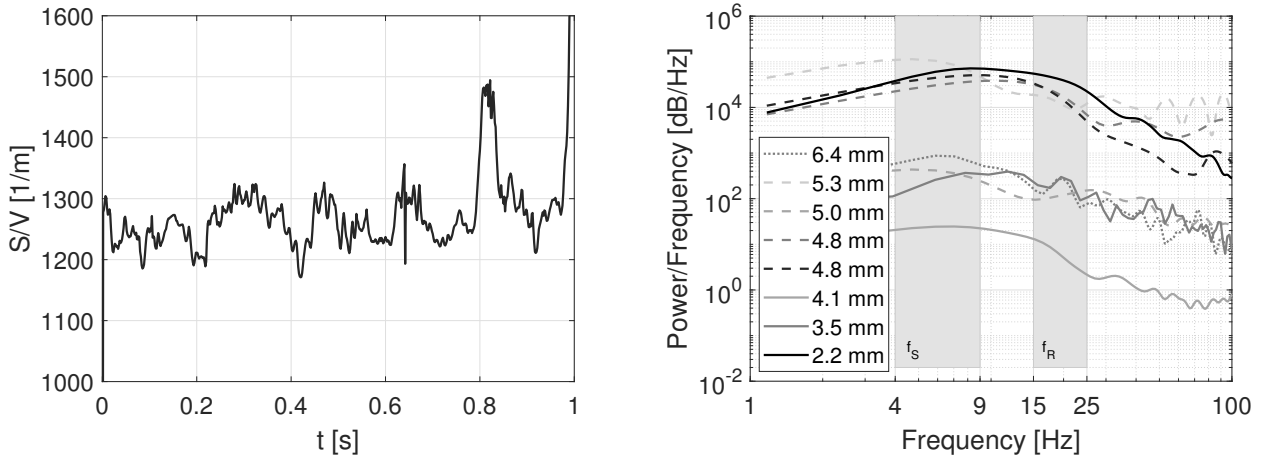


Figure 6.4: Example of the surface-to-volume ratio with time. The two frequencies are calculated from this with the Welch-method. The evaluation for different bubble diameters is shown in the right image. The most common frequency range is marked with grey boxes.

tracks can be calculated. Errors are mainly introduced by the bubble itself since due to the shadowing of the bubbles body not all cameras are able to see all particles at all times. The best results are achieved when the bubble just left the measurement area. At this point the bubbles influence is still measurable and the error that is introduced is minimal. So, in the following only those images and tracks are evaluated and discussed. However, the other tracks are used as well to get an overall impression of the swarm's statistics but are not taken into account of the calculation of the p.d.f.s etc.

Velocity in the emulated turbulence

As can be seen in Fig. 6.5 the velocity behind the bubble drops to a value of 120 mm/s in the core. This is similar to the velocity range that is induced by a free rising bubble as shown in Cha. 5. The particles are trapped in the bubbles wake pairs and get slowed down or accelerated against the counter flow. Due to the surrounding turbulence however, the wake gets dissolved only 3-4 bubble diameters stream downward. In comparison to the free rising bubble the wake is much shorter and only the stronger inner core of the wake is present or measurable.

Similar to the evaluation in Cha. 3 the probability density function of the velocity was calculated (Fig. 6.6). Data from both measurements with and without the bubble's presence are evaluated and plotted. The black line indicates the measurement with the bubble, the light gray one without. Both data plots are normalized, according to the proposed normalization of Risso (2011) with 10% of the volume ratio of the swarm. In this case the grid with a density of 10% and 5 millimeter spheres was mounted. As expected, the p.d.f. perpendicular to the flow direction (top two images in Fig. 6.6) is symmetric and self-similar both in range and intensity. The zigzagging in the plots are due to the binning of the data and has no physical meaning. Therefore, only the overall shape is important. This is similar to the expected results for bubble agitations, as described in Cha. 1 and Cha. 3. In flow direction (bottom image in Fig. 6.6) the velocity is tipped to the right side or positive velocities. This shows a similar behavior to the bubble swarm as a whole. Again as shown in Cha. 3. The bump in the p.d.f. is visible for both data with and without the bubbles presence. This suggests that the single bubble does not contribute to the overall distribution of the p.d.f.. The individual bubbles however are contributing to the overall swarm velocity distribution. The bump will be further discussed in the following section with the evaluation of the fluctuations.

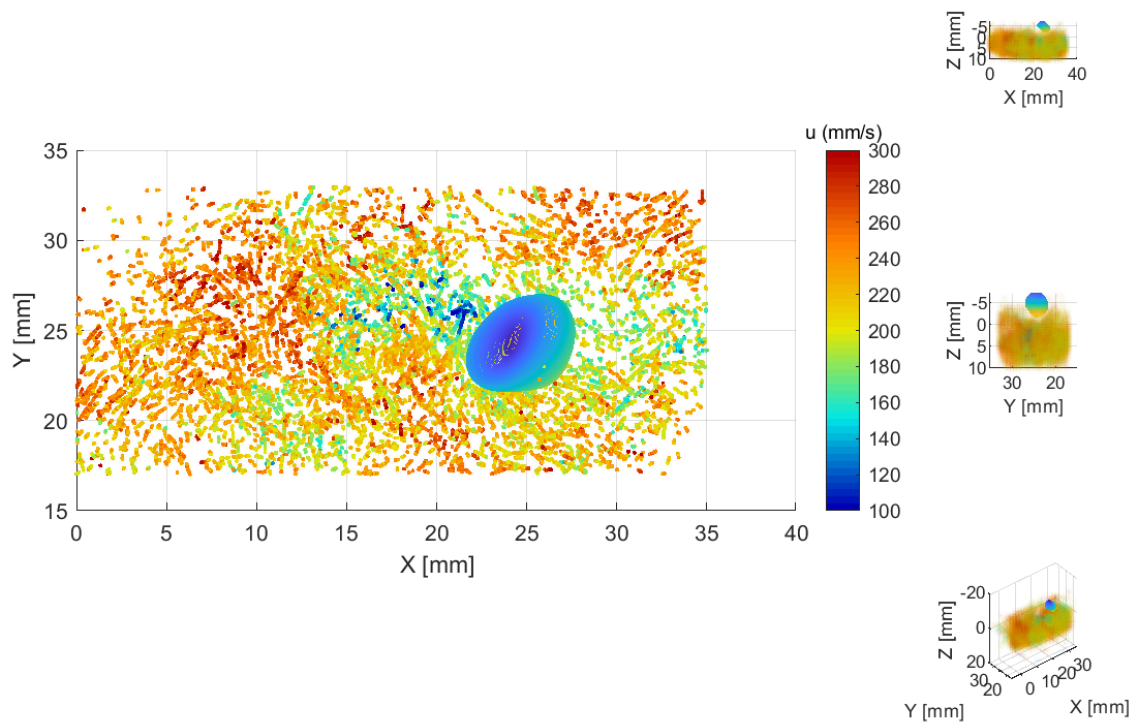


Figure 6.5: One Timestep of a suspended bubble in the emulated turbulence. The color of the dots represents the velocity. For better illustration 5 additional timesteps are plotted as well. The bubbles (blue rings, but the color of the bubble is not representative and just chosen for visibility.) influence is clearly visible. The velocity behind the bubble drops to around 120 mm/s in comparison to the 300 mm/s from the counterflow.

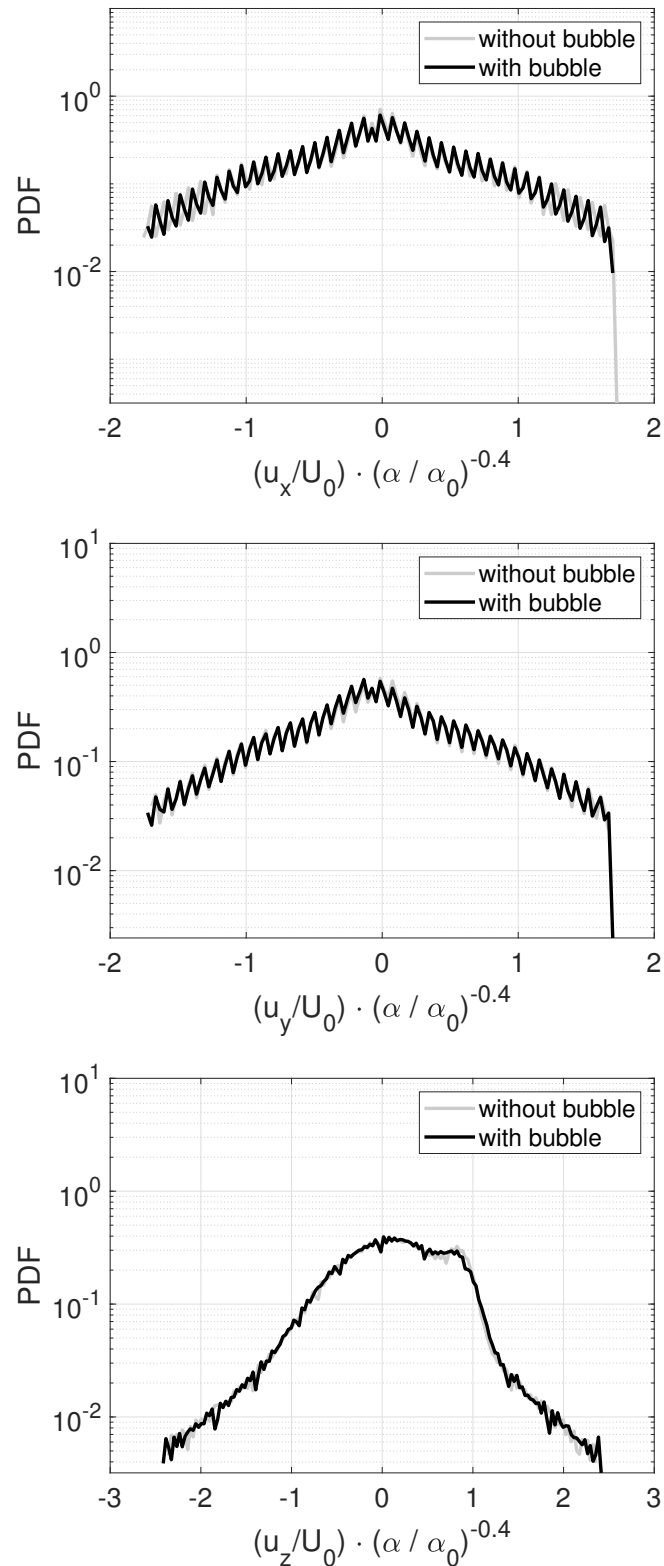


Figure 6.6: Compression of the probability density function of the velocity with and without the bubble. Taken with the 3D data. The top and middle one are the p.d.f in \vec{x} and \vec{y} direction respectively. The bottom image shows the p.d.f. in \vec{z} -direction. Z is in this case also the flow direction of the counterflow. While the p.d.f.s perpendicular to the flow direction are symmetric, the p.d.f. in the counterflow direction shows a bump to positive values. In comparison to the 2D data that was shown in [Cha. 3](#) the bump is not visible, but rather smooth.

Fluctuation probability density function

Analog to the velocities the probability density function for the fluctuations show the expected behavior. The fluctuations p.d.f. is plotted in [Fig. 6.7](#) as above the first two images show the fluctuations perpendicular to the flow, while the bottom one shows the p.d.f. in the flow direction. Same as the velocities the \vec{x} and \vec{y} are again symmetrical. Here as well the zigzagging is due to the binning of the data. In flow direction the fluctuations also show a lean towards positive fluctuations and show the bump at 0.3. With an increase of 0.25 ± 0.05 . The grid used for this experiment was a 10% grid with 5 mm speres and a 5 mm bubble. With a mean thickness of roughly half the bubble diameter this would suggest to be result of the bubble or the bubbles wake. Since the wake is dissolved roughly 3-4 bubble diameter behind the bubble, and that the bump is visible in measurements with and without the bubbles present. The bump tells that fluctuations with 0.3 are more common than other fluctuations. This bump was not visible in the 2D measurement as they were performed in [Cha. 3](#). Other grids and bubble measurements were compared to this as well and in other bubble sizes this bump was visible as well. This suggest that this bump is mainly a result of the flow and turbulence generated by the particle grids. To further investigate this behavior a experiment with a rising swarm in a clean water could give more insight into this topic if the bump is an actual effect of a bubble swarm or an artifact of the grids that is only visible when evaluated in a 3D manner.

6.3.4 Influence of the turbulence on the bubbles wake structures

In comparison to the description of free rising bubbles, the wake structures in turbulent flows are not well understood. The interaction of the surrounding turbulence with the wake is highly dependent on the local flow field. In addition, the bubble itself gets moved and deformed in the flow, making an explicit description complicated. Some aspects can however be described with the data form the tomographic 3D reconstruction. First the wake is noticeably shorter and gets diffused only a few bubble diameters behind the bubble. While in a free rising case, it is recorded that the bubble wake takes up to 20 bubble diameters, it can be seen in the 3D flow that the wake is noticeably shorten. For comparison a spatial temporal reconstruction of both a free rising and a wake behind a bubble in the emulated turbulent flow is shown. For the spatial temporal reconstruction, the displacement was chosen to create a bubble fixed origin point. In the free rising case, the flow particles were displaced with the rising velocity of the bubble. In the turbulent case the velocity difference between the bubble and the mean flow velocity was chosen as the displacement factor. This allows the comparison between the two cases for a bubble fixed coordinate system. To identify the particles that belong to the wakes a velocity threshold is applied. For the free rising bubble the threshold of 30 mm/s and for the turbulent case the threshold was chosen to 130 mm/s.

In the free rising case it can be seen as well in the side few in [Fig. 6.8](#) and in the top few in [Fig. 6.9](#) that the overall shape of the wake changes drastically. Before a comparision is made both wakes shall be described. The shape of the wake in the free rising case is roughly 20-23 bubble diameters long and one vortex piece is in the size of the bubble. As can be seen in [Fig. 6.8](#) the wake of the free rising bubble starts to decay roughly 23 bubble diameters downstream, however the full wake was not recorded, suggesting it be even longer. To reconstruct this pattern a position of the bubble for the whole measurement would need to be known, however the bubble was in the measurement volume only for a short time. If the bubble path would be known for the whole time it could be fully reconstructed. For this evaluation the main focus was placed on the decay behavior. The width of the wake on the order hand is in the order of the bubble size. They are roughly one bubble diameter displaced to the bubble. In this case as can be seen in [Fig. 6.9](#) to the north side of the bubble. Both vortex pairs have roughly the same diameter or size. The vortex on the left side has a stronger core and is slightly displaced to the outside. With a bubble size of 4 mm the transition from a zigzagging motion to a spiraling motion is to be expected and the data of the vortices also suggest that. Even though the bubbles are rising with a mean velocity

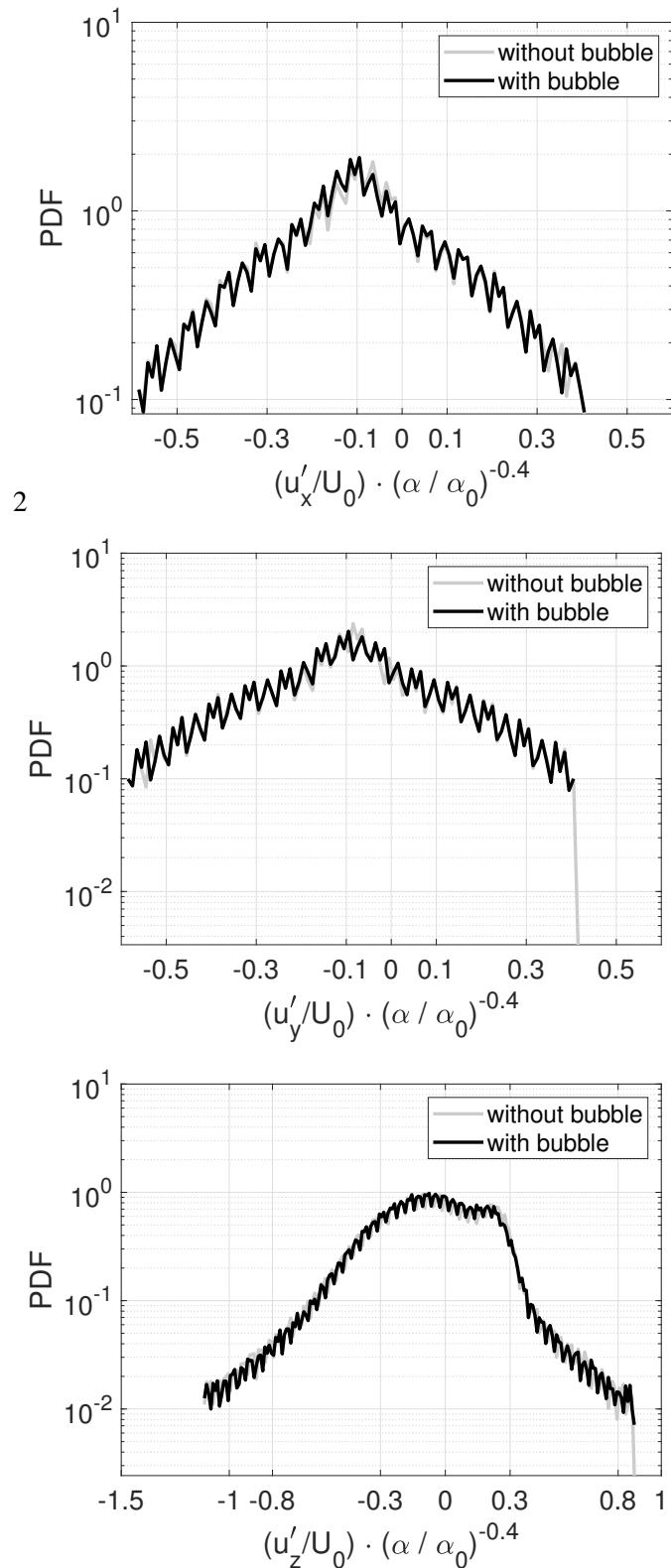


Figure 6.7: Comparison of the probability density function of the fluctuations with and without the bubble. Taken from the 3D data. The top and middle one is the represent the p.d.f in \vec{x} and \vec{y} direction respectively. The bottom image shows the p.d.f. in \vec{z} -direction. \vec{z} is in this case also the flow direction of the counterflow. While the p.d.f.s perpendicular to the flow direction are symmetric, the p.d.f. in the counterflow direction shows a bump to positive values.

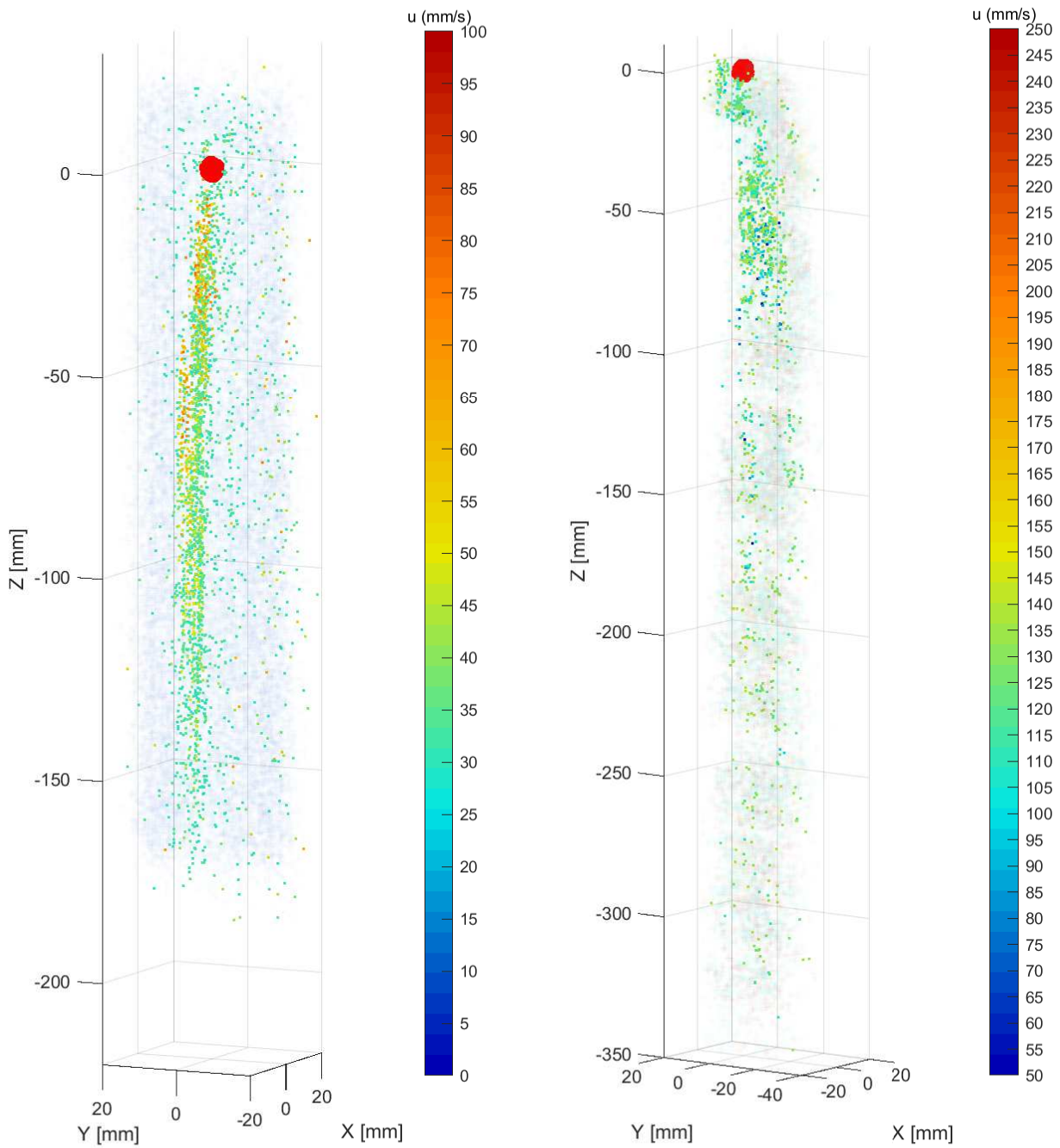


Figure 6.8: Spatial temporal reconstruction of a free rising bubble on the left and one in a counter flow setting with a 10 mm grid with a volume fraction of 5%. In both cases was the bubble moved to the coordinate origin and the flow field displaced accordingly. In the left-hand image, the displacement in \vec{z} -direction is corresponding to the rising velocity of the bubble. In the right image the sift was calculated with the effective velocity the bubble experiences. Thus, the flow field was displaced with the sum of the bubble velocity and the mean counter flow velocity.

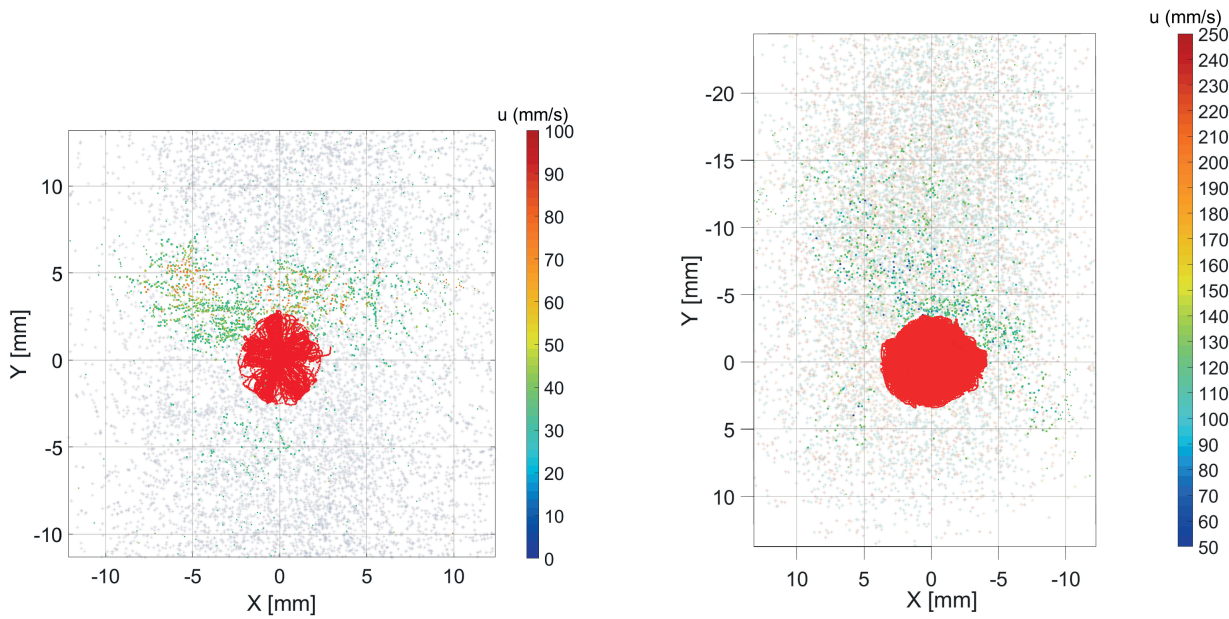


Figure 6.9: Spatial temporal reconstruction of a free rising bubble on the left and one in a counter flow setting with a 10 mm grid with a volume fraction of 5 %. In both cases was the bubble moved out of the drawing plane. In the left image, the free rising case the two counter rotating vortices can be seen forming above the bubble, marked with green to red dots. The color corresponds to the velocity. This shows that in the vortices a velocity ranges from 30 mm/s up to 100 mm/s. In the counterflow case the velocity ranges between 50 and 140 mm/s. The red dot symbolizes the bubble.

of about 250 mm/s the flow behind the bubble is in the mean of 85-100 mm/s in the core and up to 30 mm/s. While directly under the bubble the flow could not be measured due to the shadowing of the bubble but close to the bubble the flow accelerates to the same velocity as the bubble. But the velocity reduces quickly in radial direction.

In the turbulent case, the bubble and flow position are adjusted to the effective flow that the bubble experiences. The wake in the turbulent case is noticeably shortened in comparison to a bubble the same size rising freely in stagnant water. The wakes in the emulated turbulence dissipates after roughly 8 bubble diameters. Then the wake gets diffused and some parts are transported downstream. This was also predicted by [Risso \(2011\)](#) in his analysis about the shape of the p.d.f.s. Even though [Risso](#) predicted roughly 3-4 diameter, this might be due to the absence of other real bubbles in the flow. The bubbles are heavily influenced by the turbulent flow and the wake cannot develop nor can the bubble follow its path, thus making it impossible for defined structures to develop and the main structures are accumulated up to 7-8 bubble diameters behind the bubble (compare [Fig. 6.8](#)). In the data also smaller structures can be seen that do still persist downstream but got picked up by the flow and transported away from the bubble. The width of the wake is also wider than the free rising case. In this instance the wake structure is roughly double the size of the bubble ([Fig. 6.9](#)). However, it can be seen that the flow's velocity, behind the bubbles is reduced by roughly 50 % in comparison the surrounding flow. The mean flow of the liquid is set to 225 mm/s the measured flow velocity behind the bubbles wakes measured to 130 mm/s. With this it can be seen that the turbulence for the most part is dominating the behavior of the bubble and the wake. Again supporting that in a bubble swarm the wake is only a secondary factor and the overall creation of the pseudo turbulence that are created in a bubble swarm [Risso \(2011\)](#).

To create comparable measurements to the free rising bubble it was also planned to take measurements with

the chemical tracer to fully resolve the length and dissipation of the wake. Comparable to the measurements in [Cha. 5](#). However, this was not possible to the nature of the chemical tracer system to utilize it in the channel. For the whole channel to fill more than 200 liters of the iron solution would be needed, which cannot be produced at the facility. Furthermore, the whole channel would need to be fully sealed against oxygen or air in general, which is not possible with the current setup. Experiments with a diluted system was made, but the contrast of tracer to the background was not strong enough to accurately measure the wake structures. This data would have given great insight into the dissipation mechanisms of the turbulence. But knowing from the measurements with free rising bubbles, the tracer gets trapped in the core of the vortex pairs. This suggests that this would be also the case for the turbulent case and the tracer would most likely be trapped in the close bubble vicinity before it gradually gets dispersed by the counterflow.

6.4 Summary and Conclusions

In order to study the flow behavior of individual bubbles in a bubble swarm, this work presented not only a method to simultaneously record the flow field around a bubble, but also correlate it with the shape of the bubble. The shape is reconstructed solely from the shadow images, which guarantees that the surface is not contaminated with, for example tracers or other markers. With the tomographic camera setup, it was possible to record a three-dimensional flow around the bubble shape as well as influence on the shape by the turbulence. In conclusion it can be said that the behavior of the bubble is fully dictated by the turbulence and the fluctuations in the liquid. The original bubbles behavior like its path or shape oscillations are dictated by the surrounding flow.

The first aspect that was looked at was the path. It was shown that the bubble path is mainly driven by the pressure gradients induced by the velocity gradients that are created by the moving particle grids. The bubbles are moved by the Bernoulli-Effect to regions with lower turbulence levels and higher velocity. While the small bubbles tend to stay in the low-pressure regions the bigger bubbles experience a gradient over the whole volume and can't settle in the turbulent field created by this particular type of grid. In comparison to real bubble swarms the bubble is here not hindered by other bubbles and can freely rise over the whole channel width. In real bubble swarm this behavior is most likely restricted or even hindered by the swarm itself.

Secondly the shape oscillations are measured in a free rising case but also for bubbles moving in the turbulent field. Here it's clearly shown that a 2D evaluation is not suitable anymore for any kind of bubble size. The 2D evaluation shows that the turbulence is influencing the bubble oscillation but it rather suggests that the oscillation gets overwritten by the turbulence fluctuations. In contrast the 3D evaluation gives more insight with the surface-to-volume ratio that reveals that the bubbles still have some degree of dependence on the size even though the eigenfrequencies are hindered by the turbulent fluctuations up to a factor of 3. It also clearly shows that there is, similar to the free rising bubbles, that there is a critical diameter for that the bubble oscillation is becoming chaotic and the two frequencies are not sufficient anymore to describe that behavior. The bubble starts to oscillate in a random pattern that cannot be described analytically anymore. So far, the literature described the oscillation with two frequencies $f_{2,0}$ and $f_{2,2}$ those start to overlap however for bigger bubbles and don't describe the behavior sufficiently anymore. Thus two other frequencies are introduced f_R and f_S derived from the surface-to-volume ratio. With these the 3D effects can be described further and reveal that eigenfrequencies of the bubbles are still present but are superimposed by the turbulent fluctuations. In contrast a 2D evaluation shows that the eigenfrequencies are completely overwritten by the external turbulence.

The last aspect that was investigated was the wakes that are formed around the bubble. If the bubble is rising freely the wake or rather the pressure gradients induced by it determine the movement of the bubble. The wake itself persists for a long time even after the bubble has passes and up to 28 bubble diameters behind the bubble the influence of the wake can still be measured. Similar to the results from [Brücker \(1999\)](#) the two counter rotating vortices can be identified and brought in correlation with the bubbles path. In the case shown in [Fig. 6.8](#) a transition case from zigzagging to spiraling can be seen. In a turbulent flow however, the wake gets diffused

shortly behind the bubble, roughly 8 bubble diameter and most of the wake is concentrated closer to the bubble in a range of 4 bubble diameter. The shape is rather random and mostly dependent on the position of the grid elements. Thus, making it impossible for the wake to form. Furthermore, the movement and the wakes are fully determined by the emulated fluctuations.

To conclude in this chapter the behavior of the bubble in a free rising setting and with a counterflow has been measured with the new 3D technique shown in [Cha. 4](#). The turbulence has a great influence on all the aspects of the bubble, especially on the movement and the shape oscillations. And while the wake is greatly shortened, for the overall influence on phenomena like the mass transport more value should be placed on better understanding the shape changes. As can be seen in this chapter the turbulence decreases the eigenschwingen by a factor of 3 and hinders them. While even if the wake is changed the path, like in a free rising case is dominated by the pressure gradient anyway and thus the wake gives information about the location where the transported species would be collected. As can be seen in these measurements most of the species would be accumulated in the vicinity of the bubble, roughly 4-8 bubble diameter behind it.

7 Conclusions and outlook

To improve on industrial multiphase applications, it is important to understand, the complex interaction between bubbles in a swarm. In order to do that many questions still need to be answered that are crucial to evaluate industrial application. Especially experimental models and measurement techniques are important to better understand how the mechanism in a bubble swarm intertwine and interact with each other. Thus, this work focuses on experimental methods that allow studying swarms and the behavior of individual bubbles in it. In order to do that in the beginning three questions were asked:

- What is a good experimental model to emulate swarm like turbulence? How can a swarm be emulated and induced in a flow? How does it need to be characterized, to compare to real bubble agitations?
- How can a single bubble be measured without intrusive techniques? How can a single bubble be accurately described and the surface be reconstructed? Can the flow around the bubble be measured simultaneously and how are they affecting each other?
- How do bubbles behave in this emulated swarm turbulence compared to free rising bubbles? What is the difference compared to a free rising bubble?

To answer these questions a new counter flow channel was designed to emulate bubble swarms and create a flow with statistics similar to swarms that are used in industrial applications. The channel was designed in a way to induce a counterflow in which the bubble could be hold in place for the desired measurement time. The transparent test section allowed for an optical access from all four sides, which makes it possible to utilize a variety of measurement techniques. Among these are particle image velocimetry (PIV), particle tracking velocimetry (PTV) and shadowgraphy among others. At first this channel needed to be characterized and tested how a clean, undisturbed flow in this channel behaves. For this multiple PIV and 2D stereo PIV measurements were executed to characterize the flow over the whole channel width, both in the middle and the wall. From those measurements the channel itself showed a good homogeneity. This was mainly achieved with a specially designed inlet that distributes the flow evenly over the whole channel. Even though the initial turbulence level is quite high this is wanted by design to have a similar range then the expected turbulence of a bubble swarm.

The turbulence to emulate the swarm statistics is induced by letting the water flow through specially designed grids. Two different grids types were crafted and characterized in regards of the flow statistics. With planar and 3D PIV/PTV the flow was evaluated in comparison to the real bubbly flows. The first types of grids were fractal grids. These grids are 3D-printed structures that repeat certain shapes with decreasing size. The ones used here repeated the I-shape. The second type are so called free moving particle grids. Small plastic spheres or ellipsoids are connected with a loose string. This allows the sphere strings to almost move freely in the counter flow. From 2D flow field measurements, done with planar PIV different size and volume fraction combinations were characterized in regards to turbulence level, homogeneity, probability density functions and energy spectra. Last was done by at the University in Bremen. From these the best agreement with real statistics was found to be from grids with 10 mm spheres and a volume fraction of 10 % and a grid with elliptical elements and a volume fraction of ~4 %. The fractal grids however showed a strong inhomogeneity across the channel cross section, making this grid not suitable for further experiments, with a redesign of the grids a better flow could be achieved, but these would expensive to manufacture and prone to break easily in the channel. Thus, in the following experiments the free moving particle grids were used predominantly, two grids and one that showed

strong velocity gradients were used to emulate bubble swarm turbulence. With these grids it was a goal to evaluate the behavior of single bubbles in swarm like turbulence. This allows to measure bubbles as if they were moving in a real bubble swarm. Within this thesis a comparison of the behavior and different aspects of the bubble motion with and without an external fluctuation was shown and discussed. To further improve on the method to create bubble fluctuations a different approach with an active grid could be made. The grid consists of individual motors that power small elements. By setting the rotation frequency of the individual motors a variety of fluctuations can be inserted in the flow. With this an even more accurate model flow could be created. This grid however was not integrated into the channel to time restrictions and spatial impairments in the room the channel was build. With the channel and model swarm in place the bubbles could be tested inside this bubble swarm and the interactions been measured. For this further question arose:

- How can a single bubble be measured without intrusive techniques?
- How can a single bubble be accurately described and the surface be reconstructed?
- Can the flow around the bubble be measured simultaneously and how are they affecting each other?

One aspect, that is especially important for the mass transport is the bubble's surface and the three-dimensional shape changes. To measure the shape and its oscillations a new technique was developed that allows to reconstruct the bubble surface from shadow images. The bubbles were illuminated with a strong backlight to create a high contrast image and then binarized with image processing algorithms to separate the bubble from the background. This has the advantages that no tracer or other marker needs to be placed on the bubble and influencing the physical aspects like the surface tension. It does however not allow for a reconstruction of convex surfaces. Therefore this method can only reconstruct bubbles reliably up to a size of 6 mm. The shadow images are correlated with a MLOS algorithm similar to those used in tomographic PIV. The bubble is treated as one big particle and the line of sight from each individual camera is multiplied. This allows for a reconstruction of the surface. Depending on the number of cameras used, some parts of the bubbles, like the poles do still show artifacts. This could be improved by a different camera position or added cameras. This was not possible to implement in the channel since a better reconstruction would have one camera required to look from the top to bottom or vice versa on the bubble which could obviously not be done due to the water in the channel. More cameras could also improve on the reconstruction but were not available at the university. However, with this method no special chemical or physical tracers are needed and can be used in every setup that allows for an optical access. With this method it is now possible to study not only free rising bubbles but also bubbles moving in the emulated turbulence, which proposes again new questions:

- How do bubbles behave in this emulated swarm turbulence compared to free rising bubbles?
- What are the difference compared to a free rising bubble?

With this technique free rising bubbles and bubbles moving in emulated turbulence are compared to each other. For both cases the shape was reconstructed and the flow around the bubble was recorded with the introduced 3D methods. From this data different behaviors are investigated, like the bubble path, the bubble shape and its deformation with time and the wake structures. To create a basis for comparison and validation of the measurement technique free rising bubbles of different sizes were recorded. Those showed the well-known different path oscillation and deformations. In current publications the deformation was mainly evaluated from 2D data, which is correct for small bubbles. For bigger bubbles however it is important to evaluate the 3D shapes, since different modes start to deform the bubbles in a complex manor. This work used the surface-to-volume ratio to study the deformation behavior and showed that the two frequencies, in literature named as the $f_{2,0}$ and $f_{2,2}$ start to overlap. These can then be described as a beat of the two frequencies and they can be measured from the surface to volume ratio. The two new frequencies are named in this work as f_R and f_S . Therefore this

work suggests that for small bubbles up to a range of 4 mm the 2D evaluation with $f_{2,0}$ and $f_{2,2}$ is sufficient, but for bigger bubbles the 3D effects need to be taken into account and instead the deformation is described with f_R and f_S .

If the bubbles are now moving in the emulated turbulence, the first thing that is notable is, that the bubbles move in between the grid elements. The bubbles get moved by the pressure gradients induced by the grid elements. The main forces that drive this process can be estimated with the Bernoulli and Navier-Stokes-Equation. This shows that the main driving force is the pressure difference. By adding seeding particles into the flow, the wake structures behind the bubble can be visualized and reconstructed. In comparison to freely rising bubbles the wakes are shortly after diffused by induced turbulence. While the wakes of free rising bubbles persist up to 10 bubble diameter the wake structures are diffused in roughly 2-3 bubble diameters. While the wake structures behind free rising bubbles are dependent on the path motion, like zigzagging or spiraling, the wake structures in the flow structures are similar in strength but accumulate behind the bubble which stretches the width and the wakes are quickly diffused.

Additionally, in cooperation with the Department Chemie at the Ludwig-Maximilians-Universität München (Prof. Klüfers, LMU Munich Germany) the chemical tracer was introduced to visualize the wake structures. To visualize the mass transport from the bubbles interface in the liquid, a specially designed reactive system was used. The oxygen in the bubbles is bound to the iron in the liquid, which causes a visual darkening that can be detected with the cameras. For a better contrast and detection LED back lights and a diffuser were installed on the opposite side of the cameras. Please refer to (Aas & Klüfers 2017) for more information about the chemistry of this system. With this system and the 3D PTV reconstruction a full view of the small and big structures was made. While the PTV data gives insight in the dimensions the chemical tracer shows small structures in the flow like the crow instability. In the future a combination of both techniques could yield an even better comparison of the flow and the mass transport. If the 3D shadowgraphy reconstruction is added on top it is possible to also use the shadow images of the chemical tracer to reconstruct the in space. An example of such a measurement is shown in Fig. 7.1. The possibility to utilize the chemical tracer in conjunction with the emulated flow would also enhance the understanding how the wake gets diffused.

In conclusion this work presented many possibilities to study the flow behavior of free rising and bubbles moving in emulated flow and gave more insight in how some of the aspects intertwine and work together. From the evaluation several more questions came up that could be answered with additional measurements and experimental work.

- Can an even better turbulence model be achieved with for example the active grid?
- Is there a way to improve further on the reconstruction? For example with more cameras or a completely different method?
- How does a small set of bubbles behave in a emulated background turbulence? Are they stabilizing each other in their path? How are the wakes influenced?
- What is the influence of a surfactant on the oscillation frequencies? Could they be oppressed completely? Or even altered so the turbulence is not influencing the oscillation any longer?

But with this work a foundation for future experiments have been made and introduced a powerful measurement technique and evaluation tools to characterize the bubbles motion and shape oscillations with and without emulated turbulence.

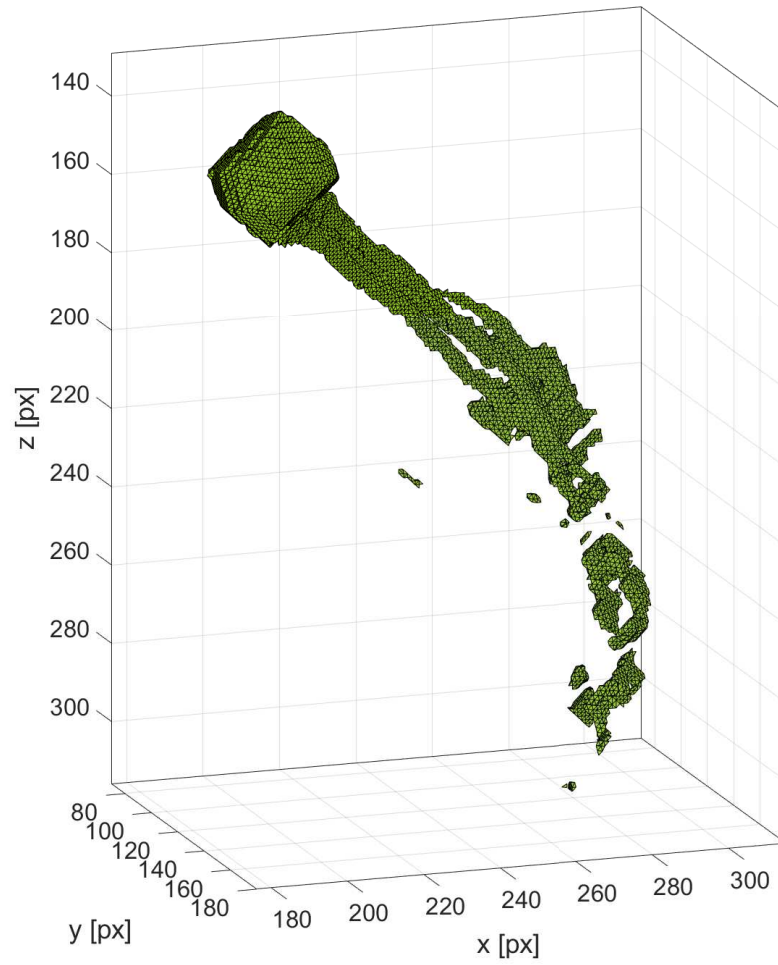


Figure 7.1: One time step of a freely rising NO-bubble in the FeEDTA solution. The reconstruction was done analog to the one in [Cha. 3](#). The two wakes behind the bubble are clearly visible and the wake diffuses roughly 3 bubble diameters behind the bubble.

LIST OF REFERENCES

- AAS BM & KLÜFERS P (2017). *The Structural Chemistry of Stable High-Spin Nitrosyl–Iron(II) Compounds with Aminocarboxylato Co-Ligands in Aqueous Solution*. European Journal of Inorganic Chemistry 2017:2313–2320, DOI: 10.1002/ejic.201601330
- ABBAS M, CLIMENT E, SIMONIN O & MAXEY MR (2006). *Dynamics of bidisperse suspensions under Stokes flows : Linear shear flow and sedimentation* Dynamics of bidisperse suspensions under Stokes flows : Linear shear flow and sedimentation. Phys Fluids 121504, DOI: 10.1063/1.2396916
- ABDULMOUTI H (2014). *Bubbly Two-Phase Flow: Part I- Characteristics, Structures, Behaviors and Flow Patterns*. American Journal of Fluid Dynamics 4:194–240, DOI: 10.5923/j.ajfd.20140404.03
- AMOURA Z (2008). *Etude hydrodynamique de l'écoulement traversant un réseau aléatoire de sphères fixes*. PhD thesis
- AYBERS N & TAPUCU A (1969). *The motion of gas bubbles rising through stagnant liquid*. Wärme-und Stoffübertragung 2:118–128
- BOOKSTEIN AFL, STRAUSS RE, HUMPHRIES JM, CHERNOFF B & ELDER RL (1982). *Society of Systematic Biologists A Comment Upon the Uses of Fourier Methods in Systematics*. Soc Syst Biol 31:85–92
- BOZZANO G & DENTE M (2000). *Shape and terminal velocity of single bubble motion: a novel approach*. Comput Aided Chem Eng 8:649–654, DOI: 10.1016/S1570-7946(00)80110-8
- BRÜCKER C (1999). *Structure and dynamics of the wake of bubbles and its relevance for bubble interaction*. Physics of fluids 11:1781–1796, DOI: 10.1063/1.870043
- CLIFT R, GRACE J & WEBER M (1978). *Bubbles, Drops, and Particles*, 1st edn. Academic Press, New York
- CROW SC (1970). *Stability theory for a pair of trailing vortices*. AIAA journal 8:2172–2179, DOI: 10.2514/3.6083
- DE VRIES AWG (2001). *Path and wake of a rising bubble*. Eng Fluid Dyn p 106, DOI: ISBN9036515262Copyright
- DECKWER WD (1985). *Reaktionstechnik in Blasensäulen*. Salle
- ELSINGA GE, SCARANO F, WIENEKE B & VAN OUDHEUSDEN BW (2006). *Tomographic particle image velocimetry*. Experiments in Fluids 41:933–947, DOI: 10.1007/s00348-006-0212-z
- FAN LS & TSUCHIYA K (1990). *Bubble Wake Dynamics in Liquids and Liquid–Solid Suspensions*. Butterworth-Heinemann, Boston London Singapore Sydney Toronto Wellington, DOI: 10.1016/C2009-0-24002-5
- FORTUNA G & HANRATTY TJ (1971). *Frequency of the Boundary Layer on*. New York 14:1499–1507
- GRANLUND GH (1972). *Fourier Preprocessing for Hand Print Character Recognition*. IEEE Trans Comput C-21:195–201, DOI: 10.1109/TC.1972.5008926
- HAASE K, KÜCK UD, THÖMING J & KÄHLER CJ (2017). *Emulation of Bubble-Induced Turbulence Using Randomly Moving Particles in a Grid Structure*. Chemical Engineering & Technology 40:1502–1511, DOI: 10.1002/ceat.201600687
- HARTUNIAN RA & SEARS WR (1957). *On the instability of small gas bubbles moving uniformly in various liquids*. J Fluid Mech 3:27–47, DOI: 10.1017/S0022112057000464
- HASSLBERGER J, KLEIN M & CHAKRABORTY N (2018). *Flow topologies in bubble-induced turbulence: A direct numerical simulation analysis*. Journal of Fluid Mechanics 857:270–290, DOI: 10.1017/jfm.2018.750

REFERENCES

- HEITHOFF S, KÜCK UD, VOLKMER P, RÄBIGER N & FRITSCHING U (2017). *Modelling mass transfer in gas-liquid two-phase flow in a jet zone loop reactor*. Can J Chem Eng 95:180–186, DOI: 10.1002/cjce.22660
- HENDRIX MHW, MANICA R, KLASEBOER E, CHAN DYC & OHL CD (2012). *Spatiotemporal evolution of thin liquid films during impact of water bubbles on glass on a micrometer to nanometer scale*. Phys Rev Lett 108:247803, DOI: 10.1103/PhysRevLett.108.247803
- HOSOKAWA S & TOMIYAMA A (2013). *Bubble-induced pseudo turbulence in laminar pipe flows*. International journal of heat and fluid flow 40:97–105, DOI: 10.1016/j.ijheatfluidflow.2013.01.004
- HURST D (2007). *Scalings and decay of fractal-generated turbulence*. Physics of Fluids 035103:0–31, DOI: 10.1063/1.2676448
- KÄHLER CJ, SCHARNOWSKI S & CIERPKA C (2012). *On the resolution limit of digital particle image velocimetry*. Experiments in Fluids 52:1629–1639, DOI: 10.1007/s00348-012-1280-x
- KIM H, WESTERWHEEL J & ELSINGA GE (2012). *Comparison of Tomo-PIV and 3D-PTV for microfluidic flows*. Measurement Science and Technology 24:024007, DOI: 10.1088/0957-0233/24/2/024007
- KIM M, LEE JH & PARK H (2016). *Study of bubble-induced turbulence in upward laminar bubbly pipe flows measured with a two-phase particle image velocimetry*. Experiments in Fluids 57:55, DOI: 10.1007/s00348-016-2144-6
- KLASEBOER E, MANICA R, HENDRIX MH, OHL CD & CHAN DY (2014). *A force balance model for the motion, impact, and bounce of bubbles*. Physics of Fluids 26:092101
- LANCE M & BATAILLE J (1991). *Turbulence in the liquid phase of a uniform bubbly air–water flow*. Journal of fluid mechanics 222:95, DOI: 10.1017/S0022112091001015
- LAUTERBORN W & KURZ T (2010). *Physics of bubble oscillations*. Reports Prog Phys 73, DOI: 10.1088/0034-4885/73/10/106501
- LIU TJ & BANKOFF SG (1993). *Structure of air-water bubbly flow in a vertical pipe-I. liquid mean velocity and turbulence measurements*. International Journal of Heat and Mass Transfer 36:1049–1060, DOI: 10.1016/S0017-9310(05)80289-3
- LIU Z, ZHENG Y, JIA L & ZHANG Q (2005). *Study of bubble induced flow structure using PIV*. Chemical Engineering Science 60:3537–3552, DOI: 10.1016/j.ces.2004.03.049
- LOTH E (2008). *Quasi-steady shape and drag of deformable bubbles and drops*. International Journal of Multiphase Flow 34:523–546, DOI: 10.1016/j.ijmultiphaseflow.2007.08.010
- LUNDE K & PERKINS R (1995). *A Method for the Detailed Study of Bubble Motion and Deformation*. Elsevier Science B.V., DOI: 10.1016/B978-0-444-81811-9.50040-8
- LUNDE K & PERKINS RJ (1998). *Shape Oscillations of Rising Bubbles*. Journal of Applied Sciences Research 58:387–408, DOI: 10.1023/A:1000864525753
- MAGNAUDET J & EAMES I (2000). *The Motion of High-Reynolds-Number Bubbles in Inhomogeneous Flows*. Annual Review of Fluid Mechanics 32:659–708, DOI: 10.1146/annurev.fluid.32.1.659
- MANICA R, HENDRIX MHW, GUPTA R, KLASEBOER E, OHL CD & CHAN DYC (2013). *Effects of hydrodynamic film boundary conditions on bubble–wall impact*. Soft Matter 9:9755–9758, DOI: 10.1039/C3SM51769A
- MANICA R, HENDRIX MH, GUPTA R, KLASEBOER E, OHL CD & CHAN DY (2014). *Modelling bubble rise and interaction with a glass surface*. Applied Mathematical Modelling 38:4249 - 4261, DOI: <https://doi.org/10.1016/j.apm.2014.03.039>
- MARTINEZ J, CHEHATA D, VAN GILS DPM, SUN C & LOHSE D (2009). *On bubble clustering and energy spectra in pseudo-turbulence*. Journal of Fluid Mechanics pp 1–35, DOI: 10.1017/S0022112009993570

REFERENCES

- MCLEOD N (2011). *PalaeoMath 101 Semilandmarks and Radial Fourier Analysis*. Paleontol News 176:25–42
- MICHIYOSHI I & SERIZAWA A (1986). *Turbulence in two-phase bubbly flow*. Nuclear Engineering and Design 95:253–267, DOI: 10.1016/0029-5493(86)90052-X
- MIESSNER U, KÜCK UD, HAASE K, KÄHLER CJ, FRITSCHING U & THÖMING J (2017). *Experimental Assessment of an Innovative Device to Mimic Bubble Swarm Turbulence*. Chemical Engineering & Technology 40:1466–1474, DOI: 10.1002/ceat.201600688
- MIZUSHINA T (1971). *The Electrochemical Method in Transport Phenomena*. Adv Heat Transf 7:87–161, DOI: 10.1016/S0065-2717(08)70017-0
- PANNEK S, PAULI J & ONKEN U (1994). *Determination of local hydrodynamic parameters in bubble columns by the electrodiffusion method with oxygen as depolarizer*. Journal of applied electrochemistry 24:666–669, DOI: 10.1007/BF00252093
- PAULI J (1992). Einsatz von Elektrodiffrusionsmeßtechnik in Gas-Flüssigkeits-Strömungen mit Sauerstoff als Depolarisator, als ms. ge edn. VDI-Verl., Düsseldorf
- PROSPERETTI A, CRUM LA & COMMANDER KW (1988). *Nonlinear bubble dynamics*. The Journal of the Acoustical Society of America 83:502–514, DOI: 10.1121/1.396145
- REDDY AJ & SZERI AJ (2002). *Shape stability of unsteadily translating bubbles*. Phys Fluids 14:2216–2224, DOI: 10.1063/1.1483840
- RIBOUX G, RISSO F & LEGENDRE D (2009). *Experimental characterization of the agitation generated by bubbles rising at high Reynolds number*. Journal of Fluid Mechanics 643:509, DOI: 10.1017/S0022112009992084
- RIBOUX G, LEGENDRE D & RISSO F (2013). *A model of bubble-induced turbulence based on large-scale wake interactions*. J Fluid Mech 719:362–387, DOI: 10.1017/jfm.2013.12
- RISSO F (2011). *Theoretical model for k^{-3} spectra in dispersed multiphase flows*. Physics of fluids 23:011701, DOI: 10.1063/1.3530438
- RISSO F (2016). *Physical interpretation of probability density functions of bubble-induced agitation*. Journal of fluid mechanics 809:240–263, DOI: 10.1017/jfm.2016.690
- RISSO F & ELLINGSEN K (2002). *Velocity fluctuations in a homogeneous dilute dispersion of high-Reynolds-number rising bubbles*. J Fluid Mech 453:395–410, DOI: 10.1017/S0022112001006930
- RISSO F, ROIG V, AMOURA Z, RIBOUX G & BILLET AM (2008a). *Wake attenuation in large Reynolds number dispersed two-phase flows*. Philosophical Transactions of the Royal Society A: Mathematical, Physical and Engineering Sciences 366:2177–90, DOI: 10.1098/rsta.2008.0002
- RISSO F, ROIG V, AMOURA Z, RIBOUX G & BILLET AM (2008b). *Wake attenuation in large Reynolds number dispersed two-phase flows*. Philosophical Transactions of the Royal Society A: Mathematical, Physical and Engineering Sciences 366:2177–90, DOI: 10.1098/rsta.2008.0002
- SAFFMAN PG (1956). *On the rise of small air bubbles in water*. Journal of Fluid Mechanics 1:249–275, DOI: 10.1017/S0022112056000159
- SCHLÜTER M, BOTHE D, HERRES-PAWLIS S & NIEKEN UE (2021). *Reactive Bubbly Flows - Final Report of the DFG Priority Program 1740*, 1st edn. Springer International Publishing
- SERIZAWA A, KATAOKA I & MICHIYOSHI I (1975). *Turbulence structure of air-water bubbly flow-II. local properties*. Int J Multiph Flow 2:235–246, DOI: 10.1016/0301-9322(75)90012-9
- TAKAGI S & MATSUMOTO Y (2011). *Surfactant Effects on Bubble Motion and Bubbly Flows*. Annual Review of Fluid Mechanics 43:615–636, DOI: 10.1146/annurev-fluid-122109-160756

REFERENCES

- TOMIYAMA A, ZUN I, SOU A & SAKAGUCHI T (1993). *Numerical analysis of bubble motion with the VOF method*. Nuclear Engineering and Design 141:69–82, DOI: 10.1016/0029-5493(93)90093-O
- TOMIYAMA A, CELATA G, HOSOKAWA S & YOSHIDA S (2002). *Terminal velocity of single bubbles in surface tension force dominant regime*. International journal of multiphase flow 28:1497–1519, DOI: 10.1016/S0301-9322(02)00032-0
- TOMIYAMA A, NAKAHARA Y, ADACHI Y & HOSOKAWA S (2003). *Shapes and rising velocities of single bubbles rising through an inner subchannel*. Journal of Nuclear Science and Technology 40:136–142, DOI: 10.1080/18811248.2003.9715343
- TSAMOPOULOS JA & BROWN RA (1983). *Nonlinear oscillations of inviscid drops and bubbles*. J Fluid Mech 127:519–537, DOI: 10.1017/S0022112083002864
- VELDHUIS C (2007). *Leonardo's paradox: path and shape instabilities of particles and bubbles*. PhD thesis, Universiteit Twente
- VELDHUIS C, BIESHEUVEL A & VAN WIJNGAARDEN L (2008). *Shape oscillations on bubbles rising in clean and in tap water*. Physics of fluids 20, DOI: 10.1063/1.2911042
- DE VRIES A, BIESHEUVEL A & VAN WIJNGAARDEN L (2002). *Notes on the path and wake of a gas bubble rising in pure water*. International journal of multiphase flow 28:1823–1835, DOI: 10.1016/S0301-9322(02)00036-8
- WANG S, LEE S, JONES O & LAHEY R (1987). *3-D turbulence structure and phase distribution measurements in bubbly two-phase flows*. Int J Multiph Flow 13:327–343, DOI: 10.1016/0301-9322(87)90052-8